Surface Modification of Magnetite for Supercapacitors: Experiment and Theory

Advancements in Supercapacitor Technology: Experimental and Theoretical Investigations on Surface Modification of Magnetite Nanoparticles with Enhanced Performance

By

COULTON BOUCHER,

B.Eng. (Materials Engineering)

A Thesis Submitted to the School of Graduate Studies

in the Partial Fulfillment of the Requirements for the Degree of

Master of Applied Science

in

Materials Science and Engineering

McMaster University

Hamilton, Ontario

Master of Applied Science (2023)

Materials Science & Engineering

McMaster University

Hamilton, Ontario, Canada

TITLE: Advancements in Supercapacitor Technology: Experimental and Theoretical Investigations on Surface Modification of Magnetite Nanoparticles with Enhanced Performance

AUTHOR:

Coulton Boucher,

B.Eng. (Materials Engineering)

CO-SUPERVISOR:

Dr. Oleg Rubel,

McMaster University, ON, Canada

CO-SUPERVISOR:

Dr. Igor Zhitomirsky,

McMaster University, ON, Canada

NUMBER OF PAGES: xv, 110

Abstract

Supercapacitors have emerged as a promising energy storage technology with unique characteristics that set them apart from conventional batteries and capacitors. Supercapacitors bridge the gap between these two technologies by combining the high power density of capacitors with the high energy storage capacity of batteries, offering a compelling solution for various applications. In the pursuit of enhancing supercapacitor performance, magnetite (Fe_3O_4) has been researched as a potential anode material. Fe_3O_4 offers several desirable properties, including high theoretical capacitance, low cost, and environmental friendliness. Compositing Fe_3O_4 with conductive additives has served to address the issue of limited conductivity in Fe_3O_4 anodes for practical uses, however, a focus must be shifted to enhancing the capacitive performance of such anodes to unlock their full potential. Achieving the full potential of Fe_3O_4 for supercapacitor applications requires addressing challenges in the colloidal fabrication of high-active mass electrodes. This is done by exploring the exceptional adsorption properties of two dispersing and capping agents: 3,4-dihydroxybenzoic acid and murexide.

Exceptional adsorption properties of catecholate-type 3,4-dihydroxybenzoic acid molecules were explored for surface modification of Fe_3O_4 nanoparticles to enhance their colloidal dispersion as verified by sedimentation test results and Fourier-transform infrared spectroscopy measurements. Electrodes prepared in the presence of 3,4-dihydroxybenzoic acid exhibited nearly double the capacitance at slow charging rates as compared to the control samples without the dispersant or with benzoic acid as a non-catecholate dispersant. Density functional theory analysis of adsorption behaviour of 3,4-dihydroxybenzoic acid and benzoic acid at the (001) surface of Fe_3O_4 corroborated these experimental results by providing an understanding of the basic mechanism of 3,4-dihydroxybenzoic acid adsorption on the surface of nanoparticles.

Furthermore, murexide for surface modification of Fe_3O_4 nanoparticles effectively enhanced the performance of multi-walled carbon nanotube-Fe_3O_4 supercapacitor anodes. Our experimental results demonstrate significant improvements in electrode performance when murexide is used as a capping or dispersing agent compared to the case with no additives. From impedance measurements, we revealed a substantial decrease in the real part of impedance for samples prepared with murexide, indicating easier charge transfer at more negative electrode potentials, and reinforcing the role of murexide as a capping agent and charge transfer mediator. The theoretical investigation allowed us to identify the nature of chemical bonds between murexide and the surface, with significant charge transfer taking place between the Fe_3O_4 surface and murexide adsorbate.

Acknowledgements

I would like to take this opportunity to express my heartfelt gratitude to Dr. Oleg Rubel and Dr. Igor Zhitomirsky for their invaluable guidance, unwavering support, and profound contributions throughout my thesis journey. Their expertise, patience, and encouragement have been instrumental in shaping the trajectory of my degree and helping me navigate through the complexities of my research. I am truly fortunate to have had the privilege of learning and working under such remarkable supervision and am deeply grateful for their dedication to my academic and personal growth.

I would like to extend my gratitude to the wonderful colleagues from both the Zhitomirsky and Rubel groups, whose support and invaluable discussions have been integral to the success of my thesis. Special thanks go to Wenyu Liang, Wenjuang Yang, Chengwei Zhang, and Kayla Baker from the Zhitomirsky group, as well as Magdalena Laurien, Himanshu Saini, Larissa Grigat, Andres Gomez, and Caio Miliante from the Rubel group. Their collaborative spirit and willingness to share their expertise have enriched my research journey and contributed significantly to the depth of my work.

I would like to express my sincerest appreciation to my Mom, Dad, Brother, and Sister, for their unwavering and constant encouragement through all of my challenging endeavors. Their love and belief in me have been a constant source of strength, and I am deeply grateful for their presence in my life.

Finally, I am incredibly grateful to my loving girlfriend and best friend, Justine Bourak. Her unwavering love, support, and patience have been a constant source of inspiration throughout this journey.

Contents

List of Figures

List of Tables

Declaration of Academic Achievement

I, Coulton Boucher, declare that this thesis titled, **Advancements in Supercapacitor Technology: Experimental and Theoretical Investigations on Surface Modification of Magnetite Nanoparticles with Enhanced Performance**, and the works presented in it are my own. This thesis was written to fulfill requirements of the M.A.Sc. degree in the Department of Materials Science and Engineering at McMaster University. All work described was undertaken from September 2021 to July 2023.

The experiments described in the following written document were conceived and conducted by the author of this thesis, in consultation with the co-supervisors, Dr. Igor Zhitomirsky and Dr. Oleg Rubel.

Chapter 1

Introduction

1.1 Motivation

The pursuit of global energy consumption solutions has spurred extensive research and development in the realm of alternative energy storage devices. Among these, supercapacitors have garnered considerable attention owing to their exceptional attributes, including rapid charge/discharge capabilities, high power density, extended lifespan, safety, and environmental friendliness. They serve as a vital link between traditional capacitors and batteries/fuel cells, effectively bridging the gap in terms of power and energy output. While capacitors excel in delivering higher power density, batteries and fuel cells outperform in energy density output. The advancement of supercapacitor technology is primarily driven by its applications in renewable energy sources and electric vehicle technologies [1]. Notably, supercapacitors are increasingly employed as interim energy storage for regenerative braking in hybrid and electric vehicles, as well as for managing power fluctuations arising from various renewable energy sources [1]. This rapidly evolving field, often in conjunction with other energy storage devices such as batteries or

fuel cells, is witnessing substantial commercial growth and interest. It is projected that sales will experience a surge from $3.3 billion in 2019 to reach $17 billion USD by 2027 [2]. Despite their immense potential, several fundamental and practical challenges still hinder the widespread adoption of supercapacitors. These include low energy density, limited cycling stability, and high cost [3]. Thorough investigation and understanding of supercapacitor materials, designs, and fabrication techniques are crucial to overcome these challenges and unlock the full potential of supercapacitor technology.

Materials selection and design will control supercapacitor performance and cost in the future. These materials are mainly investigated as electrode materials, electrolyte materials, and current collectors. By utilizing distinct materials for the anode and cathode, a supercapacitor device can optimize its operational voltage window by capitalizing on the unique potential ranges offered by each electrode [4]. The negative electrodes display a significantly lower gravimetric capacitance than the positive electrodes, leading to a greater active mass in the negative electrode needed to match the capacitance of the positive electrode. This emphasizes the need to increase the specific capacitance of the negative electrodes, while ensuring excellent performance at high active mass. Additionally, a decline in specific capacitance is observed as the active mass of capacitive material increases, primarily due to the weak electronic and ionic conductivities [5] of metal oxide-based electrodes. Significant attention must therefore be given to the development of innovative fabrication techniques and device designs.

1.2 Structure of this thesis

The structure of this thesis is as follows: In Chapter 2, I present fundamental principles and relevant literature review relevant to my investigation. In Chapters 3 and 4, I introduce the research problems and objectives, respectively. In Chapters 5 and 6, I then present the research outcomes achieved during my graduate studies.

Bibliography

[1] M. Şahin, F. Blaabjerg, and A. Sangwongwanich, "A comprehensive review on supercapacitor applications and developments," *Energies*, vol. 15, p. 674, Jan. 2022.

[2] "Supercapacitor market size, share. future analysis and trends by 2027." `https://www.alliedmarketresearch.com/supercapacitor-market`, 2020. [Accessed 30-Jun-2023].

[3] S. Huang, X. Zhu, S. Sarkar, and Y. Zhao, "Challenges and opportunities for supercapacitors," *APL Materials*, vol. 7, Oct. 2019.

[4] Y. Shao, M. F. El-Kady, J. Sun, Y. Li, Q. Zhang, M. Zhu, H. Wang, B. Dunn, and R. B. Kaner, "Design and mechanisms of asymmetric supercapacitors," *Chem. Rev.*, vol. 118, pp. 9233–9280, Sept. 2018.

[5] Y. Gogotsi and P. Simon, "Materials science. true performance metrics in electrochemical energy storage," *Science*, vol. 334, pp. 917–918, Nov. 2011.

Chapter 2

Literature Review

Increasing demand in the need for global-energy drives the development of alternative or non-conventional energy sources with high power and energy densities. Batteries, fuel cells and supercapacitors are typical non-conventional energy devices which are based on the principle of electrochemical energy conversion. They find widespread applications in consumer electronics ranging from mobile phones, laptops, digital cameras, emergency doors and hybrid vehicles etc. In these devices, chemical energy is converted into electrical energy by means of electrochemical reactions. For fuel cells, as long as the fuel is fed, electrical energy can be obtained. In the case of batteries, the stored energy can be drawn at the time of need. A supercapacitor is a typical energy storage device (similar to a secondary battery) which possesses high specific capacitance, high power density and long cycle life [1].

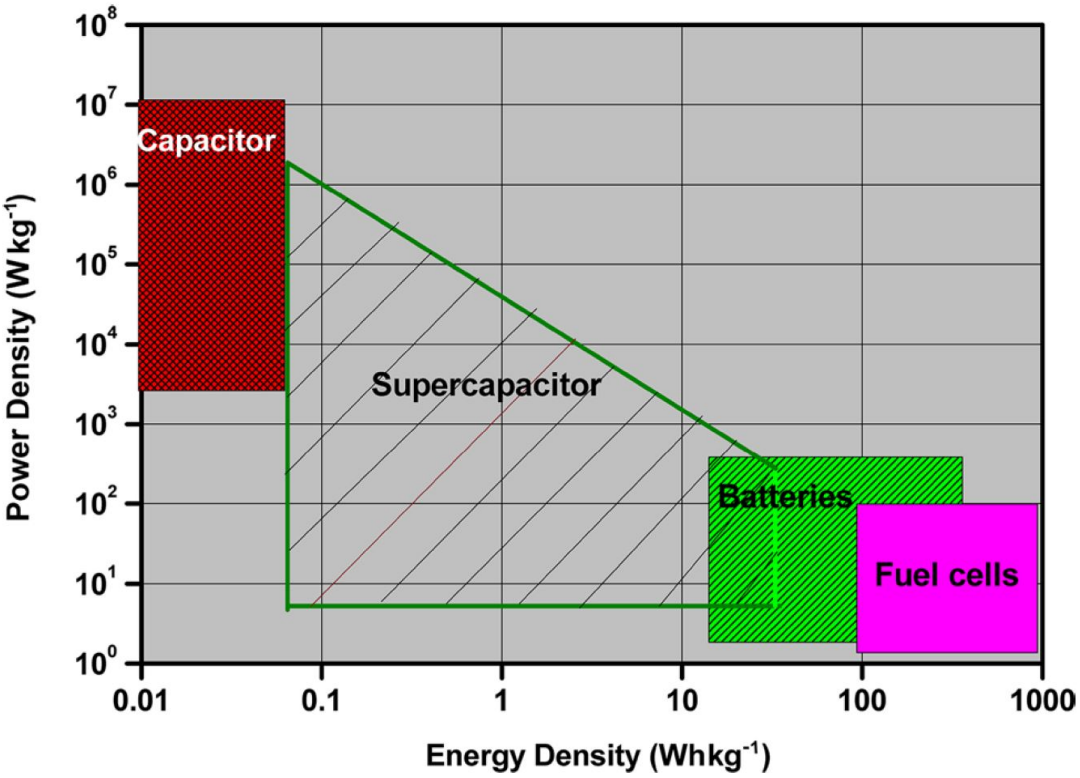

FIGURE 2.1: Ragone plot for various electrical energy storage devices (specific power against specific energy).Reprinted with permission from [1].

Electrical energy can be stored in two fundamentally different ways:

Indirectly in batteries as potentially available chemical energy requiring Faradaic oxidation and reduction of the electrochemically active reagents to release charges that can perform electrical work when they flow between two electrodes having different electrode potentials (i.e., across the voltage difference between the poles of battery cells).

Directly, in an electrostatic way, as negative and positive electric charges on the plates of a capacitor, a process known as non-Faradaic electrical energy storage [2].

A notable distinction between capacitors and batteries lies in their kinetic properties. Unlike capacitors, batteries often experience significant phase transformations in their electrodes during the cycling process [3]. While intercalation systems may exhibit minimal phase changes, they still tend to result in kinetic and thermodynamic irreversibility [4]. On the other hand, double layer capacitors simply require electrostatic charge accommodation and involve virtually no phase changes [3]. An important aspect of understanding the fundamental differences between supercapacitors and batteries is understanding the different mechanisms that result in energy and charge storage. As mentioned before reactions that result in this storage can be classified as Faradic or non-Faradaic in nature. Faradaic reactions mean electron transfer takes place across the double layers, resulting in a consequent change of oxidation state [3]. Current crosses the interface by means of an electrochemical reaction such as the reduction or oxidation of water or some ion. Additionally, there is electron transfer across the electrode, from a conducting bulk phase (metal electrode) to the electrolyte, or vice-versa. If electrons move to the electrolyte, the ions (or other molecules) that enter the electrode in reduced form leave as oxidized species when they return to the electrolyte phase (or alternatively to another bulk phase, such as a gas phase or solid salt). For Faradaic processes charged particles transfer across the electrode, i.e., they enter and they leave, coming from one bulk phase, and either returning to the same bulk phase, or going to another one. In this case, the charge is never progressively stored in the electrode. One of the bulk phases in contact with the electrode will be an electrolyte phase (either liquid or solid), in which ions or uncharged molecules are dissolved (or are a constituent of the solvent), but the other bulk phase can also be something else, such as a bulk metal phase, as is the case for a plating reaction [2].

In contrast, in a non-Faradaic electrode process, when current flows, we will notice that charge is progressively stored. Ions or other species that enter the electrode cannot leave. This is the case when there is no electrode reaction at all, or the electrode reaction

involves atoms that are part of the electrode structure itself, or when the reacting species is oxidized/reduced in the electrode, but then stays there. Charged particles do not cross the interface, and the current is carried by the charging and discharging of the electrical double layer.

2.1 Electric Double-Layer Capacitors

Energy storage systems (ESs) typically exhibit higher energy densities compared to conventional capacitors because they utilize the electrical double layer (EDL) effect. ESs comprise two electrodes with an electrolyte in between. When a potential is applied, ions from the electrolyte solution gather at the charged electrode's surface, resulting in the formation of the EDL. Since this phenomenon is limited to the surface, the charges stored primarily originate from the electrode's contact area with the electrolyte. Moreover, the double layer capacitance exclusively relies on electrostatic forces, enabling the achievement of high power density values.

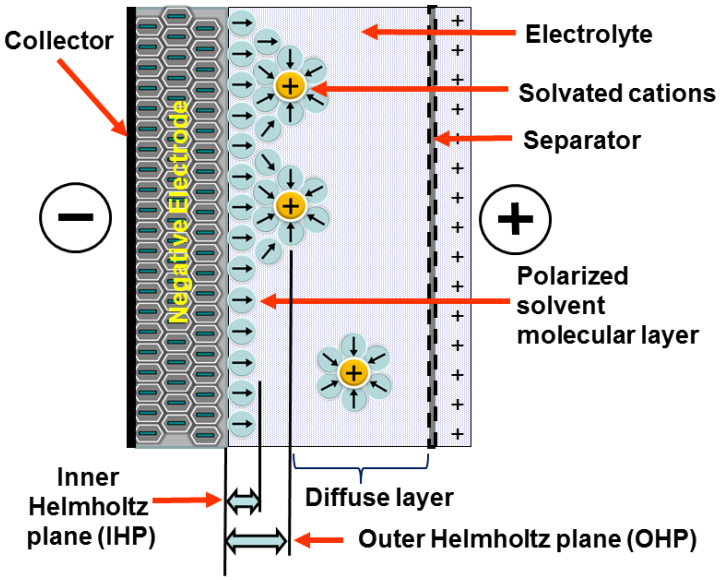

FIGURE 2.2: Schematic of an EDLC. Reprinted with permission from [5].

Figure 2.2 shows the schematic of an EDLC [5]. The establishment of the electrical double layer occurs when a metal electrode is immersed in an electrolyte solution containing solvated cations and anions. Upon immersion, the electrons within the metal migrate towards the surface in response to the presence of solvated species in the electrolyte. This migration disrupts the solution's neutrality. Initially, water molecules are the first to migrate from the electrolyte, forming an adjacent H_2O plane near the electrode's surface, known as the inner Helmholtz plane [6]. Subsequently, a plane of solvated cations emerges next to the H_2O plane, resulting in the formation of the outer Helmholtz plane, and the Helmholtz potential, V_H, which arises from the charge separation between electrons and cations [6], [7]. The high concentration of solvated cations then establishes a concentration gradient that extends into the bulk of the solution, giving rise to the Gouy-Chapman potential, V_D. Both V_D and V_H contribute to the capacitances C_D and C_H, respectively [8].

In EDLCs, energy is stored via electrostatic accumulation of charges at the electrode–electrolyte interface. During the charge/discharge processes, the arrangement of the charges in the Helmholtz double layer results in a displacement current. Since the materials can respond quickly to the change of potential and the physical reaction in nature, EDLCs can deliver energy quickly. However, due to the confinement of the electrode surface, the amount of stored energy is limited and much lower than that of pseudocapacitors and batteries. The double-layer capacitance's magnitude is approximated by Equation 2.1, where A is the electrode area, ε_0 and ε_r are the electric permittivity of free space and the relative dielectric constant of the electrolyte, respectively, and d distance from the electrode's surface to the center of the solvated cations.

$$C_{dl} = \frac{Q}{V} = \frac{\varepsilon_0 \varepsilon_r A}{d}. \tag{2.1}$$

Since the charge spacing is much smaller than that of conventional capacitors (on the scale of Angstroms) due to the distances of the Helmholtz double layer, EDLCs have a much higher theoretical capacitance. Additionally, the potential of the electrode has a linear dependence on the charge and is proportional to the area of the electrode surface covered by electroactive ions. This is why high surface area electrodes are critical in device performance.

When the constant C_{dl} is maintained for EDLCs, the subsequent equation that clarifies the response current I can be determined from the following equation.

$$I = \frac{dQ}{dt} = C_{dl}\frac{dV}{dt}. \tag{2.2}$$

The response current is directly proportional to the capacitance of the double layer and the rate at which voltage changes or sweeps. Here, t denotes the duration of charging. In the event that the applied voltage V shows a linear variation with respect to time t, such that $V = V_0 + \upsilon t$ (where V_0 denotes the initial voltage and υ signifies the sweep rate (V s^{-1} or mV s^{-1}), the correlation can be expressed as follows:

$$I = C_{dl}\upsilon. \tag{2.3}$$

The current exhibits a linear response to the sweep rate, as depicted in Equation 2.3. Consequently, this gives rise to a clearly defined rectangular plot of current (I) versus voltage (V), commonly known as a cyclic voltammogram, for diverse sweep rates (Figure 2.3 A). Conversely, if the capacitor undergoes charging or discharging with a constant current, the voltage will either increase (during charging) or decrease (during discharging) at a constant rate, as calculated by Equation 2.3. Consequently, one can anticipate a triangular charge/discharge curve, as illustrated in Figure 2.3 B [9].

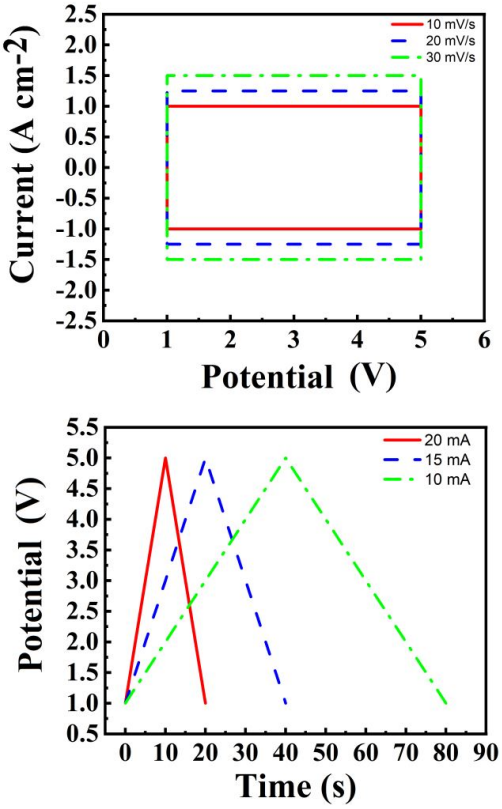

FIGURE 2.3: (Top) Cyclic voltammogram and (Bottom) charge/discharge curves for theoretically ideal EDLC.

2.2 Pseudocapacitors

The double-layer capacitance is primarily derived from the electrostatic storage of surface charge density at the interfaces of the capacitor electrode, without involving Faradaic processes. In contrast, pseudocapacitors utilize a different energy storage mechanism, characterized by rapid redox reactions taking place on or near the electrode's surface. During charging or discharging, electrosorption occurs along with charge transfer, without significant transformations in the bulk phase. Pseudocapacitance manifests at electrode surfaces, employing a distinct charge storage mechanism that differs from EDLCs. It exhibits a Faradaic nature, resembling the charge transfer observed during battery

charging or discharging. However, the capacitance is influenced by a unique thermodynamic relationship that governs the interaction between charge acceptance and potential variations [10, 11]. Furthermore, pseudocapacitance demonstrates deviations from the ideal Nernstian process typically observed in battery-type materials, as it involves faradaic reactions occurring at variable potentials [9]. The classification of pseudocapacitance involves three distinct types, and can be seen in Figure 2.4: underpotential deposition (UPD), surface redox system, and intercalation system [12].

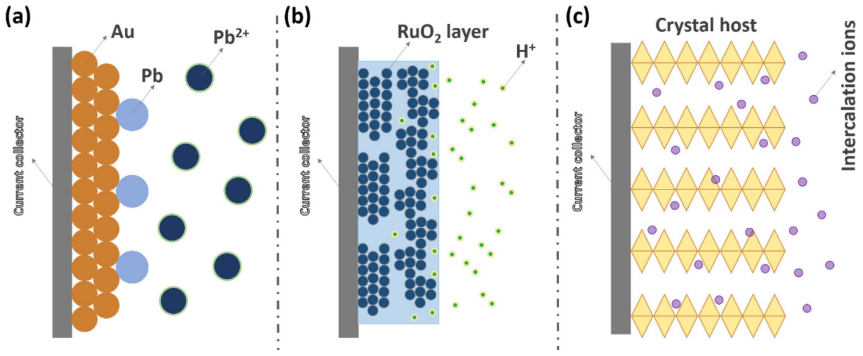

FIGURE 2.4: Types of pseudocapacitance: (a) underpotential deposition, (b) surface redox system, and (c) intercalation system. Reprinted with permission from [12].

2.2.1 Underpotential Deposition

When a potential is applied to a metal, an adsorbed monolayer will form on the surface due to the reduction of a different metal ion, resulting in a less negative potential than their equilibrium potential; this process is referred to as UPD. This results in the adsorption of metal adatoms on the surface of the electrode, and can be denoted in the following equation [3]:

$$\mathrm{M}^{n+} + \mathrm{S} + n\mathrm{e}^{-} \leftrightarrow \mathrm{SM}. \tag{2.4}$$

In the above equation, M represents a particular metal species, while S stands for a surface lattice site. In the example of figure 2.4 (a), the Pb^{2+} underpotential deposition processes taking place at a certain potential on the surface of the Au electrode can provide pseudocapacitance

2.2.2 Surface Redox System

The redox system is a typical form of pseudocapacitance, where the mechanism involves the adsorption of electroactive ions onto the surface or near-surface region of electrode materials. Faradaic charge transfer occurs between the ions in the liquid electrolyte and the active material of the solid electrode. The active layer in question has the ability to undergo rapid and reversible redox reactions. This property leads to a significant increase in capacitance through the reaction denoted as [3]:

$$\mathrm{Ox} + z\mathrm{e}^- \leftrightarrow \mathrm{Red}. \tag{2.5}$$

Equation 2.5 presents the reaction that occurs when negative charges accumulate on the electrode surface due to the movement of electrons. It is crucial to emphasize that the reactions involving the active material must be reversible. There should be no degradation of either the reactant or the product, as this fundamental characteristic distinguishes pseudocapacitive behavior from that observed in batteries [13].

2.2.3 Intercalation

Pseudocapacitance can be observed when rapid redox reactions take place due to the insertion of protons or alkali metal cations. These reactions can be represented by the following equations, where M represents a transition metal, H^+ denotes a proton, and C^+ represents an alkali metal cation [9].

$$MO_2 + H^+ + e^- \leftrightarrow MOOH. \tag{2.6}$$

$$MO_2 + C^+ + e^- \leftrightarrow MOOC. \tag{2.7}$$

During the charging/discharging process, no chemical transformation occurs. However, reversible faradaic reactions lead to the formation of a functionalized molecular layer on the electrode surface. The electrode potential shows a linear relationship with the charge and is directly proportional to the portion of the electrode surface covered by electroactive ions. Intercalation takes place when ions rapidly transfer into the tunnels or layers of a redox-active material, without causing a change in the crystallographic phase. As a result, the material maintains a highly stable structure during electrochemical reactions. It's worth noting that the previously mentioned Faradaic surface redox pseudocapacitance is limited to the material's surface, with electrolyte ions not penetrating the bulk of the electrode. However, the intercalation process allows ions to occupy the tunnels or vacancies within the material's bulk. This intercalation occurs so rapidly that it resembles the electrode reaction of a supercapacitor rather than a battery. As a result, intercalation pseudocapacitive materials typically exhibit superior rate capability compared to battery materials [9].

A big difference in galvanostatic charge and discharge profiles can be seen when comparing intercalation pseudocapacitance and battery-like intercalation (figure 2.5). Intercalation pseudocapacitance exhibits a gradual sloping charge-discharge profile similar to EDLC and surface-redox pseudocapacitance, whereas battery-like intercalation processes commonly exhibit distinct plateaus in their charge-discharge profile. This discrepancy arises from the inherent occurrence of crystallographic phase transformations in battery-like intercalation materials [12].

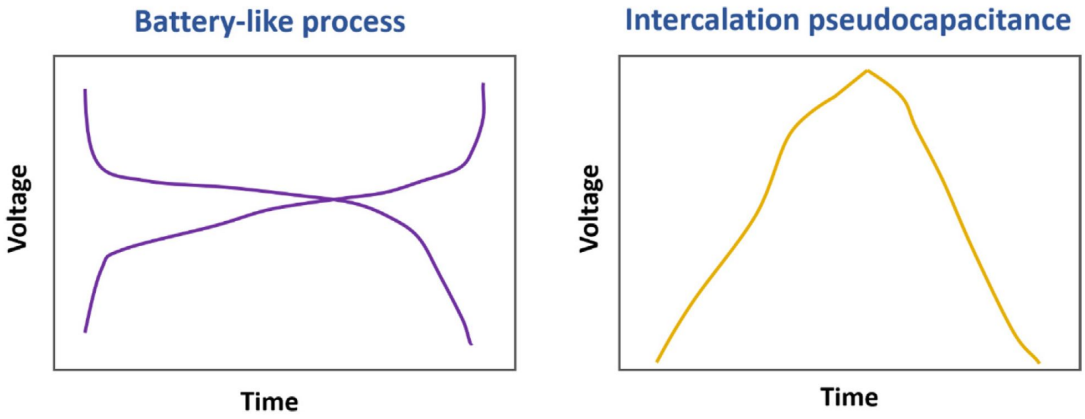

FIGURE 2.5: Difference in GCD profiles between battery-like intercalation and intercalation pseudocapacitance. Reprinted with permission from [12].

2.3 Fe_3O_4 in Supercapacitors

Transition metal oxides are commonly employed in the fabrication of electrodes for electrochemical supercapacitors, thanks to their various valence states, high capacitance, affordability, and chemical stability. Among these oxides, Fe_3O_4 exhibits promising characteristics as a pseudocapacitive material suited for the negative electrodes of supercapacitors. The redox-active properties of Fe_3O_4 stem from its oxidation states of Fe^{2+} and Fe^{3+}. However, the low electronic conductivity of Fe_3O_4 and limited access of the electrolyte to its surface hinder its specific capacitance, resulting in a notable decrease as the active mass loading increases.

To address this issue, Fe_3O_4 is combined with conductive carbon additives, which enhance the overall electronic conductivity. Several carbon materials, including activated carbon [14, 15], acetylene black [16], graphene [17, 18], graphite [19], and carbon nanotube (CNT)s [20, 21], have been incorporated into Fe_3O_4 electrodes and tested with various electrolytes such as KOH, H_2SO_4, Na_2SO_3, and Na_2SO_4. In aqueous K_2SO_4 electrolyte, asymmetric devices comprising Fe_3O_4 as the negative electrode and MnO_2

as the positive electrode have demonstrated an expanded voltage window of 1.8 V at low active masses. Notably, composite Fe_3O_4-based electrodes have reported a capacitance of 50 F g^{-1} when the mass loading was 8.8 mg cm^{-2} [22].

By utilizing distinct materials for the anode and cathode, a supercapacitor device can optimize its operational voltage window by capitalizing on the unique potential ranges offered by each electrode [23]. However, the negative electrodes display a significantly lower gravimetric capacitance than the positive electrodes, leading to a greater active mass in the negative electrode needed to match the capacitance of the positive electrode. To make an efficient device, the values of the capacitance of the anode and cathode must be matched due to the inverse relationship to total capacitance seen in equation 2.8.

$$\frac{1}{C_{total}} = \frac{1}{C_{anode}} + \frac{1}{C_{cathode}}. \tag{2.8}$$

The development of supercapacitor devices has yielded cathode materials that exhibit high capacitive properties. Therefore, research must be done to improve the capacitive properties of anode materials to closely match the typically higher capacitance seen in cathode materials such as MnO_2 and Mn_2O_3. Functionally decorated CNTs combined with energy storage materials allowed for significant improvement in the capacity, cyclic stability, and decrease in contact resistance between active materials and current collectors in batteries [24]. The increase in electrode performance seen with functionally decorated CNT makes their use with Fe_3O_4 very promising.

2.4 Dispersing and capping agents

The utilization of molecules as dispersing and capping agents has shown great potential in mitigating agglomeration and improving the stability of dispersed systems. The

undesirable phenomenon of particle clustering, known as agglomeration, poses a significant challenge in achieving uniform dispersion and stable colloidal systems. Molecules with specific functionalities and surface properties have been explored as effective tools to overcome agglomeration and enhance the stability of dispersed systems. A variety of dispersing agents, such as surfactants, polymers, and biomolecules, have been investigated for their ability to prevent agglomeration and improve the dispersion of nanoparticles or particles in various media. By adsorbing onto the particle surfaces, these additives, utilize long polymer chains or specifically tailored functional groups to provide steric or electrostatic stabilization, leading to improved dispersion and reduced agglomeration [25]. These additives play a crucial role in controlling the interparticle interactions, reducing the van der Waals forces, and promoting long-term stability of the colloidal system.

Furthermore, the use of capping agents has emerged as an effective strategy to prevent agglomeration and control the growth of nanoparticles.By adsorbing onto the particle surface, these molecules effectively act as growth inhibitors, limiting the growth of large particles and promoting the formation of desired nanostructures. The presence of these adsorbed molecules hinders the diffusion of precursor species to the particle surface, thereby preventing the incorporation of additional atoms or molecules and impeding particle growth [26]. The precise control over the growth of particles provided by capping agents allows for the synthesis of nanoparticles with controlled sizes and narrow size distributions. This control enables the production of nanoparticles with tailored properties and specific applications, such as enhanced catalytic activity, improved optical properties, or unique magnetic behavior. Overall, the adsorption of capping agents onto the particle surface during synthesis serves as an effective means to control particle growth and obtain nanoparticles with well-defined sizes and properties.

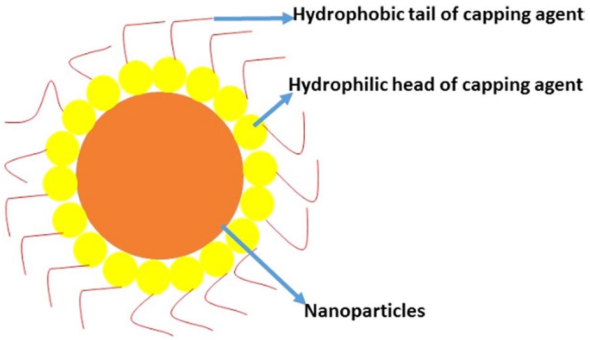

FIGURE 2.6: Nanoparticles covalently bound with capping agents. Reprinted with permission from [27].

2.5 Density Functional Theory

DFT is a widely used computational method in condensed matter physics and materials science to study the electronic structure and properties of materials. It provides a theoretical framework to calculate the ground-state energy of a system based on the electron density distribution. The foundation of DFT lies in the Hohenberg-Kohn theorems [28, 29]. These theorems examine the relationship between the density of particles, their Hamiltonian, and external potential in a particle-based system [30].

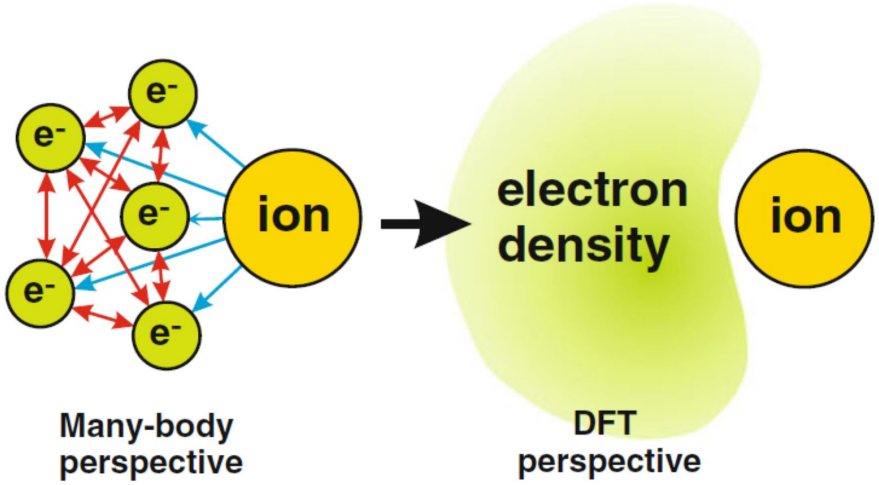

FIGURE 2.7: Schematic representation of the fundamental concept behind DFT, which addresses the challenges of the many-body problem by utilizing an electron density description rather than explicitly modeling each electron-electron interaction. Reprined with permission from [31].

The first theorem establishes that the value of the external potential is solely determined by the ground-state particle density within it. This theorem also states that many-body wavefunctions exhibiting a constant energy change can effectively describe both excited and ground states. The Hamiltonian relies on electron density as its foundation, enabling precise predictions of the system's characteristics [30].

The second theorem asserts the possibility of constructing a universal functional, denoted as $F[n]$, for the energy of the system in terms of its density. This functional is applicable to *any* external potential. This then implies that the ground-state energy of the system can be expressed as a function of its density, while considering the influence of the electron density and the external potential [30, 32].

$$E[n] = F[n] + \int \rho(r) v_{ext}(r) dr. \tag{2.9}$$

Based on these theorems, it can be concluded that the determination of the exact ground-state energy in the system involves finding the global minimum of the functional $F[n]$, considering all possible external potentials. The density that minimizes this functional corresponds to the precise ground-state density. By manipulating the functional in relation to density, we are able to accurately obtain the ground-state density and energy of the system. This theorem also highlights that by solely utilizing the functional $F[n]$, without any additional information, we can effectively determine the exact ground-state energy or density [30].

In practical applications, the Kohn-Sham formulation of DFT is commonly employed. The Kohn-Sham formulation simplifies the calculation of the groundstate energy and density by replacing the complex Hamiltonian system with a much simpler auxilliary one, introducing a set of fictitious non-interacting electrons with the same electron density as the real system. These auxiliary particles are governed by an effective potential, which consists of the external potential and an exchange-correlation potential. The exchange-correlation potential accounts for the electron-electron interactions and is typically approximated using various exchange-correlation functionals [32].

The Kohn-Sham formulation transforms the many-body Schrödinger equation into a set of single-particle equations known as the Kohn-Sham equations. Kohn and Shams idea was that, if one can find a system of non-interacting electrons that produces the same electronic density of the interacting system, then the kinetic energy of the non-interacting system can be calculated exactly. Using this kinetic energy $T[n]$, the universal density functional $F[n]$ can be written [30, 32]:

$$F[n] = T[n] + \frac{1}{2}\int\int \frac{\rho(r)\rho(r')}{|r-r'|}drdr' + E_{XC}[n], \tag{2.10}$$

containing the kinetic energy term, Coulomb interaction term, and exchange-correlation energy term, respectively.

By substituting this expression for $F[n]$ into the total energy functional (equation 2.9), we obtain the Kohn-Sham functional, written as [29, 32],

$$E_{KS}[n] = T[n] + \frac{1}{2}\int\int \frac{\rho(r)\rho(r')}{|r-r'|}drdr' + \int \rho(r)\upsilon_{ext}(r)dr + E_{XC}[n], \tag{2.11}$$

which can be rewritten to contain the interactions that formulate the total ground-state energy [33, 32],

$$E[n] = T[n] + U_{ee}[n] + V_{ext}[n] + E_{XC}[n], \tag{2.12}$$

where $T[n]$ is the kinetic energy, $U_{ee}[n]$ is the Coulomb self-interaction of the electron density, $V_{ext}[n]$ is the electron–nuclear interaction energy, and $E_{XC}[n]$ is the exchange-correlation energy [33, 32].

These equations can be solved self-consistently to obtain the electron wavefunctions and energies of the auxiliary particles. The ground-state electron density is then determined from these wavefunctions. By treating the interacting system as a set of non-interacting particles, the Kohn-Sham formulation allows for a computationally manageable solution to the DFT problem. It enables the calculation of various properties and observables of the system based on the electron density obtained from the auxiliary particles.

In summary, the Kohn-Sham functional allows for the calculation of groundstate energy of a system by considering the kinetic energy term, the electron-electron interaction term, the external potential term, and the exchange-correlation term. The kinetic energy term, $T[n]$, represents the energy associated with the motion of electrons in the system. It accounts for the quantum mechanical effects of electron wavefunctions and their corresponding kinetic energy operators. The electron-electron interaction term, U_{ee}, takes into account the repulsive Coulomb interactions between electrons. It considers the

electrostatic potential energy resulting from the mutual repulsion of electrons. The external potential term, V_{ext}, accounts for the interaction between the electrons and the external potential, such as the electrostatic potential generated by atomic nuclei or an applied electric field. It describes the energy of electrons in the presence of this external potential. Finally, the exchange-correlation term, E_{XC}, includes the electron-electron interactions not covered in the repulsive Coulomb interactions. It incorporates both the exchange and correlation effects of electron-electron interactions. The exchange term describes the quantum mechanical effect that arises when two electrons interchange their positions. The correlation term accounts for the additional electron-electron interactions beyond the simple Coulomb repulsion.

A self-consistent field (SCF) method is used to compute the ground-state energy of a system using the total energy functional and the electron density. An initial estimation of the electron density (n_0) of the system is needed to start. This initial electron density is used to solve the Kohn-Sham equations to obtain electron wavefunctions and determine a new electron density (n_1). This new electron density is compared with the previous guess. If they are sufficiently close, the iteration process stops, and the calculated electron density is considered the converged ground-state electron density. If the electron densities are not close enough, the electron density (n_0) is updated with the new density (n_1) and the process is repeated. This process will continue through several iterations until the electron density converges within the desired accuracy and the iteration process stops. Through this iterative process, the ground-state energy is determined by repeatedly updating the electron density and solving the Kohn-Sham equations until self-consistency is achieved. This approach ensures that the electron density corresponds to the lowest total energy, representing the ground state of the system within the approximations used in the exchange-correlation functionals [30, 32, 34].

2.5.1 Local Density Approximation

The local density approximation (LDA) [29] assumes that the exchange-correlation energy depends only on the local electron density and does not consider the spatial gradients of the density, resulting in a simpler and computationally less expensive approach compared to more advanced functionals. However, this simplicity comes at the cost of reduced accuracy in capturing certain electronic and structural properties, particularly those influenced by electron delocalization or strong electron-electron interactions [35, 36].

To apply the LDA, the electron density is divided into small regions, and the exchange-correlation energy is approximated separately for each region based on its local density. The local energy terms are determined by integrating the energy density over the volume of the system. This integration is performed by evaluating the energy density at each point r in the volume and multiplying it by the corresponding electronic density value at that point. By integrating over the entire volume, the contributions from different regions of the system are combined to obtain the local energy terms. This approach allows for the consideration of localized energy effects that depend on the specific electronic density distribution within the system. By evaluating the energy density at each point and integrating over the volume, the local energy terms capture the variations in energy associated with different electron density values throughout the system [32, 35].

The LDA approach has been found to be particularly effective for systems with slowly varying electron densities, such as nearly free-electron metals, molecules, and semiconductors, where the local approximation remains reasonably accurate [37]. While the LDA provides a computationally efficient approach to estimating the exchange-correlation energy in DFT, it does have limitations. Since it relies solely on local electron densities, it neglects non-local effects and correlations that can occur over longer distances. This can lead to inaccuracies, especially in systems with rapidly varying electron densities or

strong electron-electron correlations. To overcome these limitations, more sophisticated and accurate exchange-correlation functionals, such as the generalized gradient approximation (GGA) [38] and hybrid functionals, have been developed. However, the Local Density Approximation remains a valuable and widely used tool in DFT, particularly for systems where the electron density varies slowly [32].

2.5.2 Generalized Gradient Approximation

The GGA is a widely used approach in DFT calculations to approximate the exchange-correlation energy functional. GGA aims to improve upon the LDA by incorporating information about the gradient of the electron density. In LDA, the exchange-correlation functional is solely based on the local electron density at each point in space. However, GGA takes into account not only the local electron density but also the spatial variations of the density. By considering the gradient of the electron density, GGA provides a more accurate description of the exchange-correlation energy and, consequently, the total energy of the system. This improved treatment of the exchange-correlation functional leads to more accurate predictions of various electronic, structural, and energetic properties of materials by providing superior chemical accuracies, improved predictions of binding energies, and more accurate estimations of bond lengths and angles which are critical in predicting lattice parameters [39, 40, 41, 42]. The most commonly used GGA functionals include the Perdew, Burke, and Ernzerhof (PBE) [43] functional, the revised PBE (RPBE) [44] functional, and the Becke-Lee-Yang-Parr (BLYP) [45] functional. These functionals have been successfully applied in a wide range of systems, including molecules, solids, and surfaces, enabling reliable predictions of structural, electronic, and spectroscopic properties within DFT calculations [32]. In addition to exchange-correlation effects, pseudopotentials are implemented in electronic structure calculations to reduce computational cost and enhance computational efficiency.

2.5.3 Pseudopotentials

Pseudopotentials are valuable assets in DFT, enabling efficient calculations and providing accurate descriptions of materials electronic structures for studying a broad range of physical and chemical phenomena. Pseudopotentials are commonly employed to simplify electronic structure calculations by treating core electrons as fixed and efficiently representing the interaction between valence electrons and atomic nuclei. A distinction is made between valence and core electrons, and by implementing atomic pseudopotentials, the effective nucleus is represented as the nucleus combined with its core electrons, reducing the computational burden. Pseudopotentials are designed to accurately capture valence electron behavior while approximating the interaction with ionic cores, accounting for core electron screening effects. They are generated using theoretical techniques, such as the projector-augmented wave (PAW) method, ensuring an accurate representation of the atomic electronic structure while minimizing computational demands. Incorporating pseudopotentials into DFT calculations enhances computational efficiency, enabling the study of larger and more complex systems [32, 46, 47].

Bibliography

[1] P. E. Lokhande, U. S. Chavan, and A. Pandey, "Materials and fabrication methods for electrochemical supercapacitors: Overview," *Electrochem. Energy Rev.*, vol. 3, pp. 155–186, Mar. 2020.

[2] P. M. Biesheuvel, S. Porada, and J. E. Dykstra, "The difference between faradaic and non-faradaic electrode processes," 2021.

[3] B. E. Conway, *Electrochemical Supercapacitors*. Boston, MA: Springer US, 1999.

[4] R. C. Massé, C. Liu, Y. Li, L. Mai, and G. Cao, "Energy storage through intercalation reactions: electrodes for rechargeable batteries," *Natl. Sci. Rev.*, vol. 4, pp. 26–53, Jan. 2017.

[5] O. Haas and E. J. Cairns, "Chapter 6. electrochemical energy storage," *Annu. Rep. Prog. Chem., Sect. C: Phys. Chem.*, vol. 95, pp. 163–198, 1999.

[6] J. Wu, "Understanding the electric double-layer structure, capacitance, and charging dynamics," *Chem. Rev.*, vol. 122, pp. 10821–10859, June 2022.

[7] D. Govindarajan and K. K. Chinnakutti, "Fundamentals, basic components and performance evaluation of energy storage and conversion devices," in *Oxide Free Nanomaterials for Energy Storage and Conversion Applications*, pp. 51–74, Elsevier, 2022.

[8] K. Doblhoff-Dier and M. T. M. Koper, "Modeling the Gouy–Chapman diffuse capacitance with attractive ion–surface interaction," *J. Phys. Chem. C Nanomater. Interfaces*, vol. 125, pp. 16664–16673, Aug. 2021.

[9] J. Liu, J. Wang, C. Xu, H. Jiang, C. Li, L. Zhang, J. Lin, and Z. X. Shen, "Advanced energy storage devices: Basic principles, analytical methods, and rational materials design," *Adv. Sci. (Weinh.)*, vol. 5, p. 1700322, Jan. 2018.

[10] T. Brousse, D. Bélanger, and J. W. Long, "To be or not to be pseudocapacitive?," *J. Electrochem. Soc.*, vol. 162, no. 5, pp. A5185–A5189, 2015.

[11] Y. Jiang and J. Liu, "Definitions of pseudocapacitive materials: A brief review," *Energy Environ. Mater.*, vol. 2, pp. 30–37, Mar. 2019.

[12] Y. Liu, S. P. Jiang, and Z. Shao, "Intercalation pseudocapacitance in electrochemical energy storage: recent advances in fundamental understanding and materials development," *Mater. Today Adv.*, vol. 7, p. 100072, Sept. 2020.

[13] Y. Gogotsi and R. M. Penner, "Energy storage in nanomaterials - capacitive, pseudocapacitive, or battery-like?," *ACS Nano*, vol. 12, pp. 2081–2083, Mar. 2018.

[14] X. Du, C. Wang, M. Chen, Y. Jiao, and J. Wang, "Electrochemical performances of nanoparticle Fe_3O_4/activated carbon supercapacitor using KOH electrolyte solution," *J. Phys. Chem. C Nanomater. Interfaces*, vol. 113, pp. 2643–2646, Feb. 2009.

[15] N. Sinan and E. Unur, "Fe3O4/carbon nanocomposite: Investigation of capacitive & magnetic properties for supercapacitor applications," *Mater. Chem. Phys.*, vol. 183, pp. 571–579, Nov. 2016.

[16] Y. Zeng, M. Yu, Y. Meng, P. Fang, X. Lu, and Y. Tong, "Iron-based supercapacitor electrodes: Advances and challenges," *Advanced Energy Materials*, vol. 6, 08 2016.

[17] A. K. Mishra and S. Ramaprabhu, "Functionalized graphene-based nanocomposites for supercapacitor application," *J. Phys. Chem. C Nanomater. Interfaces*, vol. 115, pp. 14006–14013, July 2011.

[18] S. Sheng, W. Liu, K. Zhu, K. Cheng, K. Ye, G. Wang, D. Cao, and J. Yan, "Fe3O4 nanospheres in situ decorated graphene as high-performance anode for asymmetric supercapacitor with impressive energy density," *J. Colloid Interface Sci.*, vol. 536, pp. 235–244, Feb. 2019.

[19] H. Sayahi, F. Mohsenzadeh, H. R. Darabi, and K. Aghapoor, "Facile and economical fabrication of magnetite/graphite nanocomposites for supercapacitor electrodes with significantly extended potential window," *J. Alloys Compd.*, vol. 778, pp. 633–642, Mar. 2019.

[20] A. K. Mishra and S. Ramaprabhu, "Magnetite decorated multiwalled carbon nanotube based supercapacitor for arsenic removal and desalination of seawater," *J. Phys. Chem. C Nanomater. Interfaces*, vol. 114, pp. 2583–2590, Feb. 2010.

[21] Q. Wang, L. Jiao, H. Du, Y. Wang, and H. Yuan, "Fe3O4 nanoparticles grown on graphene as advanced electrode materials for supercapacitors," *J. Power Sources*, vol. 245, pp. 101–106, Jan. 2014.

[22] T. Brousse and D. Bélanger, "A hybrid fe3o4-mno2 capacitor in mild aqueous electrolyte," *Electrochem. Solid State Letters*, vol. 6, no. 11, p. A244, 2003.

[23] Y. Shao, M. F. El-Kady, J. Sun, Y. Li, Q. Zhang, M. Zhu, H. Wang, B. Dunn, and R. B. Kaner, "Design and mechanisms of asymmetric supercapacitors," *Chem. Rev.*, vol. 118, pp. 9233–9280, Sept. 2018.

[24] P. Forouzandeh, V. Kumaravel, and S. C. Pillai, "Electrode materials for supercapacitors: A review of recent advances," *Catalysts*, vol. 10, p. 969, Aug. 2020.

[25] F. O. Pirrung, P. H. Quednau, and C. Auschra, "Wetting and dispersing agents," *CHIMIA*, vol. 56, p. 170, May 2002.

[26] C. M. Phan and H. M. Nguyen, "Role of capping agent in wet synthesis of nanoparticles," *The Journal of Physical Chemistry A*, vol. 121, pp. 3213–3219, Apr. 2017.

[27] R. Javed, M. Zia, S. Naz, S. O. Aisida, N. ul Ain, and Q. Ao, "Role of capping agents in the application of nanoparticles in biomedicine and environmental remediation: recent trends and future prospects," *Journal of Nanobiotechnology*, vol. 18, Nov. 2020.

[28] P. Hohenberg and W. Kohn, "Inhomogeneous electron gas," *Phys. Rev.*, vol. 136, pp. B864–B871, Nov 1964.

[29] W. Kohn and L. J. Sham, "Self-consistent equations including exchange and correlation effects," *Phys. Rev.*, vol. 140, pp. A1133–A1138, Nov 1965.

[30] R. M. Martin, *Electronic structure: Basic theory and practical methods*. Cambridge University Press, second ed., 2020.

[31] M. T. Lusk and A. E. Mattsson, "High-performance computing for materials design to advance energy science," *MRS Bull.*, vol. 36, pp. 169–174, Mar. 2011.

[32] J. Kohanoff, *Electronic structure calculations for solids and molecules: Theory and computational methods*. Cambridge University Press, 2006.

[33] B. Miller and D. Ginev, "5.2 kohn-sham density functional theory 2023; chapter 5 density functional theory 2023." `https://manual.q-chem.com/5.2/Ch5.S2.html`, 2011. [Accessed 15-Jun-2023].

[34] E. Kaxiras, *Atomic and electronic structure of solids*. Cambridge University Press, second ed., 2011.

[35] D. H. Gebremedhin and C. A. Weatherford, "Application of the space-pseudo-time method to density functional theory," in *Advances in Quantum Chemistry*, Advances in quantum chemistry, pp. 231–247, Elsevier, 2016.

[36] V. Sahni, K. P. Bohnen, and M. K. Harbola, "Analysis of the local-density approximation of density-functional theory," *Phys. Rev. A*, vol. 37, pp. 1895–1907, Mar 1988.

[37] G.-X. Zhang, A. M. Reilly, A. Tkatchenko, and M. Scheffler, "Performance of various density-functional approximations for cohesive properties of 64 bulk solids," *New Journal of Physics*, vol. 20, p. 063020, June 2018.

[38] J. P. Perdew, K. Burke, and M. Ernzerhof, "Generalized gradient approximation made simple," *Phys. Rev. Lett.*, vol. 77, pp. 3865–3868, Oct 1996.

[39] T. J. Giese and D. M. York, "Density-functional expansion methods: Evaluation of LDA, GGA, and meta-GGA functionals and different integral approximations," *The Journal of Chemical Physics*, vol. 133, p. 244107, Dec. 2010.

[40] D. C. Patton, M. R. Pederson, and D. V. Porezag, "The generalized-gradient approximation to density functional theory and bonding," in *Frontiers in Materials Modelling and Design*, pp. 37–50, Springer Berlin Heidelberg, 1998.

[41] D. Rappoport, N. R. M. Crawford, F. Furche, and K. Burke, "Approximate density functionals: Which should i choose?," Sept. 2009.

[42] Š. Masys and V. Jonauskas, "On the crystalline structure of orthorhombic SrRuO3: A benchmark study of DFT functionals," *Computational Materials Science*, vol. 124, pp. 78–86, Nov. 2016.

[43] J. P. Perdew, K. Burke, and M. Ernzerhof, "Generalized gradient approximation made simple," *Phys. Rev. Lett.*, vol. 77, pp. 3865–3868, Oct 1996.

[44] M. Ernzerhof and G. E. Scuseria, "Assessment of the Perdew–Burke–Ernzerhof exchange-correlation functional," *The Journal of Chemical Physics*, vol. 110, pp. 5029–5036, 03 1999.

[45] A. D. Becke, "Density-functional exchange-energy approximation with correct asymptotic behavior," *Physical Review A*, vol. 38, pp. 3098–3100, Sept. 1988.

[46] G. Kresse and D. Joubert, "From ultrasoft pseudopotentials to the projector augmented-wave method," *Physical Review B*, vol. 59, pp. 1758–1775, Jan. 1999.

[47] R. M. Martin, L. Reining, and D. M. Ceperley, *Interacting electrons: Theory and computational approaches*. Cambridge University Press, 2016.

Chapter 3

Problem Statement

The performance improvement of supercapacitor anodes based on Fe_3O_4 requires addressing two major challenges: enhancing the capacitive properties of Fe_3O_4 to match the high performance of cathode materials and overcoming agglomeration issues during electrode fabrication.

Achieving a balanced capacitance between the anode and cathode is crucial for maximizing the overall energy storage capacity of a supercapacitor device. Currently, cathode materials have demonstrated superior capacitive properties, while the gravimetric capacitance of Fe_3O_4-based anodes remains relatively low. To bridge this gap, extensive research is needed to improve the capacitive properties of Fe_3O_4 anode materials, aiming to closely match the performance seen in cathode materials. Such improvements can be achieved through strategies like nanostructuring, surface modification, and utilization of carbon-based additives to enhance electronic conductivity and electrolyte accessibility, thereby increasing the specific capacitance of Fe_3O_4.

Recently, Fe_3O_4 has emerged as a promising anode material due to its high theoretical capacitance, low cost, and environmentally benign nature [1]. The interest in the investigation of nanostructured Fe_3O_4 is fueled by the possibility to combine advanced ferrimagnetic and pseudocapacitive properties in a single material. However, due to the low electronic conductivity of Fe_3O_4 and poor electrolyte access to the material surface, the specific capacitance decreases significantly with increasing active mass loading [2], making it a poor choice as a standalone material for electrodes in supercapacitors.

The fabrication of supercapacitor anodes using Fe_3O_4 encounters the challenge of agglomeration. The ferrimagnetic nature of Fe_3O_4 and the strong Van der Waals interactions present among CNTs [3] lead to the formation of agglomerates. These agglomerates negatively impact electrode performance by reducing surface area, hindering ion diffusion, and increasing charge transport resistance.

Bibliography

[1] L. Wang, H. Ji, S. Wang, L. Kong, X. Jiang, and G. Yang, "Preparation of fe3o4 with high specific surface area and improved capacitance as a supercapacitor," *Nanoscale*, vol. 5, no. 9, p. 3793, 2013.

[2] M. Nawwar, R. Poon, R. Chen, R. P. Sahu, I. K. Puri, and I. Zhitomirsky, "High areal capacitance of fe_3o_4-decorated carbon nanotubes for supercapacitor electrodes," *Carbon Energy*, vol. 1, pp. 124–133, Sept. 2019.

[3] D. Guan, Z. Gao, W. Yang, J. Wang, Y. Yuan, B. Wang, M. Zhang, and L. Liu, "Hydrothermal synthesis of carbon nanotube/cubic fe3o4 nanocomposite for enhanced performance supercapacitor electrode material," *Materials Science and Engineering: B*, vol. 178, pp. 736–743, June 2013.

Chapter 4

Objectives

The research presented in this thesis aims to address key challenges in the development of supercapacitors by investigating the utilization of dispersing and capping agents during the synthesis of Fe_3O_4 nanoparticles. These agents play a crucial role in controlling nanoparticle size and reducing the agglomeration of particles, thereby enhancing the performance of supercapacitor electrodes. Specifically, the goal is to utilize novel additives, including dispersing agents and CNTs as conductive additives, to reduce the particle size of Fe_3O_4 and increase the surface area of active anode materials. The use of dispersing and capping agents during the synthesis of Fe_3O_4 nanoparticles plays a vital role in controlling particle size and preventing agglomeration. These agents enable precise control over the growth and dispersion of nanoparticles, leading to uniform and stable electrode structures.

Addressing these challenges requires a comprehensive understanding of the underlying mechanisms governing the capacitive properties of Fe_3O_4 and the agglomeration

phenomenon. Through experimental investigations and computational simulations, insights can be gained into the structural, electronic, and surface properties of Fe_3O_4 and the interactions with additives and dispersing agents. These insights will guide the development of effective strategies to optimize the synthesis, dispersion, and electrode fabrication processes, ultimately leading to improved performance and commercial viability of Fe_3O_4-based supercapacitors

Innovative approaches involving dispersing and capping agents are employed during the synthesis of Fe_3O_4 nanoparticles and the electrode fabrication process. These agents can effectively disperse the Fe_3O_4 nanoparticles and CNTs, preventing their agglomeration and ensuring uniform distribution within the electrode matrix. The controlled dispersion of Fe_3O_4 nanoparticles and CNTs will enable the formation of well-defined electrode structures with enhanced electrochemical performance.

The investigation of the adsorption process of dispersant molecules will be conducted using DFT simulations. This approach provides valuable insights into the chemical processes that occur during adsorption, shedding light on the mechanisms governing the dispersion and stability of Fe_3O_4 nanoparticles.

By addressing these research objectives, this thesis aims to contribute to the development of improved supercapacitor electrodes by controlling nanoparticle size and reducing particle agglomeration. The utilization of novel dispersing and capping agents, along with insights gained from DFT simulations, will pave the way for enhanced electrode performance and ultimately advance the field of supercapacitor technology.

Chapter 5

Supercapacitor Performance of Magnetite Nanoparticles Enhanced by a Catecholate Dispersant: Experiment and Theory

Coulton Boucher

Oleg Rubel

Igor Zhitomirsky

Molecules 2023, 28(4), 1562;

https://doi.org/10.3390/molecules28041562

Published: 6 February 2023

5.1 Abstract

The full potential of Fe_3O_4 for supercapacitor applications can be achieved by addressing challenges in colloidal fabrication of high active mass electrodes. Exceptional adsorption properties of catecholate-type 3,4-dihydroxybenzoic acid (DHBA) molecules are explored for surface modification of Fe_3O_4 nanoparticles to enhance their colloidal dispersion as verified by sedimentation test results and Fourier-transform infrared spectroscopy measurements. Electrodes prepared in the presence of DHBA show nearly double capacitance at slow charging rates as compared to the control samples without the dispersant or with benzoic acid as a non-catecholate dispersant. Such electrodes with active mass of 40 mg cm^{-2} show a capacitance of 4.59 F cm^{-2} from cyclic voltammetry data at a scan rate of 2 mV s^{-1} and 4.72 F cm^{-2} from galvanostatic charge-discharge data at a current density of 3 mA cm^{-2}. Experimental results are corroborated by density functional theory (DFT) analysis of adsorption behaviour of DHBA and benzoic acid at the (001) surface of Fe_3O_4. The strongest adsorption energy (ca. -1.8 eV per molecule) is due to the catechol group of DHBA. DFT analysis provides understanding of the basic mechanism of DHBA adsorption on the surface of nanoparticles and opens the way for fabrication of electrodes with high capacitance.

5.2 Introduction

Surface modification of materials using molecules from the catechol family is emerging as a new area of technological and scientific interest [1, 2]. Catecholate molecules can achieve extremely strong adhesion to inorganic surfaces by utilizing a similar adsorption mechanism to that of mussel proteins when bonded to different surfaces [2, 3, 4]. Very fast and very strong adsorption to various inorganic substrates is a necessity for mussels to avoid damage by sea waves. This adhesion mechanism is attributed to bonding of the catechol ligands of the mussel proteins to metal atoms on material surfaces

[4, 5, 6, 7, 8]. Polymer molecules were modified with catechol ligands for the fabrication of adherent polymer and composite films [4, 9, 10, 11, 12]. Catecholate molecules were used as charged dispersants for electrophoretic deposition of inorganic and organic materials [5, 13, 14]. Catecholate molecules were also utilized as particle transfer vehicles for liquid-liquid extraction [15], which prevented nanoparticle agglomeration. In this technology, inorganic particles were modified with catechol ligands in the synthesis medium or at the liquid- liquid interface and transferred from the synthesis medium directly to the device processing medium [15]. Catechol molecules facilitated efficient and versatile extraction [16] of MnO_2, Mn_3O_4, FeOOH, and ZnO for energy storage and sensor applications. The phase transfer of the particles resulted in reduced agglomeration, which allowed for improved electrolyte access to the particle surface [16] and improved device performance. Recent studies highlighted benefits of catecholate molecules for surface modification of materials for applications in dye-sensitized solar cells and photoelectrochemical sensors [17, 18, 19]. For dye-sensitized solar cells, a staggered gap heterojunction can occur at a catechol-TiO_2 interface [17], which facilitates electron injection into the TiO_2 semiconductor [20]. Such configurations improved dye-sensitized solar cell efficiency. Redox properties of catechol, related to oxidation of their phenolic OH groups, were used for electron transfer mediation in electrochemical biosensors [21]. Moreover, redox properties of catechol are under investigation for applications in bioelectronics [19, 22], catalysis [23], and energy storage devices [24, 25]. Enhanced capacitance has been seen in catechol-modified carbon cloth electrodes due to the additional contribution of electrochemical oxidation of catechol OH groups [26]. The ability of catechol to oxidize electrochemically to o-benzoquinone allows for many uses in electropolymerization [27, 28]. It is known that o-benzoquinone participates in polymerization reactions, including chemical oxidative polymerization [29], electrochemical oxidative polymerization [30], and bipolar electropolymerization [27], to be used in a variety of biomedical applications including targeted drug delivery to cancer cells [31], catechol-modified polymers

with antimicrobial properties [32], and structural adhesives for tissue and bone [33]. Catechol molecules can play an additional role as charge-transfer mediators [34]. The use of catecholate dopants for polypyrrole facilitated charge transfer, reduced electropolymerization potential, and allowed the fabrication of adherent polypyrrole films on non-noble substrates [35, 36, 37]. The functionalization of ferrimagnetic nanoparticles with catecholate molecules in- duced improved magnetization [38]. Other investigations reported applications of catecholate molecules for the fabrication of quantum dots and luminescent materials [39, 40]. Catecholates have generated significant interest for applications in nanotechnology as capping, reducing, and structure directing additives, which facilitated the fabrication of nanoparticles of metals and metal oxides with controlled size, shape, and functional properties [41, 42, 43, 44, 45]. Further progress in the application of catecholates in nanotechnology can result in the development of advanced functional nanomaterials for modern applications. Catecholates are of particular interest for the fabrication of devices, based on materials, combining advanced magnetic and electrical properties [41, 46, 47]. This investigation was motivated by interesting electrical charge storage properties of iron oxides, such as Fe_2O_3 and Fe_3O_4 [41, 48]. Fe_3O_4 is of particular interest for the development of multifunctional devices, based on the high capacitance and advanced ferrimagnetic properties of this material. It is known that Fe_3O_4 exhibits higher conductivity compared to many other spinel ferrimagnetic materials [49]. The relatively high conductivity of Fe_3O_4 is beneficial for electrochemical charge-discharge processes [49]. The pseudocapacitive charging mechanism of this material, containing ${Fe_2}^+$ and ${Fe_3}^+$ ions ($Fe^{2+}{Fe_2}^{3+}O_4$), is attributed to redox ${Fe_3}^+$ ${Fe_2}^+$ reactions. The charge storage properties in the positive potential range [50, 51] are attributed to oxidation of ${Fe_2}^+$ ions (${Fe_2}^+ \rightarrow {Fe_3}^+$), whereas the charging mechanism in the negative potential range is based on reduction of ${Fe_3}^+$ ions (${Fe_3}^+ \rightarrow {Fe_2}^+$) [41, 52, 53]. Fe_3O_4 is especially important for the development of negative electrodes of advanced asymmetric supercapacitors with an enlarged voltage window. Recently, significant progress

was achieved in the development of different materials for positive electrodes, which showed high capacitance [54, 55, 56]. However, lower capacitance of the negative electrodes, such as activated carbon, is a limiting factor in the development of advanced devices. The important tasks in the development of Fe_3O_4 electrodes are the fabrication of small nanoparticles and prevention of their agglomeration, which can result from Van der Waals forces and magnetic attraction forces. Moreover, efficient mixing of non-agglomerated and well-dispersed nanoparticles with conductive additives is necessary for good electrode performance. Therefore, advanced capping and dispersing agents are critically important for the synthesis of small non-agglomerated Fe_3O_4 nanoparticles and fabrication of composite electrodes. The goal of this investigation is the fabrication of Fe_3O_4 electrodes for supercapacitors using a catecholate-type 3,4-dihydroxybenzoic acid (DHBA) as a capping and dispersing agent for Fe_3O_4 nanoparticles. This goal was achieved in experimental studies of the synthesis of Fe_3O_4 particles, fabrication, and testing of supercapacitor electrodes and application of density functional theory (DFT) [57] for the analysis of the DHBA adsorption mechanism. Fe_3O_4 has emerged as a promising supercapacitor material due to its low cost and environmentally benign nature [58]. Here, we aimed at improving electrochemical performance of fabricated Fe_3O_4 supercapacitor anodes and selected DHBA as a catechol molecule to play the role of a capping and dispersing agent. The chemical structure of DHBA contains adjacent phenolic OH functional groups on the 3rd and 4th carbons on the benzene ring (Figure1), providing strong adsorption to the particle surface, while a carboxyl group can facilitate dispersion via electrostatic repulsion [59, 60]. These adsorption and dispersion properties are critical to prevent agglomeration of nanoparticles in solution, particularly materials with magnetic properties, such as Fe_3O_4. Benzoic acid (BA) is chosen as a negative control in our experimental design. The chemical structures of DHBA and BA differ only by the adjacent phenolic OH groups present in DHBA but not in BA (Figure 5.1). To corroborate the understanding of the adsorption processes seen in our

experimental results, we used DFT to model DHBA and BA adsorption on the surface of Fe_3O_4 and assess their binding affinities and mechanisms.

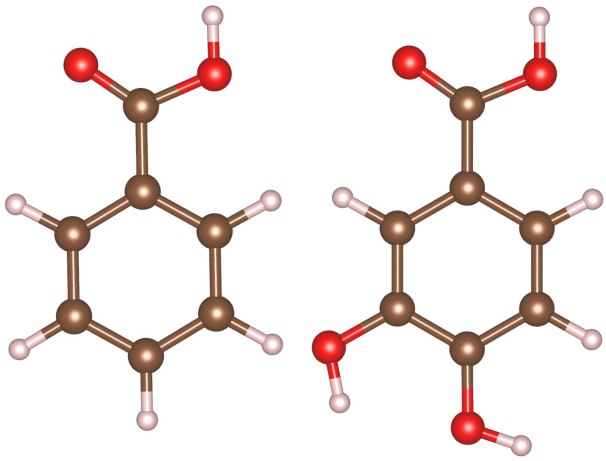

FIGURE 5.1: Chemical structure of benzoic acid (left) and 3,4-dihydroxybenzoic acid (right).

5.3 Results and Discussion

5.3.1 Experimental Results

Dispersing properties of BA and DHBA were investigated by analysing the suspension stability of Fe_3O_4 particles in water (Figure2). Fe_3O_4 suspensions without additives and containing BA showed rapid precipitation. However, the suspension prepared with DHBA as a dispersing agent remained stable, further confirming the role of the phenolic OH groups of the molecule for adsorption, which are functional groups that BA lacks. The synthesis of Fe_3O_4 was conducted at pH = 9, which is above the isoelectric point of Fe_3O_4 (pH = 6.5) [61]. Therefore, the as-prepared Fe_3O_4 particles were negatively charged. The adsorption of anionic DHBA on the negatively charged Fe_3O_4 particles indicated a strong adsorption power of the catecholate DHBA molecules.

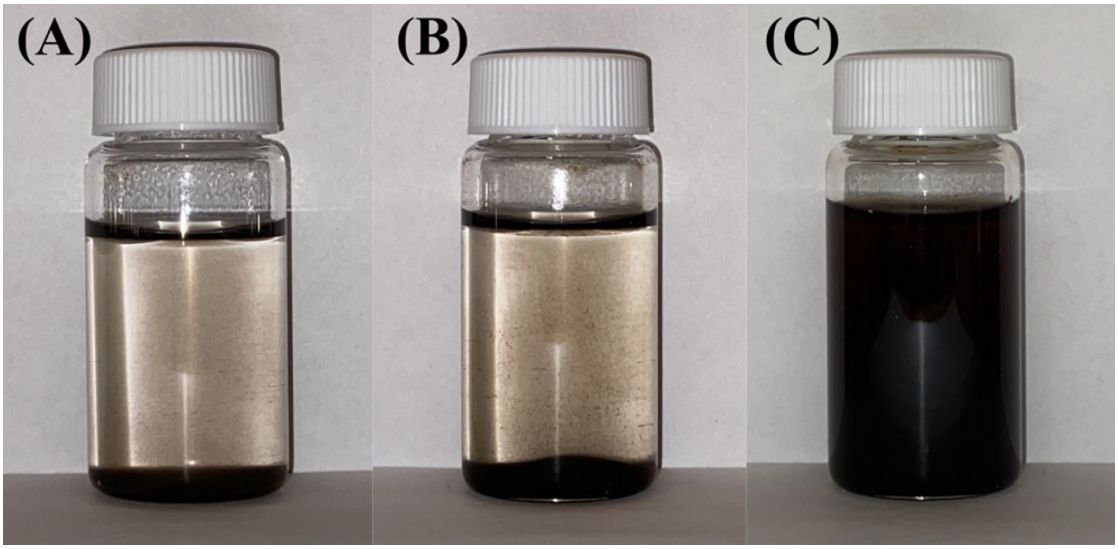

FIGURE 5.2: Fe_3O_4 suspension in water with (A) no dispersing agent, (B) BA as a dispersing agent, and (C) DHBA as a dispersing agent 1 h after ultrasonication.

The adsorption of DHBA on Fe_3O_4 particles was confirmed by results of Fourier Transform Infrared (FTIR) spectroscopy studies. Figure3compares FTIR spectra of Fe_3O_4 prepared without and with DHBA and pure DHBA.

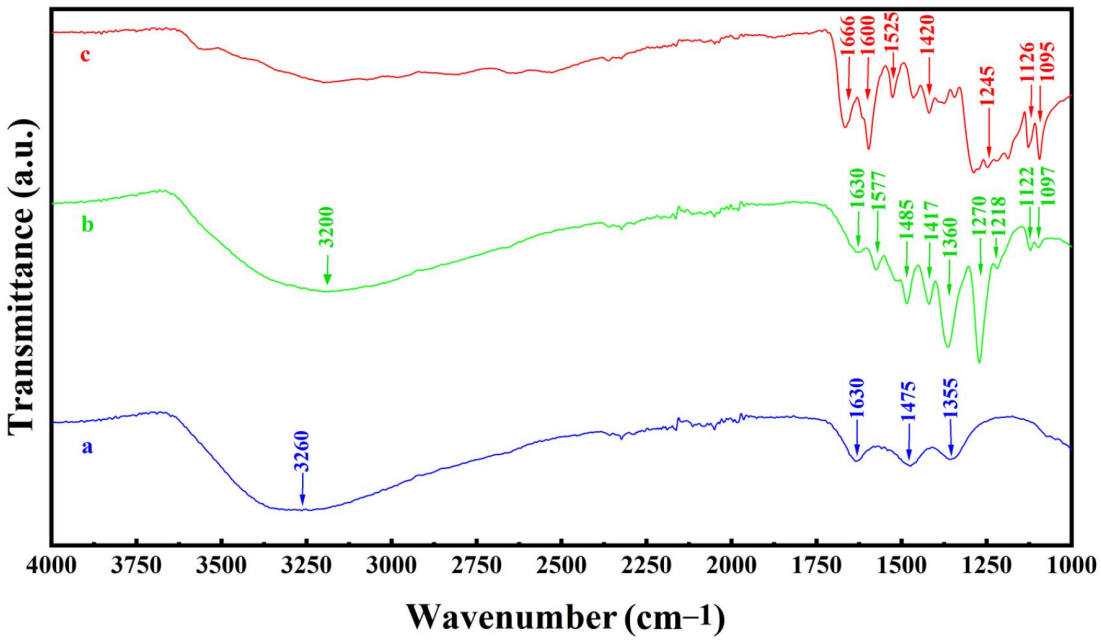

FIGURE 5.3: FTIR spectra of (a) Fe_3O_4 prepared without DHBA, (b) Fe_3O_4 prepared using DHBA, and (c) pure as-received DHBA.

The FTIR spectrum of Fe_3O_4 prepared without DHBA (Figure3a) showed absorptions at 1355, 1475, and 1630 cm^{-1}, which can be attributed [13, 62] to stretching of surface OH groups and vibrations of adsorbed CO_2. The broad absorption centred at 3260 cm^{-1} resulted from the O-H bending vibrations of adsorbed water [62]. Similar absorptions were observed in the spectrum of Fe_3O_4 prepared using DHBA (Figure3b). However, the spectrum of Fe_3O_4 prepared using DHBA showed additional absorptions due to adsorbed DHBA. The absorptions at 1097 and 1122 cm^{-1} resulted from bending C−H vibrations [63, 64]. Similar absorptions were observed in the spectrum of DHBA (Figure3c). The C−O stretching and bending vibrations [7, 64] of DHBA resulted in a broad absorption (Figure 3c) centred around 1245 cm^{-1} and corresponding absorptions at 1218 and 1270 cm^{-1} for Fe_3O_4 prepared using DHBA (Figure3b), which were not observed in the spectrum of Fe 3O4 prepared without DHBA (Figure3a). FTIR studies also revealed additional peaks related to the C−C vibrations in the range of 1300-1600 cm^{-1}

in the spectrum of Fe_3O_4 prepared using DHBA (Figure 3b), which were not observed in the spectrum of Fe_3O_4 prepared without DHBA (Figure3a). Such peaks, related to C−C stretching of aromatic rings, were observed in the spectrum of pure DHBA (Figure3c). Electrokinetic measurements showed that the adsorption of anionic DHBA resulted in increasing absolute value of negative zeta potential from −28.9 mV for Fe_3O_4 prepared without DHBA to −38.7 mV for Fe_3O_4 prepared using DHBA. Therefore, the results of sedimentation tests, zeta potential measurements, and FTIR spectroscopy indicated that DHBA adsorbed on Fe_3O_4 and facilitated the formation of suspensions with improved colloidal stability. In this investigation, MWCNT were used as a conductive additive for the fabrication of composite Fe_3O_4-MWCNT electrodes with enhanced electronic conductivity. Figure4 presents experimental results for the CV analysis of the Fe_3O_4-MWCNT composite electrodes. Electrodes were fabricated with synthesized Fe_3O_4 and MWCNT in the presence of DHBA, BA, and no dispersing agent to investigate the impact of a dispersant on capacitive behaviour. Electrodes prepared using DHBA showed significant improvement in capacitance at scan rates 2-50 mV s^{-1}. The role of the phenolic OH groups of DHBA is evident when comparing CVs and obtained capacitances of electrodes fabricated with DHBA and BA as dispersants. The capacitance of 4.59 F cm^{-2} for DHBA at 2 mV s^{-1} scan rate represents significant improvement, compared to the 2.38 F cm^{-2} and 2.80 F cm^{-2} obtained when using no dispersing agent and BA dispersant, respectively. The slightly lower capacitance of electrodes prepared using DHBA at a high scan rate of 100 mV s^{-1} can be attributed to the insulating properties of adsorbed DHBA, which affect the capacitance at such high scan rate.

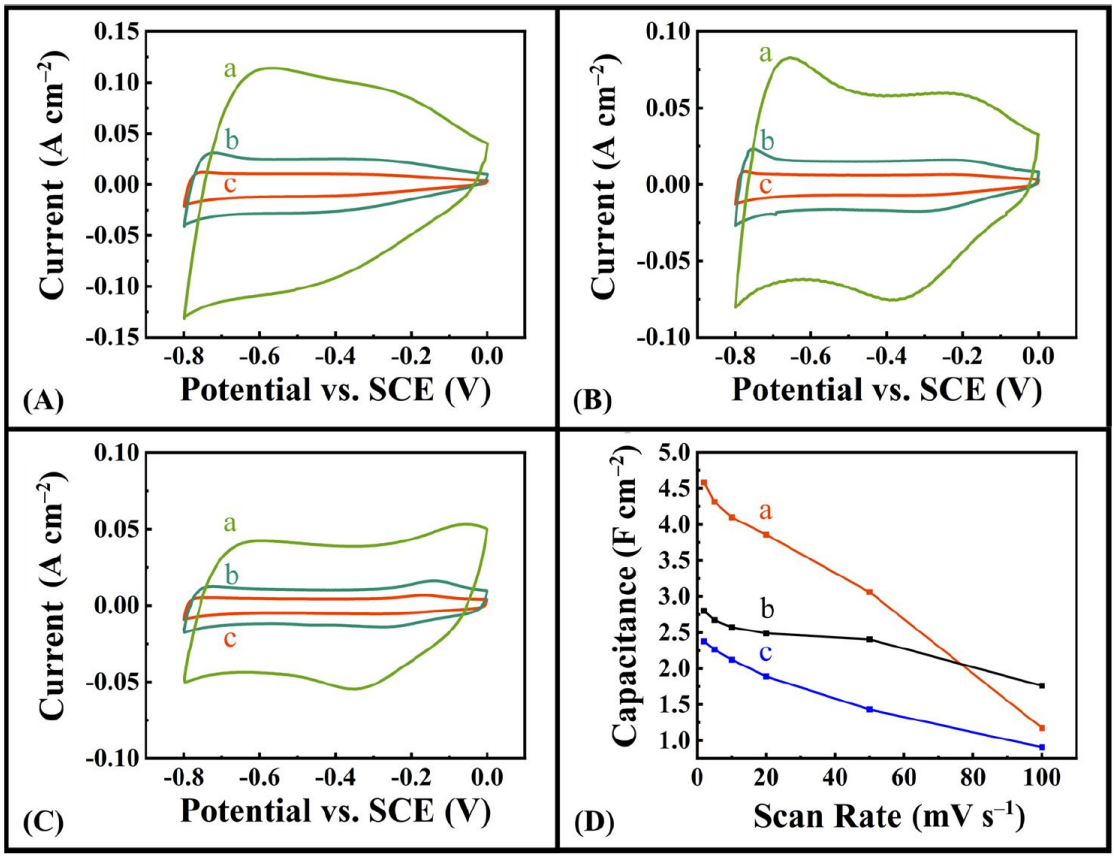

FIGURE 5.4: (A-C) CVs at scan rates of (a) 20, (b) 5, and (c) 2 mV s^{-1} for Fe_3O_4-MWCNT electrodes prepared with (A) DHBA as dispersing agent, (B) BA as dispersing agent, and (C) no dispersing agent. (D) Capacitance vs. scan rate for Fe_3O_4-MWCNT electrodes prepared with (a) DHBA as dispersing agent, (b) BA as dispersing agent, and (c) no dispersing agent.

Figure 5 compares the galvanostatic charge-discharge curves (A-C) for different electrodes, with corresponding capacitances (D) calculated from the discharge data at different current densities. GCD was performed in a voltage window of −0.8 - 0 V vs. SCE. Nearly symmetrical and triangular charge-discharge curves are seen, confirming the pseudocapacitive behaviour. Electrodes prepared with DHBA showed significant increase in discharge time and significant improvement in capacitance when compared to

electrodes prepared using BA or no dispersant. A capacitance of 4.72 F cm^{-2} was obtained for electrodes made with DHBA at a current density of 3 mA cm^{-2} and decreased to 3.16 F cm^{-2} with increasing current density. This capacitance shows significant improvement compared to the capacitances of 2.76 F cm^{-2} and 2.37 F cm^{-2} obtained for the electrodes prepared with BA as a dispersing agent and no dispersing agent, respectively, at the current density of 3 mA cm^{-2}. It should be noted that capacitance decreases with increasing charge-discharge time. The difference in the capacitance values obtained using CV and GCD data can result from the different time scale ranges used in both experiments. The Coulombic efficiency at 3 mA cm^{-2} was 98.0%; it decreased with current density to the value of 97.7% at a current density of 40 mA cm^{-2}. The electrodes prepared using DHBA showed significantly higher capacitance, compared to electrodes prepared with BA and without dispersant in the current density range of 3-40 mA cm^{-2}. The high areal capacitance obtained in this investigation for negative electrodes is important for the development of asymmetric devices operating in Na2SO4 electrolyte [56, 55]. The obtained capacitance is higher than the capacitance of carbon electrodes of the same mass operating in the negative potential range [54]. It is comparable with capacitance of advanced positive electrodes [56, 55]. It should be noted that catechol exhibits redox active properties in a positive potential range [25, 65]. Specifically, the redox activity is associated with the transition of phenolic groups of DHBA to a quinone-like structure [66, 67]. In this investigation, a catecholate type DHBA dispersant was used for the fabrication of negative electrodes. Therefore, redox reaction contribution of this dispersant to the to the electrode capacitance in the negative potential range is not expected. However, adsorbed catecholate molecules can facilitate charge transfer [21, 35, 36].

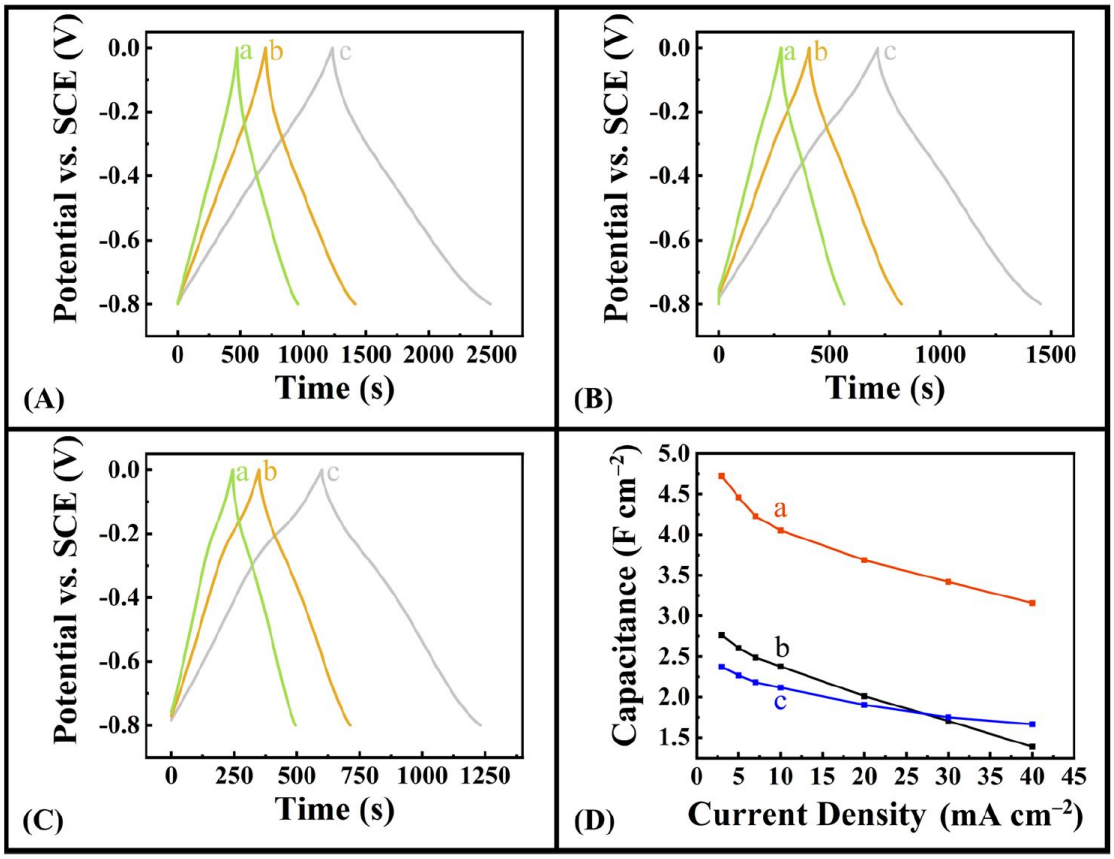

FIGURE 5.5: (A-C) charge-discharge curves at current densities of (a) 7 mA cm^{-2}, (b) 5 mA cm^{-2}, and (c) 3 mA cm^{-2} for Fe_3O_4-MWCNT electrodes prepared with (A) DHBA as dispersing agent, (B) BA as dispersing agent, and (C) no dispersing agent. (D) Capacitance vs. current density profiles for Fe_3O_4-MWCNT electrodes prepared with (a) DHBA as dispersing agent, (b) BA as dispersing agent, and (c) no dispersing agent.

The analysis of impedance data provides evidence of improved performance of the electrode fabricated using DHBA as a dispersing agent. Figure6A shows significant increase in the low frequency capacitance (C_s') for the electrode fabricated with DHBA as a dispersing agent compared to the electrodes where BA and no dispersing agent was used. The analysis of frequency dependences of C_s" shows an increase in the relaxation frequency for both electrodes prepared using DHBA and BA compared to the electrode

prepared with no dispersing agent (Figure6B). The Nyquist plot, presented in Figure6C, shows relatively low real part of impedance (Z'), indicating low resistance. Furthermore, the large slope shown in the Z" vs. Z' curves indicate good capacitive behaviour. Modelling of impedance spectroscopy data using equivalent circuits is an important strategy for the analysis of supercapacitor electrodes [68]. In this investigation, an equivalent circuit developed for high active mass bulk electrodes [69] was used. The simulation results presented in Figure6D showed good agreement with experimental data and indicated that the electrodes exhibited low charge transfer resistance (R_T), which was found to be 0.08 Ohm.

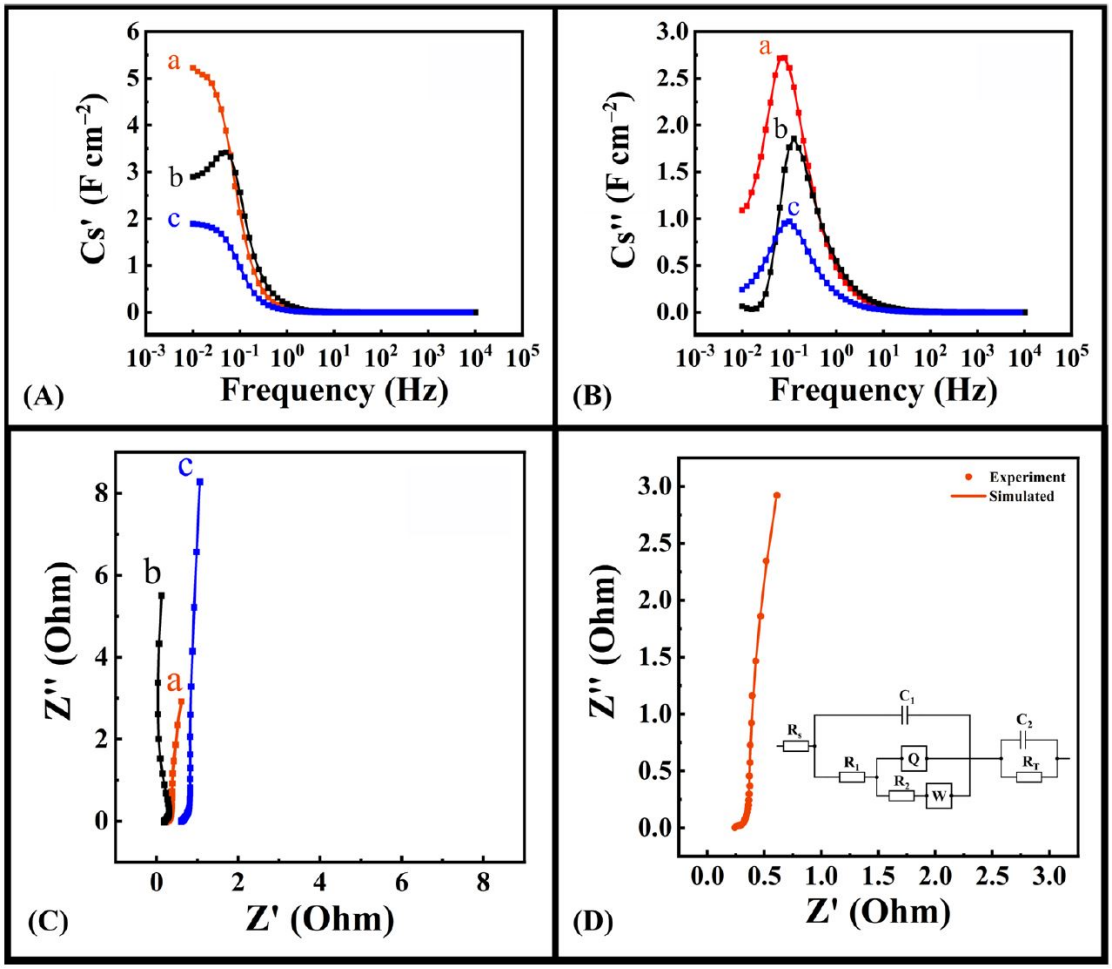

FIGURE 5.6: (A) Real part of capacitance (C_s') vs. frequency, (B) imaginary part of capacitance (C_s") vs. frequency, and (C) Nyquist plot for Fe_3O_4-MWCNT electrodes prepared with (a) DHBA as dispersing agent, (b) BA as dispersing agent, and (c) no dispersing agent, and (D) modelling of impedance for Fe_3O_4 electrode prepared using DHBA and corresponding equivalent circuit (inset).

Fe_3O_4 is a promising negative electrode material for the development of asymmetric supercapacitors [52] with enlarged voltage window for operation in mild electrolytes, such as K_2SO_4 or Na_2SO_4. However, the lower specific capacitance of the negative electrodes [52], compared to the capacitance of positive electrodes, limits the development of such devices. Another difficulty is related to significant decrease in specific capacitance with

TABLE 5.1: Comparison of lattice parameter, O−Fe bond lengths, magnetic moments to previous DFT study of bulk Fe_3O_4 and experimentally reported values.

Parameter	**Literature PBE+U** [71]	**This Work PBE+U+D3**	**Experimental**
Lattice parameter (Å)	8.488	8.453	8.396 [71]
Bond length (oct) (Å)	2.09	2.07	2.07 [72]
Bond length (tet) (Å)	1.90	1.91	1.88 [72]
Magnetic moment (Fe_{oct}) (μ_B)	3.96	3.92	-
Magnetic moment (Fe_{tet}) (μ_B)	4.09	4.02	-
Magnetic moment (O) (μ_B)	0.030	0.045	-
Total magnetic moment (μ_B/f.u)	4.0	4.0	4.1 [71]

increasing active mass [70]. However, high active mass loading is necessary for practical applications. The approach developed in this investigation allowed for improved utilization of capacitive properties of Fe_3O_4. Despite the high active mass of 40 mg cm^{-2}, the capacitance of 114.8 F g^{-1} (4.59 F cm^{-2}) was obtained from the CV data, which is higher than the reported capacitance [52] of 75 F g^{-1} at active mass of 8.8 mg cm^{-2}.

5.3.2 DFT Modeling of Adsorption on Fe_3O_4 001 Surface

Next, we performed DFT modelling of adsorption of molecules studied experimentally at the surface of Fe_3O_4. For this purpose, we established the most stable surface of Fe_3O_4 and its reconstruction. Relaxation of a bulk cubic Fe_3O_4 unit cell was conducted. The corresponding lattice parameter, bond lengths, and magnetic moments were in good agreement with values obtained in a prior DFT+U Fe_3O_4 study [71] and the experimental values found in literature. Table 1 summarizes these results, where differences between the two DFT studies may be attributed to the selection of a slightly different value for U_{eff}, as well as the Van der Waals interaction, accounted for in our work but not in the prior study [71].

For the purposes of this study, adsorption investigations were performed exclusively on the (001) surface of the Fe_3O_4 crystal. The abundance of the (001) surface on Fe_3O_4

nanoparticles has been confirmed experimentally [73]. The Fe_3O_4 nanoparticle surface was modelled as a slab of ($\sqrt{2}$ x $\sqrt{2}$)R45° supercell of bulk cubic magnetite. The exact structure of (001) surface of magnetite is a delicate topic [74, 75], sensitive to the chemical potential of species involved. We selected a stochiometric surface terminated with tetrahedrally coordinated Fe atoms (Fe_{tet}), which is in line with previous computational studies [76, 77, 78] that identified this (001) surface and its termination as the most energetically favourable.

Slabs of varying thicknesses (9, 15, and 23 layers) separated from its periodic image by a 25 Åvacuum layer were constructed to test for convergence of the surface energy (Figure 7). The resulting slabs were constrained by fixing the positions of the middle three layers of atoms at their relaxed bulk positions (the region enclosed by dashed lines in (Figure 7) to simulate the bulk phase of Fe_3O_4, while the remaining outer layers of atoms were allowed to relax during optimization to simulate the surface reconstruction. The surface energy was calculated as

$$\gamma = \frac{E_{slab} - NE_{bulk}}{2A}, \tag{5.1}$$

where E_{slab} is the total energy of the constructed surface slab, N is the equivalent number of Fe_3O_4 formula units in the slab, E_{bulk} is the total energy per formula unit of the bulk Fe_3O_4, and A is the area of the surface slab. The calculated surface energies were compared to the surface energy found in a prior DFT study of Fe_3O_4 (001) surface [78]. These results can be seen in Table 2, where surface energy and Fe−O bond length are compared.

The bond length converges quickly as a function of the number of layers, while the surface energy converges very slowly. Due to computational constraints, we selected the 9-layer surface to investigate the physicochemical nature of the catechol adhesion.

TABLE 5.2: Fe_3O_4 (001) surface energy and Fe-O bond length of surface tetrahedrally coordinated Fe, for 23-layer, 15-layer, and 9-layer slabs calculated at PBE+U+D3 level of theory and compared to previous surface study using PBE+U.

Surfaces (PBE+U+D3)	**Surface Energy (J m^{-2})**	**Surface Fe−O Bond Length (Å)**
23 layers	0.48	1.92
15 layers	0.73	1.81
9 layers	0.90	1.90
Literature, 9 layers (PBE+U)	0.96 [76]	1.89 [77]

Figure 7 shows the final 9-layer force relaxed surface of which DHBA and BA adsorption will be modelled using DFT. One can see that the tetrahedrally coordinated Fe atoms on the top and bottom of the surface (shown by arrows) moved towards the bulk during relaxation, which is in agreement with literature [76].

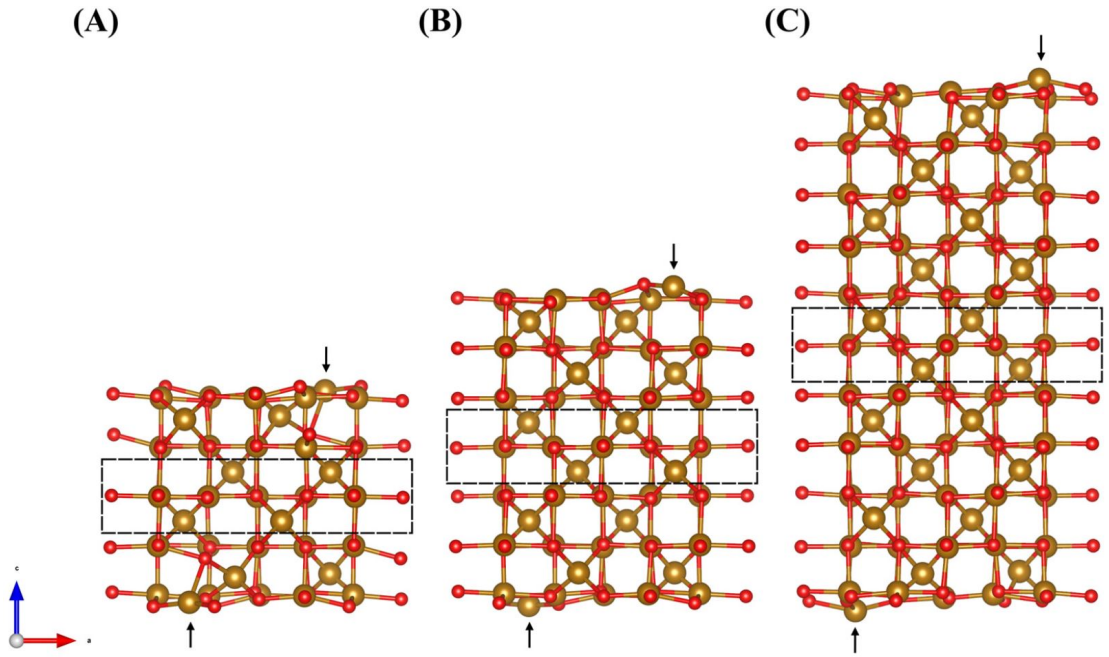

FIGURE 5.7: The 9-layer (A), 15-layer (B), and 23-layer (C) relaxed surfaces with Hubbard U correction. Dashed rectangle indicates region where atoms within are constrained to their relaxed bulk positions. The arrows point at Fe_tet atoms in the first surface termination layer.

5.3.2.1 DFT Analysis of DHBA and BA Adsorption at the (001) Surface

Previous adsorption studies [78, 79, 80] of single adatoms and water molecules on the surface of Fe_3O_4 have found favourable adsorption sites and have reported adsorption energies for the various species. Ni adatoms were found to adsorb favourably onto the (001) surface and reported an adsorption enthalpy of -3.21 eV [78]. This study also reported the incorporation of Ni and Ti into the subsurface by replacing Fe tetrahedral and octahedral sites, respectively. Incorporation energies of -3.39 eV for the Ni and -8.29 eV for the Ti were reported [78]. Gargallo-Caballero et al. [75] reported co-adatom adsorption as well as incorporation at octahedral/tetrahedral sites with energies of the order of -5.5 eV for the magnetite (001) surface. Additionally, adsorption enthalpies of

-0.76 eV for H_2O molecules adsorbing to surface Fe_{tet} atoms and -0.85 eV for singleH atoms adsorbing to surface O atoms were reported [79, 80]. For adsorption of DHBA onto the Fe_3O_4 surface, bonding to both tetrahedrally and octahedrally coordinated Fe atoms were considered, in a manner that maintained coordination seen in the bulk crystal.

Adsorption of DHBA is modelled on the (001) surface in four different configurations, seen in Figure8. Two H atoms are cleaved from phenolic OH groups, in the case of Figure8A,B,D, and are accommodated on surface O atoms. In the cases where the carboxyl group is responsible for adsorption (Figures8C and9A), only oneH atom is cleaved and accommodated by Fe_3O_4 forming a surface OH group. Adsorption strength of molecules to the surface of Fe_3O_4 is evaluated by the calculation of an adsorption enthalpy (H_{ads}), which represents the difference between the total energy (E_{tot}) of the adsorbed and nonadsorbed states

$$H_{ads} = E_{tot}^{adsorbed} - E_{tot}^{nonadsorbed}. \tag{5.2}$$

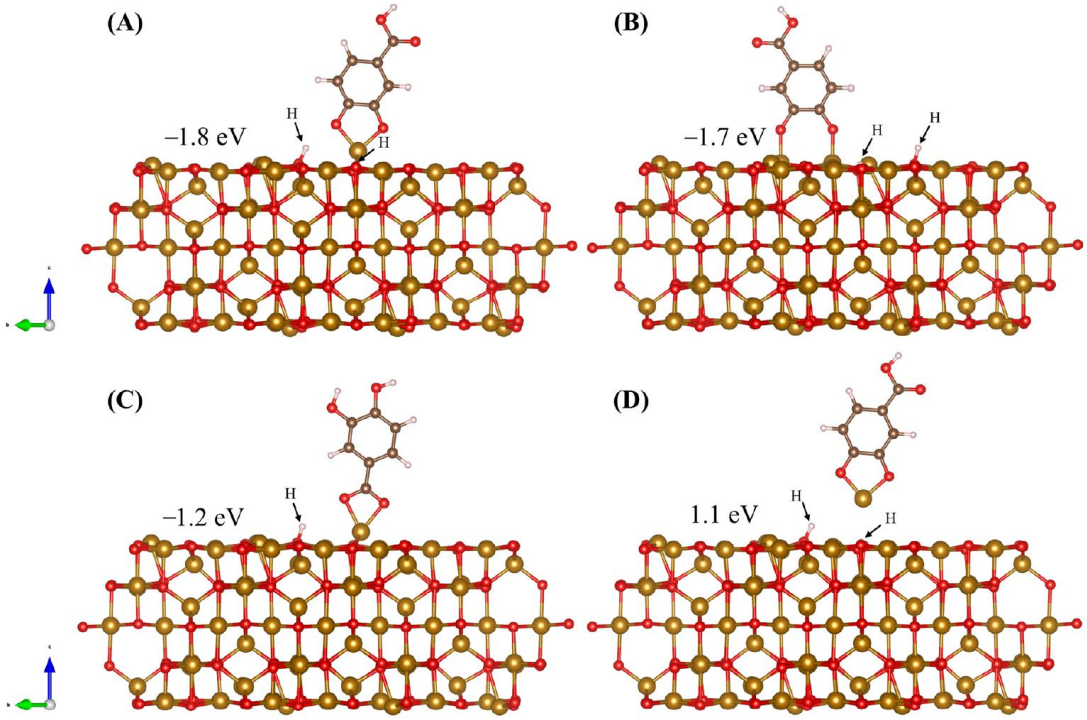

FIGURE 5.8: Adsorption of DHBA on the (001) surface of Fe_3O_4 in three different configurations, (A) chelating bidentate via phenolic OH groups, (B) bridging bidentate via phenolic OH groups, (C) chelating bidentate via carboxyl group, and (D) scenario where molecule adsorbs and detaches with Fe atom. The adsorption is accompanied by the surface adsorption of H^+ ions displaced from OH groups. Values on each panel represent respective adsorption energies.

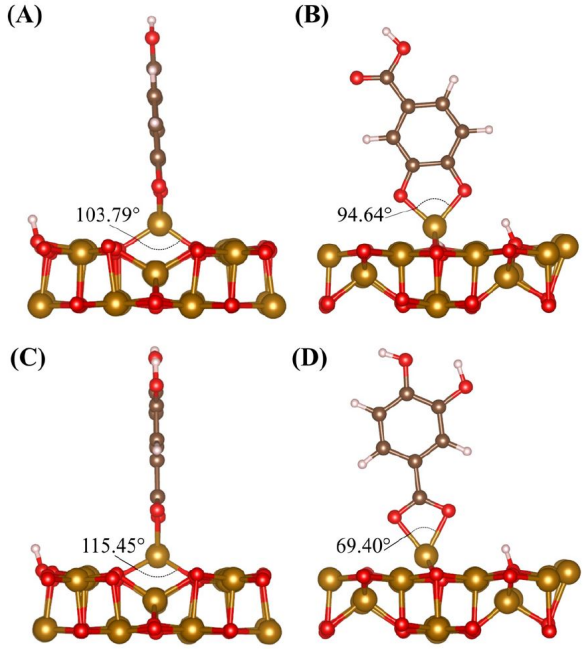

FIGURE 5.9: Surface Fe bond angles for (A) bottom of DHBA via phenolic OH group adsorption, (B) top of DHBA via phenolic OH group adsorption, (C) bottom of DHBA via carboxyl group adsorption, (D) top of DHBA via carboxyl group adsorption. Values of bond angles in degrees are shown on each panel.

The nonadsorbed state is modelled as the surface slab with the respective molecule in a fixed, nonadsorbed state 10 Åabove the surface in the vacuum layer. The calculated adsorption enthalpies are shown within Figure 8. The DFT study reveals that the three adsorbed configurations are energetically favourable, while the Fe_{tet}-detached configuration (Figure 8D) is not. Figure 8A,C,D include adsorption of DHBA to a surface Fe_{tet} atom where Figure 8B captures adsorption of DHBA to two surface octahedrally coordinated Fe atoms (Fe_{oct}). The chelating bidentate configuration is the most energetically favourable, closely followed by the bridging bidentate; the carboxyl bidentate configuration is the least favourable. These trends can be explained by examining the resulting bond angles. In the case of the chelating bidentate adsorption of DHBA via phenolic OH groups (Figure 8A), the Fe_{tet} atom is pulled away from the surface. This

causes the bond angle between the surface Fe_{tet} atom and the surface O atom to change from 157.26° to 103.79°, seen in Figure 9A, returning the bond angle to a value much closer to what occurs in the bulk crystal (109.47°). This configuration also forms a bond angle with O atoms in the DHBA molecule of 94.64° (Figure 9B).

In the case where DHBA is adsorbed via carboxyl group, we again see the bond angles changing, this time to 115.45° between the surface O and Fe_{tet} and 69.40° between the O atoms in the carboxyl group and Fe_{tet}, shown in Figure 9C,D, respectively. This less drastic change in the bond angle towards what is seen in the bulk crystal may contribute to the less favourable adsorption energy seen when adsorption occurs via the carboxyl group. Another consideration is that less energy may be required during the cleaving/adsorption process of theH atom in one of the phenolic OH groups (Figure 8A) compared to breaking the double bonded O in the carboxyl group (Figure 8C) to bond to the Fe_{tet} atom. We see similar changes in bond angle for adsorption via carboxyl group for BA to that of adsorption via carboxyl group for DHBA, this time changing to 114.33° in the case of Figure 9C and to 65.12° in the case of Figure 9D. This further explains the results seen experimentally, describing the role of phenolic OH groups for adsorption onto the Fe_3O_4 surface. In all configurations, the DHBA adsorption restores the coordination of the metal ions involved in bonding.

Two different configurations of BA on the surface of Fe_3O_4 can be seen in Figure 10. In the chelating bidentate configuration (Figure 10A) adsorption energy is similar to that of the chelating bidentate adsorption via carboxyl group seen with DHBA (Figure 8C). In both cases where the carboxyl group is responsible for adsorption, the adsorption energy is much less than that of the chelating bidentate adsorption via phenolic OH groups. Figure 10B shows the optimized position of BA when it is positioned above the surface so that theH atoms point toward the surface. We can see that in this case adsorption is very weak. To explain the clear difference seen in the experimental results,

where dispersion and capacitive properties are greatly improved with the use of DHBA, and the use of BA compares similarly to no dispersing agent at all; it is the electrostatic repulsion that must differ and not adsorption. For DHBA, adsorption utilizing the two adjacent OH groups results in the most energetically favourable adsorption configuration. Then, the carboxyl group is available to facilitate the electrostatic repulsion needed for good dispersion. However, in the case of BA, where the carboxyl functional group is involved in adsorption to the surface, there are no functional groups to provide the charge essential for electrostatic repulsion.

During the modelling of adsorption of both DHBA and BA, the presence of a solvent was neglected. Since the synthesis of Fe_3O_4 was conducted in a water medium, we would expect adsorption energies to reduce by approximately a factor of two [81] without changing trends. Thus, the presence of a solvent in our calculations would not affect the main conclusions, since we are interested in the trend of adsorption energy across different configurations and molecules, and not in the magnitude of adsorption energy seen.

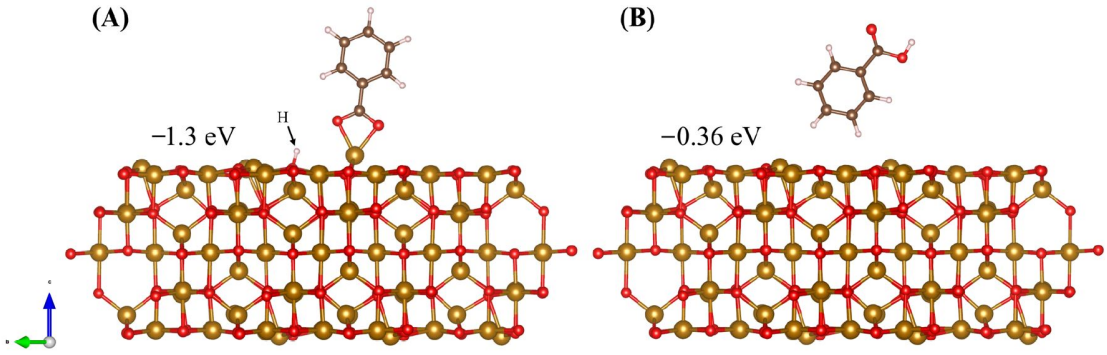

FIGURE 5.10: Adsorption of BA in two different configurations, (A) chelating bidentate via carboxyl groups, and (B) bonding of H to Fe_3O_4 surface O atoms. The adsorption can be accompanied by the surface adsorption of H+ ions displaced from OH groups.

5.4 Materials and Methods

5.4.1 Materials and Experimental Methods

Iron (II) chloride tetrahydrate, iron (III) chloride hexahydrate, ammonium hydroxide, 3,4-dihydroxybenzoic acid, benzoic acid, poly (vinyl butyral-co-vinyl alcohol-co-vinyl acetate) (PVB, MilliporeSigma, Canada), multiwalled carbon nanotubes (MWCNT, ID 4 nm, OD 13 nm, length 1-2 µm, Bayer, Leverkusen, Germany), and nickel foam (porosity 95%, thickness 1.6 mm, Vale, Toronto, ON, Canada), were used as starting materials. Synthesis of Fe_3O_4 was performed by a chemical precipitation method [41, 53] using aqueous solutions of iron (II) chloride and iron (III) chloride. The molar ratio of $FeCl_2$ to $FeCl_3$ in the solutions was 1:2. A similar procedure was carried with DHBA to analyse the influence of DHBA on the electrode performance, as well as with BA to gain insight into the dispersion and adsorption mechanisms involved. For the synthesis of Fe_3O_4 in the presence of MWCNT, a 3 g L^{-1} MWCNT suspension, containing 1.5 g L^{-1} DHBA or BA, was initially prepared. Preparation included ultrasonication of the MWCNT suspensions using a high energy Cole-Parmer (VCX 500, Cole-Parmer, Quebec City, QC, Canada) ultrasonic processor. Iron (II) chloride tetrahydrate and iron (III) chloride hexahydrate were added to the suspension, allowing for an Fe_3O_4:MWCNT mass ratio of 4:1. The pH of the solutions was adjusted to pH = 9 by ammonium hydroxide. Chemical precipitation was performed at 50°C at continuous stirring. Obtained suspensions were filtrated, washed to remove non-adsorbed dispersant and reaction by-products, and dried overnight in an oven at 60°C. Electrodes were prepared by impregnation of Ni foam current collectors with slurries, containing Fe_3O_4, MWCNT and PVB binder. The mass ratio of Fe_3O_4:MWCNT:PVB was 80:20:3. The mass of the impregnated material after drying was 40 mg cm^{-2}. The impregnated Ni foams were pressed to 30% of their original thickness in order to improve electrical contact of the impregnated material and current collector. A Bruker Vertex 70 spectrometer (Bruker, Milton, ON, Canada) was used

for the Fourier Transform Infrared Spectroscopy (FTIR) experiments. Zeta potential measurements were performed using a dynamic light scattering instrument (DelsaMax Pro: Beck- man Coulter, Brea, CA, USA). Electrochemical studies were performed in aqueous 0.5 M Na_2SO_4 electrolyte using PARSTAT 2273 potentiostat (AMETEK, Berwyn, PA, USA) for cyclic voltammetry (CV) and electrochemical impedance spectroscopy (EIS). Galvanostatic charge-discharge (GCD) investigations were performed using Biologic VMP 300 poten- tiostat (BioLogic, Seyssinet-Pariset, France). Testing was performed using a 3-electrode electrochemical cell containing a working (impregnated Ni foam), counter-electrode (Pt mesh, MiliporeSigma, Oakville, ON, Canada), and a reference electrode(SCE, saturated calomel electrode, AMETEK, Berwyn, PA, USA). Mass and area normalized capacitances were calculated from the corresponding CV and GCD data, as described by previous studies [70, 82]. The capacitances calculated from the CV and GCD data represented integral capacitances measured in a potential window of 0.8-0 V versus SCE. The capacitances calculated from the EIS data represented differential capacitances measured at an open circuit potential at voltage amplitude of 5 mV. CV results were obtained at 2, 5, 10, 20, 50, and 100 mV s^{-1} scan rates with EIS measurements performed afterwards. GCD results were obtained at 3, 5, 7, 10, 20, 30, and 40 mA cm^{-2} current densities.

5.4.2 Computational

The first-principles electronic structure calculations were performed in the framework of DFT [57] using Perdew–Burke–Ernzerhof (PBE) generalized gradient approximation [83] for the exchange correlation functional, augmented by the DFT-D3 correction with Becke– Johnson damping [84, 85] to capture van der Waals interactions. The Vienna ab initio simulation program (VASP) (version 5.4.4, University of Vienna, Vienna, Austria) [86, 87, 88] and projector augmented-wave potentials [89] were used, where the p semi-core states were treated as valence states for Fe potentials in all calculations. Standard

potentials were used for all other elements. The cut-off energy for a plane wave expansion of 500 eV was used for the relaxation of the bulk and surface structures to achieve an accurate stress tensor, and the cut-off energy of 400 eV was used in the case of adsorption calculations. During bulk relaxation, atomic position, cell shape, and cell volume were relaxed, whereas only atomic positions were relaxed during the surface and adsorption calculations. We included on-site Coulomb interaction to treat the highly correlated Fe 3d-electrons in the framework of Dudarev et al. [90] using an effective Hubbard energy of U = 3.7 eV [78]. Collinear spin-polarized calculations were performed for all structures. Magnetic moments were initialized with opposing spin orientations of magnitude 4.0 μB for tetrahedrally and octahedrally coordinated Fe atoms [91]. Full self-consistent structural optimization was performed for the bulk, while only forces were relaxed for surface models of Fe_3O_4 with additional constrains (see Section 5.3.2 for more details). The structure was considered as optimized when the magnitude of Hellmann–Feynman forces acting on atoms dropped below 50 meV $Å^{-1}$ and components of the stress tensor did not exceed 1 kbar. The ground- state energy was calculated using first order Methfessel–Paxton smearing with a width of 0.02 eV. A blocked-Davidson algorithm with high precision is used during the relaxation of the bulk and surface Fe_3O_4 structures. The Brillouin zone was sampled with a Γ-centered k-mesh generated automatically with a linear density of 15 divisions per 1 $Å^{-1}$ of the reciprocal space. Adsorption calculations utilize a preconditioned conjugate gradient with normal precision and automatic Γ-centered k-mesh with 30 divisions per 1 $Å^{-1}$. Construction of the Fe_3O_4 (001) surfaces is discussed in the results and discussions section. All structure files and VASP input files used in this work can be found in the Supporting Information section. Structure files can be visualized in VESTA [92].

5.5 Conclusions

We have investigated the role DHBA has on the electrochemical performance of composite Fe_3O_4-MWCNT anode material for use in supercapacitors. DHBA's exceptional adsorption and dispersing properties, utilized during synthesis of Fe_3O_4, contribute to the significant increase in capacitance at low values of impedance. With a mass loading of 40 mg cm^{-2}, a capacitance of 4.59 F cm^{-2} was obtained from CV data at a scan rate of 2 mV s^{-1} and 4.72 F cm^{-2} from GCD data at a current density of 3 mA cm^{-2}. DFT surface and adsorption study of DHBA and BA on the Fe_3O_4 (001) surface sheds light on the adsorption and dispersion mechanisms seen experimentally. The largest magnitudes of adsorption enthalpies, 1.8 and 1.7 eV, are seen for DHBA chelating bidentate and DHBA bridging bidentate configurations, respectively. Lower adsorption enthalpies were calculated for adsorption of DHBA and BA via bidentate bonding of the carboxyl group, where we see comparable adsorption enthalpies of 1.2 and 1.3 eV, respectively. One can therefore conclude that, due to favourable and comparable adsorption enthalpies of DHBA and BA utilizing a carboxyl functional group, the difference in dispersion and electrochemical performance seen when comparing these two molecules as dispersing agents is dependent on the means of electrostatic repulsion. We see that the more favourable adsorption configurations for DHBA are those that rely on the phenolic OH groups for adsorption, allowing the carboxyl group to facilitate electrostatic repulsion. The Fe_3O_4-MWCNT anode obtained with the use of DHBA as a dispersing agent, showing improved electrochemical properties, is favourable in the development of advanced energy storage devices.

Supplementary Materials: The following supporting information can be downloaded at: https:// www.mdpi.com/article/10.3390/molecules28041562/s1. This paper is accompanied by a ZIP archive file that contains VASP files (POSCAR) for all structures calculated in the present work. In addition, structure-specific input files (INCAR)

as well as KPOINTS files are provided. POSCAR files can be visualized using VESTA [94].

Author Contributions: Conceptualization, C.B., O.R. and I.Z.; methodology, O.R. and I.Z.; software, C.B. and O.R.; validation, C.B., O.R. and I.Z.; formal analysis, C.B., O.R. and I.Z.; investigation, C.B.; resources, O.R. and I.Z.; data curation, C.B.; writing—original draft preparation, C.B., O.R. and I.Z.; writing—review and editing, C.B., O.R. and I.Z.; visualization, C.B.; supervision, O.R. and I.Z; project administration, O.R. and I.Z; funding acquisition, O.R. and I.Z. All authors have read and agreed to the published version of the manuscript.

Funding: This research was funded by the Natural Sciences and Engineering Research Council of Canada and Faculty of Engineering of McMaster University. Calculations were performed using the Compute Canada infrastructure supported by the Canada Foundation for Innovation under John R. Evans Leaders Fund.

Institutional Review Board Statement: Not applicable.

Informed Consent Statement: Not applicable.

Data Availability Statement: The data is available in this manuscript and Supplementary information.

Acknowledgments: O.R. is thankful to Peter Blaha (TU Vienna) for insightful discussions on the model of magnetite (001) surface.

Conflicts of Interest: The authors declare no conflict of interest.

Sample Availability: Samples of Fe_3O_4 are available from the authors.

Bibliography

[1] T. Zhang, P. Wojtal, O. Rubel, and I. Zhitomirsky, "Density functional theory and experimental studies of caffeic acid adsorption on zinc oxide and titanium dioxide nanoparticles," *RSC Adv.*, vol. 5, no. 129, pp. 106877–106885, 2015.

[2] J. Melrose, "High performance marine and terrestrial bioadhesives and the biomedical applications they have inspired," *Molecules*, vol. 27, p. 8982, Dec. 2022.

[3] P. Forouzandeh, V. Kumaravel, and S. C. Pillai, "Electrode materials for supercapacitors: A review of recent advances," *Catalysts*, vol. 10, p. 969, Aug. 2020.

[4] K. Hennig and W. Meyer, "Synthesis and characterization of catechol-containing polyacrylamides with adhesive properties," *Molecules*, vol. 27, p. 4027, June 2022.

[5] M. S. Ata, Y. Liu, and I. Zhitomirsky, "A review of new methods of surface chemical modification, dispersion and electrophoretic deposition of metal oxide particles," *RSC Adv.*, vol. 4, no. 43, p. 22716, 2014.

[6] B. K. Ahn, "Perspectives on mussel-inspired wet adhesion," *J. Am. Chem. Soc.*, vol. 139, pp. 10166–10171, Aug. 2017.

[7] I. A. Janković, Z. V. Šaponjić, M. I. Čomor, and J. M. Nedeljković, "Surface modification of colloidal TiO_2 nanoparticles with bidentate benzene derivatives," *J. Phys. Chem. C Nanomater. Interfaces*, vol. 113, pp. 12645–12652, July 2009.

[8] J. P. Cornard and C. Lapouge, "Theoretical and spectroscopic investigations of a complex of Al(III) with caffeic acid," *J. Phys. Chem. A*, vol. 108, pp. 4470–4478, May 2004.

[9] E. Faure, C. Falentin-Daudré, C. Jérôme, J. Lyskawa, D. Fournier, P. Woisel, and C. Detrembleur, "Catechols as versatile platforms in polymer chemistry," *Prog. Polym. Sci.*, vol. 38, pp. 236–270, Jan. 2013.

[10] A. Clifford, X. Pang, and I. Zhitomirsky, "Biomimetically modified chitosan for electrophoretic deposition of composites," *Colloids Surf. A Physicochem. Eng. Asp.*, vol. 544, pp. 28–34, May 2018.

[11] A. Clifford, B. E. J. Lee, K. Grandfield, and I. Zhitomirsky, "Biomimetic modification of poly-l-lysine and electrodeposition of nanocomposite coatings for orthopaedic applications," *Colloids Surf. B Biointerfaces*, vol. 176, pp. 115–121, Apr. 2019.

[12] R. Sikkema, K. Baker, and I. Zhitomirsky, "Electrophoretic deposition of polymers and proteins for biomedical applications," *Adv. Colloid Interface Sci.*, vol. 284, p. 102272, Oct. 2020.

[13] K. Wu, Y. Wang, and I. Zhitomirsky, "Electrophoretic deposition of TiO2 and composite TiO2-MnO2 films using benzoic acid and phenolic molecules as charging additives," *J. Colloid Interface Sci.*, vol. 352, pp. 371–378, Dec. 2010.

[14] Q. Zhao and I. Zhitomirsky, "Biomimetic strategy for electrophoretic deposition of composite ferroelectric poly(vinylidene, fluoride-co-hexafluoropropylene) – ferrimagnetic NiFe2O4 films," *Colloids Surf. A Physicochem. Eng. Asp.*, vol. 651, p. 129743, Oct. 2022.

[15] R. M. E. Silva, R. Poon, J. Milne, A. Syed, and I. Zhitomirsky, "New developments in liquid-liquid extraction, surface modification and agglomerate-free processing of inorganic particles," *Adv. Colloid Interface Sci.*, vol. 261, pp. 15–27, Nov. 2018.

[16] J. Milne, R. Marques Silva, and I. Zhitomirsky, "Surface modification and dispersion of ceramic particles using liquid-liquid extraction method for application in supercapacitor electrodes," *J. Eur. Ceram. Soc.*, vol. 39, pp. 3450–3455, Sept. 2019.

[17] D. J. Mowbray and A. Migani, "Optical absorption spectra and excitons of dye-substrate interfaces: Catechol on TiO2(110)," *J. Chem. Theory Comput.*, vol. 12, pp. 2843–2852, June 2016.

[18] S. Sakib, R. Pandey, L. Soleymani, and I. Zhitomirsky, "Surface modification of TiO 2 for photoelectrochemical DNA biosensors," *Med. Devices Sens.*, vol. 3, Apr. 2020.

[19] R. Savin, C. Blanck, N.-O. Benzaamia, and F. Boulmedais, "Optimization of nanohybrid biosensors based on electro-crosslinked tannic acid capped nanoparticles/enzyme," *Molecules*, vol. 27, p. 3309, May 2022.

[20] A. L. Pinto, L. Cruz, V. Gomes, H. Cruz, G. Calogero, V. de Freitas, F. Pina, A. J. Parola, and J. Carlos Lima, "Catechol versus carboxyl linkage impact on DSSC performance of synthetic pyranoflavylium salts," *Dyes Pigm.*, vol. 170, p. 107577, Nov. 2019.

[21] K. Yan, Y. Liu, Y. Guan, N. Bhokisham, C.-Y. Tsao, E. Kim, X.-W. Shi, Q. Wang, W. E. Bentley, and G. F. Payne, "Catechol-chitosan redox capacitor for added amplification in electrochemical immunoanalysis," *Colloids Surf. B Biointerfaces*, vol. 169, pp. 470–477, Sept. 2018.

[22] S. Wu, E. Kim, J. Li, W. E. Bentley, X.-W. Shi, and G. F. Payne, "Catechol-based capacitor for redox-linked bioelectronics," *ACS Appl. Electron. Mater.*, vol. 1, pp. 1337–1347, Aug. 2019.

[23] J. J. N. Segoviano-Garfias, G. A. Zanor, F. Ávila-Ramos, and E. Y. Bivián-Castro, "Equilibrium studies of iron (III) complexes with either pyrazine, quinoxaline, or phenazine and their catecholase activity in methanol," *Molecules*, vol. 27, p. 3257, May 2022.

[24] E. Touzé, F. Gohier, B. Daffos, P.-L. Taberna, and C. Cougnon, "Improvement of electrochemical performances of catechol-based supercapacitor electrodes by tuning the redox potential via different-sized o-protected catechol diazonium salts," *Electrochim. Acta*, vol. 265, pp. 121–130, Mar. 2018.

[25] E. Jokar, S. Shahrokhian, and A. I. Zad, "Electrochemical functionalization of graphene nanosheets with catechol derivatives as an effective method for preparation of highly performance supercapacitors," *Electrochim. Acta*, vol. 147, pp. 136–142, Nov. 2014.

[26] D. Malka, S. Giladi, O. Hanna, M. Weitman, R. Cohen, Y. Elias, R. Attias, T. Brousse, A. A. Frimer, and D. Aurbach, "Catechol-modified carbon cloth as hybrid electrode for energy storage devices," *J. Electrochem. Soc.*, vol. 166, no. 6, pp. A1147–A1153, 2019.

[27] R. Pourghobadi, D. Nematollahi, M. R. Baezzat, S. Alizadeh, and H. Goljani, "Electropolymerization of catechol on wireless graphite electrode. unusual cathodic polycatechol formation," *J. Electroanal. Chem. (Lausanne Switz)*, vol. 866, p. 114180, June 2020.

[28] H. Beiginejad, D. Nematollahi, M. Bayat, F. Varmaghani, and A. Nazaripour, "Experimental and theoretical analysis of the electrochemical oxidation of catechol and hydroquinone derivatives in the presence of various nucleophiles," *J. Electrochem. Soc.*, vol. 160, no. 10, pp. H693–H698, 2013.

[29] N. Sadaba, M. Salsamendi, N. Casado, E. Zuza, J. Muñoz, J.-R. Sarasua, D. Mecerreyes, D. Mantione, C. Detrembleur, and H. Sardon, "Catechol end-functionalized polylactide by organocatalyzed ring-opening polymerization," *Polymers (Basel)*, vol. 10, p. 155, Feb. 2018.

[30] A. S. Barham, B. M. Kennedy, V. J. Cunnane, and M. A. Daous, "The electrochemical polymerisation of 1,2 dihydroxybenzene and 2-hydroxybenzyl alcohol prepared in different solutions media," *Electrochim. Acta*, vol. 147, pp. 19–24, Nov. 2014.

[31] J. Su, F. Chen, V. L. Cryns, and P. B. Messersmith, "Catechol polymers for ph-responsive, targeted drug delivery to cancer cells," *J. Am. Chem. Soc.*, vol. 133, pp. 11850–11853, Aug. 2011.

[32] S. Razaviamri, K. Wang, B. Liu, and B. P. Lee, "Catechol-based antimicrobial polymers," *Molecules*, vol. 26, p. 559, Jan. 2021.

[33] J. Kim, C. Lee, and J. H. Ryu, "Adhesive catechol-conjugated hyaluronic acid for biomedical applications: A mini review," *Appl. Sci. (Basel)*, vol. 11, p. 21, Dec. 2020.

[34] M. Nawwar, R. P. Sahu, I. K. Puri, and I. Zhitomirsky, "Pseudocapacitive behavior of ferrimagnetic NiFe2O4-carbon nanotube electrodes prepared with a multifunctional dispersing agent," *Open Ceramics*, vol. 6, p. 100127, June 2021.

[35] D. E. Tallman, C. Vang, G. G. Wallace, and G. P. Bierwagen, "Direct electrodeposition of polypyrrole on aluminum and aluminum alloy by electron transfer mediation," *J. Electrochem. Soc.*, vol. 149, no. 3, p. C173, 2002.

[36] C. Shi and I. Zhitomirsky, "Electrodeposition of composite polypyrrole–carbon nanotube films," *Surf. Eng.*, vol. 27, pp. 655–661, Oct. 2011.

[37] C. Shi and I. Zhitomirsky, "Electrodeposition and capacitive behavior of films for electrodes of electrochemical supercapacitors," *Nanoscale Res. Lett.*, vol. 5, pp. 518–523, Jan. 2010.

[38] D. K. Nagesha, B. D. Plouffe, M. Phan, L. H. Lewis, S. Sridhar, and S. K. Murthy, "Functionalization-induced improvement in magnetic properties of Fe3O4 nanoparticles for biomedical applications," *J. Appl. Phys.*, vol. 105, p. 07B317, Apr. 2009.

[39] W. Huang, P. Jiang, C. Wei, D. Zhuang, and J. Shi, "Low-temperature one-step synthesis of covalently chelated ZnO/dopamine hybrid nanoparticles and their optical properties," *J. Mater. Res.*, vol. 23, pp. 1946–1952, July 2008.

[40] M. Bloemen, D. Debruyne, P.-J. Demeyer, K. Clays, A. Gils, N. Geukens, C. Bartic, and T. Verbiest, "Catechols as ligands for CdSe–ZnS quantum dots," *RSC Adv.*, vol. 4, no. 20, p. 10208, 2014.

[41] M. Nawwar, R. Poon, R. P. Sahu, I. K. Puri, and I. Zhitomirsky, "Fe3O4 spinel-Mn3O4 spinel supercapacitor prepared using celestine blue as a dispersant, capping agent and charge transfer mediator," *Ceram. Int.*, vol. 46, pp. 18851–18858, Aug. 2020.

[42] T. Togashi, S. Takami, K. Kawakami, H. Yamamoto, T. Naka, K. Sato, K. Abe, and T. Adschiri, "Continuous hydrothermal synthesis of 3,4-dihydroxyhydrocinnamic acid-modified magnetite nanoparticles with stealth-functionality against immunological response," *J. Mater. Chem.*, vol. 22, no. 18, p. 9041, 2012.

[43] T. Sugimoto, H. Itoh, and T. Mochida, "Shape control of monodisperse hematite particles by organic additives in the gel-sol system," *J. Colloid Interface Sci.*, vol. 205, pp. 42–52, Sept. 1998.

[44] M. Hori, C. Pagnoux, J.-F. Baumard, and M. Nogami, "Preparation of gold nanoparticles (GNP) aqueous suspensions by a new method involving tiron," *J. Mater. Sci.*, vol. 42, pp. 80–86, Jan. 2007.

[45] X. Huang, Y. Pang, Y. Liu, Y. Zhou, Z. Wang, and Q. Hu, "Green synthesis of silver nanoparticles with high antimicrobial activity and low cytotoxicity using catechol-conjugated chitosan," *RSC Adv.*, vol. 6, no. 69, pp. 64357–64363, 2016.

[46] L. Zhang, D. Wu, and X. Yan, "Applications of magnetic field for electrochemical energy storage," *Appl. Phys. Rev.*, vol. 9, p. 031307, Sept. 2022.

[47] Y. N. Venevtsev, V. V. Gagulin, and I. D. Zhitomirsky, "Material science aspects of seignette-magnetism problem," *Ferroelectrics*, vol. 73, pp. 221–248, June 1987.

[48] M. B. Poudel and H. J. Kim, "Confinement of Zn-Mg-Al-layered double hydroxide and α-Fe2O3 nanorods on hollow porous carbon nanofibers: A free-standing electrode for solid-state symmetric supercapacitors," *Chem. Eng. J.*, vol. 429, p. 132345, Feb. 2022.

[49] K. Malaie and M. R. Ganjali, "Spinel nano-ferrites for aqueous supercapacitors; linking abundant resources and low-cost processes for sustainable energy storage," *J. Energy Storage*, vol. 33, p. 102097, Jan. 2021.

[50] S. Ghasemi and F. Ahmadi, "Effect of surfactant on the electrochemical performance of graphene/iron oxide electrode for supercapacitor," *J. Power Sources*, vol. 289, pp. 129–137, Sept. 2015.

[51] X. Li, L. Zhang, and G. He, "Fe3O4 doped double-shelled hollow carbon spheres with hierarchical pore network for durable high-performance supercapacitor," *Carbon N. Y.*, vol. 99, pp. 514–522, Apr. 2016.

[52] T. Brousse and D. Bélanger, "A hybrid fe_3o_4-mno_2 capacitor in mild aqueous electrolyte," *Electrochem. Solid State Letters*, vol. 6, no. 11, p. A244, 2003.

[53] M. Nawwar, R. Poon, R. Chen, R. P. Sahu, I. K. Puri, and I. Zhitomirsky, "High areal capacitance of fe_3o_4-decorated carbon nanotubes for supercapacitor electrodes," *Carbon Energy*, vol. 1, pp. 124–133, Sept. 2019.

[54] R. Chen, M. Yu, R. P. Sahu, I. K. Puri, and I. Zhitomirsky, "The development of pseudocapacitor electrodes and devices with high active mass loading," *Adv. Energy Mater.*, vol. 10, p. 1903848, May 2020.

[55] K. Wickramaarachchi and M. Minakshi, "Status on electrodeposited manganese dioxide and biowaste carbon for hybrid capacitors: The case of high-quality oxide composites, mechanisms, and prospects," *J. Energy Storage*, vol. 56, p. 106099, Dec. 2022.

[56] K. Wickramaarachchi and M. Minakshi, "Consequences of electrodeposition parameters on the microstructure and electrochemical behavior of electrolytic manganese dioxide (EMD) for supercapacitor," *Ceram. Int.*, vol. 48, pp. 19913–19924, July 2022.

[57] W. Kohn and L. J. Sham, "Self-consistent equations including exchange and correlation effects," *Phys. Rev.*, vol. 140, pp. A1133–A1138, Nov. 1965.

[58] L. Wang, H. Ji, S. Wang, L. Kong, X. Jiang, and G. Yang, "Preparation of Fe3O4 with high specific surface area and improved capacitance as a supercapacitor," *Nanoscale*, vol. 5, pp. 3793–3799, May 2013.

[59] N. Saikia, J. Sarma, J. M. Borah, and S. Mahiuddin, "Adsorption of 3,4-dihydroxybenzoic acid onto hematite surface in aqueous medium: importance of position of phenolic -OH groups and understanding of the same using catechol as an auxiliary model," *J. Colloid Interface Sci.*, vol. 398, pp. 227–233, May 2013.

[60] J. M. Borah, J. Sarma, and S. Mahiuddin, "Adsorption comparison at the α-alumina/water interface: 3,4-dihydroxybenzoic acid vs. catechol," *Colloids Surf. A Physicochem. Eng. Asp.*, vol. 387, pp. 50–56, Aug. 2011.

[61] G. A. Parks, "The isoelectric points of solid oxides, solid hydroxides, and aqueous hydroxo complex systems," *Chem. Rev.*, vol. 65, pp. 177–198, Apr. 1965.

[62] T. . Kamakshi, G. . Sunita Sundari, H. Erothu, and R. . Subhakaran Singh, "EFFECT OF NICKEL DOPANT ON STRUCTURAL, MORPHOLOGICAL AND OPTICAL CHARACTERISTICS OF Fe3O4 NANOPARTICLES," *Rasayan J. Chem.*, vol. 12, no. 02, pp. 531–536, 2019.

[63] K. D. Dobson and A. J. McQuillan, "In situ infrared spectroscopic analysis of the adsorption of aromatic carboxylic acids to TiO2, ZrO2, Al2O3, and Ta2O5 from

aqueous solutions," *Spectrochim. Acta A Mol. Biomol. Spectrosc.*, vol. 56, pp. 557–565, Feb. 2000.

[64] H. Gulley-Stahl, P. A. Hogan, 2nd, W. L. Schmidt, S. J. Wall, A. Buhrlage, and H. A. Bullen, "Surface complexation of catechol to metal oxides: an ATR-FTIR, adsorption, and dissolution study," *Environ. Sci. Technol.*, vol. 44, pp. 4116–4121, June 2010.

[65] J. Choi, M. Yang, and S.-K. Kim, "Pseudocapacitive organic catechol derivative-functionalized three-dimensional graphene aerogel hybrid electrodes for high-performance supercapacitors," *Appl. Surf. Sci.*, vol. 422, pp. 316–320, Nov. 2017.

[66] S. M. Golabi and D. Nematollahi, "Electrochemical study of 3,4-dihydroxybenzoic acid and 4- tert -butylcatechol in the presence of 4-hydroxycoumarin application to the electro-organic synthesis of coumestan derivatives," *J. Electroanal. Chem. (Lausanne Switz)*, vol. 430, pp. 141–146, June 1997.

[67] C. Litos, V. Aletras, D. Hatzipanayioti, M. Kamariotaki, and A. Lymberopoulou-Karaliota, "CV and NMR study on the reaction of Mo(VI) with 3,4-dihydroxybenzoic acid and ascorbic acid in aqueous solution," *Inorganica Chim. Acta*, vol. 360, pp. 2321–2330, May 2007.

[68] M. B. Poudel, A. R. Kim, S. Ramakrishan, N. Logeshwaran, S. K. Ramasamy, H. J. Kim, and D. J. Yoo, "Integrating the essence of metal organic framework-derived ZnCoTe–N–C/MoS2 cathode and ZnCo-NPS-N-CNT as anode for high-energy density hybrid supercapacitors," *Compos. B Eng.*, vol. 247, p. 110339, Dec. 2022.

[69] Y. Wang, Y. Liu, and I. Zhitomirsky, "Surface modification of MnO2 and carbon nanotubes using organic dyes for nanotechnology of electrochemical supercapacitors," *J. Mater. Chem. A Mater. Energy Sustain.*, vol. 1, no. 40, p. 12519, 2013.

[70] K. Shi and I. Zhitomirsky, "Electrophoretic nanotechnology of graphene-carbon nanotube and graphene-polypyrrole nanofiber composites for electrochemical supercapacitors," *J. Colloid Interface Sci.*, vol. 407, pp. 474–481, Oct. 2013.

[71] J. Noh, O. I. Osman, S. G. Aziz, P. Winget, and J.-L. Brédas, "A density functional theory investigation of the electronic structure and spin moments of magnetite," *Sci. Technol. Adv. Mater.*, vol. 15, p. 044202, Aug. 2014.

[72] A. Jain, S. P. Ong, G. Hautier, W. Chen, W. D. Richards, S. Dacek, S. Cholia, D. Gunter, D. Skinner, G. Ceder, and K. A. Persson, "Commentary: The materials project: A materials genome approach to accelerating materials innovation," *APL Mater.*, vol. 1, p. 011002, July 2013.

[73] L. Zhao, H. Zhang, Y. Xing, S. Song, S. Yu, W. Shi, X. Guo, J. Yang, Y. Lei, and F. Cao, "Morphology-controlled synthesis of magnetites with nanoporous structures and excellent magnetic properties," *Chem. Mater.*, vol. 20, pp. 198–204, Jan. 2008.

[74] R. Bliem, E. McDermott, P. Ferstl, M. Setvin, O. Gamba, J. Pavelec, M. A. Schneider, M. Schmid, U. Diebold, P. Blaha, L. Hammer, and G. S. Parkinson, "Subsurface cation vacancy stabilization of the magnetite (001) surface," *Science*, vol. 346, pp. 1215–1218, Dec. 2014.

[75] R. Gargallo-Caballero, L. Martín-García, A. Quesada, C. Granados-Miralles, M. Foerster, L. Aballe, R. Bliem, G. S. Parkinson, P. Blaha, J. F. Marco, and J. de la Figuera, "Co on Fe3O4(001): Towards precise control of surface properties," *J. Chem. Phys.*, vol. 144, p. 094704, Mar. 2016.

[76] D. Santos-Carballal, A. Roldan, R. Grau-Crespo, and N. H. de Leeuw, "A DFT study of the structures, stabilities and redox behaviour of the major surfaces of magnetite Fe_3O_4," *Phys. Chem. Chem. Phys.*, vol. 16, pp. 21082–21097, Oct. 2014.

[77] T. Yang, X.-D. Wen, J. Ren, Y.-W. Li, J.-G. Wang, and C.-F. Huo, "Surface structures of Fe3O4 (111), (110), and (001): A density functional theory study," *J. Fuel Chem. Technol.*, vol. 38, pp. 121–128, Feb. 2010.

[78] R. Bliem, J. Pavelec, O. Gamba, E. McDermott, Z. Wang, S. Gerhold, M. Wagner, J. Osiecki, K. Schulte, M. Schmid, P. Blaha, U. Diebold, and G. S. Parkinson, "Adsorption and incorporation of transition metals at the magnetiteFe3O4(001) surface," *Phys. Rev. B Condens. Matter Mater. Phys.*, vol. 92, Aug. 2015.

[79] N. Mulakaluri, R. Pentcheva, and M. Scheffler, "Coverage-dependent adsorption mode of water on Fe_3O_4(001): Insights from first principles calculations," *J. Phys. Chem. C Nanomater. Interfaces*, vol. 114, pp. 11148–11156, July 2010.

[80] N. Mulakaluri and R. Pentcheva, "Hydrogen adsorption and site-selective reduction of the Fe3O4(001) surface: Insights from first principles," *J. Phys. Chem. C Nanomater. Interfaces*, vol. 116, pp. 16447–16453, Aug. 2012.

[81] M. Albert, A. Clifford, I. Zhitomirsky, and O. Rubel, "Adsorption of maleic acid monomer on the surface of hydroxyapatite and TiO2: A pathway toward biomaterial composites," *ACS Appl. Mater. Interfaces*, vol. 10, pp. 24382–24391, July 2018.

[82] D. Yan, Y. Li, Y. Liu, R. Zhuo, Z. Wu, B. Geng, J. Wang, P. Ren, P. Yan, and Z. Geng, "Hydrothermal synthesis and electrochemical properties of hexagonal hydrohausmannite plates as supercapacitor electrode material," *Mater. Lett.*, vol. 117, pp. 62–65, Feb. 2014.

[83] J. P. Perdew, K. Burke, and M. Ernzerhof, "Generalized gradient approximation made simple," *Phys. Rev. Lett.*, vol. 77, pp. 3865–3868, Oct. 1996.

[84] S. Grimme, J. Antony, S. Ehrlich, and H. Krieg, "A consistent and accurate ab initio parametrization of density functional dispersion correction (DFT-D) for the 94 elements H-Pu," *J. Chem. Phys.*, vol. 132, p. 154104, Apr. 2010.

[85] S. Grimme, S. Ehrlich, and L. Goerigk, "Effect of the damping function in dispersion corrected density functional theory," *J. Comput. Chem.*, vol. 32, pp. 1456–1465, May 2011.

[86] G. Kresse and J. Hafner, "Ab initio molecular dynamics for liquid metals," *Phys. Rev. B Condens. Matter*, vol. 47, pp. 558–561, Jan. 1993.

[87] G. Kresse and J. Furthmüller, "Efficiency of ab-initio total energy calculations for metals and semiconductors using a plane-wave basis set," *Comput. Mater. Sci.*, vol. 6, pp. 15–50, July 1996.

[88] G. Kresse and J. Furthmüller, "Efficient iterative schemes for ab initio total-energy calculations using a plane-wave basis set," *Phys. Rev. B Condens. Matter*, vol. 54, pp. 11169–11186, Oct. 1996.

[89] G. Kresse and D. Joubert, "From ultrasoft pseudopotentials to the projector augmented-wave method," *Phys. Rev. B Condens. Matter*, vol. 59, pp. 1758–1775, Jan. 1999.

[90] S. L. Dudarev, G. A. Botton, S. Y. Savrasov, C. J. Humphreys, and A. P. Sutton, "Electron-energy-loss spectra and the structural stability of nickel oxide: An LSDA+U study," *Phys. Rev. B Condens. Matter*, vol. 57, pp. 1505–1509, Jan. 1998.

[91] F. Chiter, V. B. Nguyen, N. Tarrat, M. Benoit, H. Tang, and C. Lacaze-Dufaure, "Effect of van der waals corrections on DFT-computed metallic surface properties," *Materials Research Express*, vol. 3, p. 046501, Apr. 2016.

[92] K. Momma and F. Izumi, "Vestafor three-dimensional visualization of crystal, volumetric and morphology data," *Journal of Applied Crystallography*, vol. 44, pp. 1272–1276, Oct. 2011.

Chapter 6

Application of murexide as a capping agent for fabrication of magnetite anodes for supercapacitors: experimental and first-principle studies

Coulton Boucher

Igor Zhitomirsky

Oleg Rubel

Submitted to The Journal of Physical Chemistry C on July 28, 2023

Archived at arXiv.org, 2023;

https://doi.org/10.48550/arXiv.2307.15845

6.1 Abstract

In this study, we investigate the effectiveness of murexide for surface modification of Fe_3O_4 nanoparticles to enhance the performance of multi-walled carbon nanotube-Fe_3O_4 supercapacitor anodes. Our experimental results demonstrate significant improvements in electrode performance when murexide is used as a capping or dispersing agent compared to the case with no additives. When murexide is used as a capping agent, we report a capacitance of 4.2 F cm^{-2} from cyclic voltammetry analysis with good capacitance retention at high scan rate. From impedance measurements, we reveal a substantial decrease in the real part of impedance for samples prepared with murexide, indicating easier charge transfer at more negative electrode potentials, and reinforcing the role of murexide as a capping agent and charge transfer mediator. Density functional theory is used to investigate interactions between the murexide adsorbate and the Fe_3O_4 (001) surface, with a specific emphasis on adsorption strength, charge transfer, and electronic properties. This theoretical investigation uncovers a strong adsorption enthalpy of -4.5 eV, and allows us to identify the nature of chemical bonds between murexide and the surface, with significant charge transfer taking place between the Fe_3O_4 surface and murexide adsorbate. The transfer of electrons from the Fe_3O_4 surface to murexide is recognized as a vital component of the adsorption process. By examining the bonding nature of murexide on Fe_3O_4, this research study uncovers insights and proposes a novel bonding configuration of murexide that incorporates a combination of bridging and chelating bonding.

6.2 Introduction

Supercapacitors have emerged as promising energy storage devices due to their high power density, fast charging and discharging rates, and long cycle life [1]. Advanced

electrode materials play a critical role in the electrochemical performance of supercapacitors, as they are responsible for storing and releasing charge during the charge/discharge cycles [2]. However, the electrochemical performance of these materials can be limited by factors such as low surface area, poor wettability, and high resistance at the electrode-electrolyte interface.

Surface modification has been identified as a key strategy to overcome these limitations and enhance the electrochemical performance of anode materials for supercapacitor applications [3, 4]. Surface modification techniques such as surface roughening, the use of nanostructured materials, and the control of surface chemistry can increase the surface area, improve the wettability, and reduce the resistance at the electrode-electrolyte interface [5, 6, 7]. These modifications can lead to higher capacitance and energy density, improved rate capability, and cycling stability of supercapacitors.

By utilizing distinct materials for the anode and cathode, a supercapacitor device can optimize its operational voltage window by capitalizing on the unique potential ranges offered by each electrode [8]. Such an asymmetric device, containing Fe_3O_4 and MnO_2 electrodes, can exhibit an expanded voltage window of 1.8 V in aqueous K_2SO_4 electrolyte and have a reported capacitance of 50 F g^{-1} at electrode mass density of 8.8 mg cm^{-2} [9]. However, the negative electrodes display a significantly lower gravimetric capacitance than the positive electrodes, leading to a greater active mass in the negative electrode needed to match the capacitance of the positive electrode. This emphasizes the need to increase the specific capacitance of the negative electrodes, while ensuring excellent performance at high active mass. Designing electrodes with high active mass poses several challenges, including the poor charge transfer between Fe_3O_4 and conductive additives. Metal oxide nanoparticles and carbon nanotubes (CNTs) have high surface areas, making them prone to agglomeration, which further complicates the charge transfer process. Additionally, a decline in specific capacitance is observed as the

active mass of capacitive material increases, primarily due to the weak electronic and ionic conductivities [10] of metal oxide-based electrodes.

Recently, significant interest has been generated in application of chelating molecules for surface modification of materials [11]. The strong adsorption of such molecules on particle surface is an important factor for many applications. Molecules of different types are currently under investigation, including catecholates, gallates, salicylates, and other molecules from phosphonic acid and chromotropic acid families [11, 3]. Such molecules show strong bidentate or tridentate bonding to metal atoms on the particle surface, which is critical for their applications as capping agents for synthesis of nanoparticles, dispersing agents for colloidal processing and extractors for liquid-liquid extraction of nanoparticles[11, 3, 12]. Surface modification of metals with various catecholates such as Tiron and alizarin red, and molecules of other types such as chromotropic acid, facilitated electron transfer, reduced electropolymerization potential, and enabled electropolymerization of polypyrrole on non-noble substrates [13, 14, 15, 16]. Of particular interest are applications of catecholates as photosensitizers for surface modification of semiconductors for photovoltaic applications [17]. Catecholates were used as capping agents for synthesis of nanoparticles for supercapacitor electrodes with enhanced capacitive properties [6]. To enhance the capacitance of supercapacitor electrodes, a catecholate-type celestine blue molecule was employed as a capping agent during synthesis, a cationic dispersing agent for colloidal processing, and a charge transfer mediator [18].

Charge transfer mediators introduce a fast and reversible redox reaction that enhances the ionic conductivity and increases the pseudocapacitive capacity of the supercapacitor [19]. They can also store charges through valence changes and electron transfer between the mediators and electronic conductors, such as activated carbon, which provides additional charge capacity beyond that of electrostatic double layer capacitors [20, 21]. Unlike pseudocapacitance, the redox mediator-induced capacitance is not dependent on

the number of electrochemically active sites. The energy density of a redox mediator-based supercapacitor relies on the solubility of the redox mediators and their interaction with the electrodes. If highly soluble redox mediators are used, the volumetric energy density can be significantly improved as the dissolved mediator molecules or ions do not cause any significant volume changes in the entire system [22]. [23] have shown that using hydroquinone as a redox mediator in an electrolyte supporting 1 M H_2SO_4 with a chemically activated carbon electrode can result in a two-fold increase in specific capacitance. This increase is due to the additional pseudocapacitive contribution from the faradaic reactions of the hydroquinone/quinone system in the redox electrolyte. These studies have generated interest in the search for charged chelating molecules with redox properties for the development of advanced supercapacitor electrodes.

Murexide is a versatile and widely used indicator in analytical chemistry. Murexide has been employed in complexometric investigations involving *3d* or *4f* ions, where the formation of a complex results in a modification of the solution's color [24, 25, 26, 27]. It can form stable, colored complexes with a range of metal ions, including transition metals such as iron, cobalt, nickel, and copper [28]. These complexes have distinctive hues that can be easily observed and quantified, making murexide an excellent tool for identifying and measuring metal ions in a sample. Furthermore, murexide can be employed in both aqueous and non-aqueous solvents, expanding its potential applications in a variety of fields [29].

Murexide has emerged as a promising capping and dispersing agent for the surface modification of cathode materials in supercapacitor applications [30, 12]. Murexide has been used as a capping agent for Mn_3O_4 nanoparticles and as a co-dispersant for Mn_3O_4 and CNTs. The adsorption of murexide on Mn_3O_4 and CNTs facilitated electrostatic co-dispersion of Mn_3O_4 with CNTs with enhanced mixing to significantly increase the performance of the Mn_3O_4-CNT electrodes [12].

The redox properties of murexide have been investigated in various solvents and electrolytes, and the results have shown that it can exhibit multiple redox peaks with high redox potentials and good reversibility in aqueous electrolytes, indicating its potential for high energy density applications. In aqueous electrolytes, reversible cathodic and anodic peaks are well defined in a voltage window of 0 to -1.5 V vs. saturated calomel electrode (SCE) [29].

In this work, we are conducting the first density functional theory (DFT) study to investigate the adsorption mechanism and binding energy of murexide on a surface of Fe_3O_4. The bonding mechanism of murexide on surfaces remains poorly understood, and therefore, we propose a novel bonding configuration that utilizes four atoms in the murexide molecule, forming a combination of bridging and chelating bonds. This proposed configuration contrasts with the tridentate [12, 28, 31] bonding previously suggested in the literature and offers a promising explanation for the strong adsorption observed experimentally. The charge density and Bader charge analyses are performed to understand the mechanism of molecular adsorption and magnitude of charge transfer during the adsorption process. The results of this study provide insights into the underlying principles governing the interaction between murexide and Fe_3O_4 and will help to identify the optimal conditions for using murexide as an effective adsorbent in various applications. To corroborate the theoretical findings with experimental results, we have fabricated Fe_3O_4-CNT composite electrodes using murexide as a capping and dispersing agent. This study aims to investigate, for the first time, the difference in electrode performance when the same molecule is used strictly as a dispersing agent, or as a capping agent. This combination of theoretical and experimental approaches provides a comprehensive understanding of the behavior of murexide as a dispersant agent, capping agent, and charge transfer mediator, and its potential use in energy storage applications.

6.3 Results and discussion

6.3.1 Experimental results

In this investigation murexide was investigated as both a dispersing and capping agent to facilitate the co-dispersion of Fe_3O_4 nanoparticles and CNTs to be used as the active material in supercapacitor anodes. Five techniques were conducted and tested where an electrode was fabricated from Fe_3O_4 and CNTs with no additives (NA), 5% murexide added as a dispersing agent to synthesized Fe_3O_4 particles and CNTs in a solution of ethanol and dispersed in ethanol via probe ultrasonication (DE), 5% murexide added as a dispersing agent to synthesized Fe_3O_4 particles and CNTs in a solution of water and dispersed water via probe ultrasonication (DW), 5% murexide as a capping agent added during synthesis of Fe_3O_4 (C5), and 10% murexide as a capping agent added during synthesis of Fe_3O_4 (C10).

The cyclic voltammetry (CV) curves in figure 6.1 clearly show that the addition of murexide provides an increase in electrode performance compared to the case where no additive is used. In the cases where murexide is used as strictly a dispersing agent (DE and DW) we can see a slight increase in the peak capacitance of the electrodes from 2.4 F cm^{-2} for NA to 2.6 F cm^{-2} and 3.0 F cm^{-2} for DE and DW, respectively, at a scan rate of 2 mV s^{-1}. We see capacitance retention at increasing scan rate improving greatly for DE and DW, where capacitance at 100 mV s^{-1} is 2.3 F cm^{-2} and 2.0 F cm^{-2}, respectively, compared to 0.9 F cm^{-2} for NA. For C5 and C10, peak capacitance increases much more significantly, reaching a peak capacitance of 4.5 F cm^{-2} and 4.2 F cm^{-2}, respectively, at 2 mV s^{-1} scan rate. The improved capacitance retention is not seen for C5 as capacitance fades to 1.9 F cm^{-2} at 100 mV s^{-1}. When the concentration of murexide used as a capping agent increases from 5% to 10%, we see capacitance retention similar to DE and DW, where capacitance at 100 mV s^{-1} is reported at 3.4 F cm^{-2}.

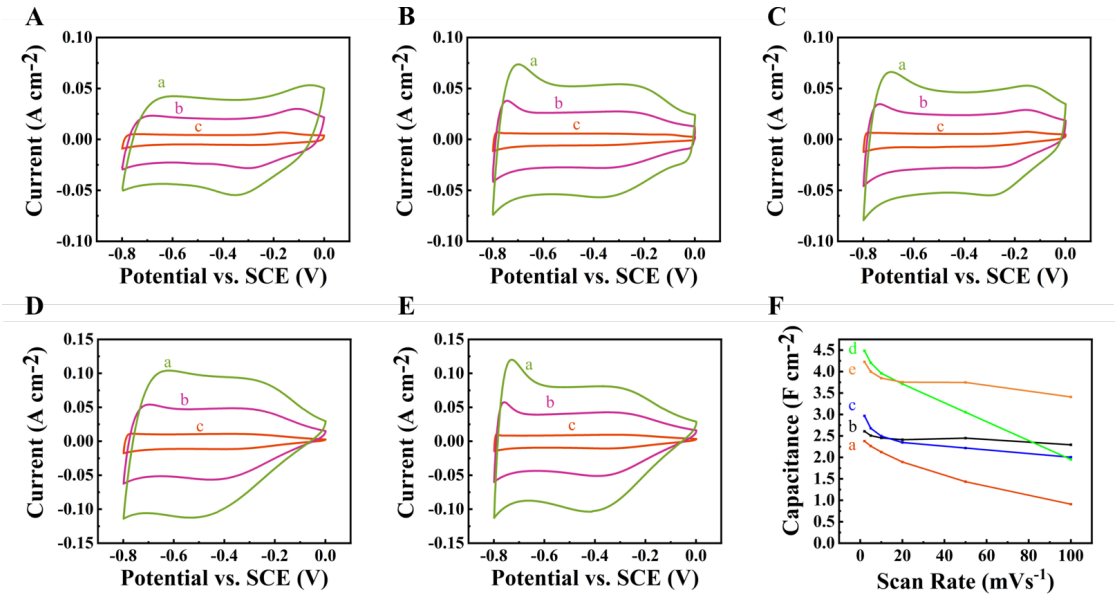

FIGURE 6.1: (A, B, C, D, E) CVs at scan rates of (a) 20, (b) 10, and (c) 2 mV s^{-1} for for (A) NA, (B) DE, (C) DW, (D) C5, and (E) C10. (F) Capacitance vs. scan rate for for (a) NA, (b) DE, (c) DW, (d) C5, and (e) C10.

We see a greater increase in the peak capacitance with murexide used as a capping agent compared to as a dispersing agent. We do, however, see better capacitance retention when murexide is used as a dispersing agent compared to a capping agent at a concentration of 5%.

When synthesis of Fe_3O_4 is conducted without additives, particles are able to agglomerate into larger particles after synthesis. Once murexide is introduced as a dispersing agent, these particles are no longer able to agglomerate further. This in combination with the adsorbed murexide playing the role of a charge transfer mediator results in a slight increase in peak capacitance and an improvement in the capacitance retention at higher scan rates.

It is known that increasing the scan rate can result in a decrease in the measured capacitance [32]. This is because the scan rate affects the amount of time that the

electrochemical reactions have to take place at the electrode-electrolyte interface [33, 34]. This results in the resistance at the electrode-electrolyte interface becoming a limiting factor in the charging and discharging processes at high scan rates [35, 33]. Murexide shows redox active peaks in the negative potential range, leading to a reversible 1 electron transfer process[29] and allowing murexide to serve as a charge transfer mediator in a negative potential window. This charge transfer mediation allows for a decrease in resistance at the electrode-electrolyte interface. This means that electrons can more easily transfer during the surface redox reactions necessary for charge storage, which at high scan rates, need to happen very quickly in order to retain capacitance.

As a capping agent during synthesis, murexide is able to form complexes with the actively forming Fe_3O_4 surfaces. This prevents agglomeration as well as controls the growth of the Fe_3O_4 particles during formation. This results in a suspension containing smaller particles, which allows for the fabrication of an electrode with a higher active surface area for the necessary surface redox reaction to take place during cycling.

When the concentration of murexide as a capping agent is increased from 5% to 10%, there is more murexide to facilitate charge transfer from electrolyte to the active electrode material, effectively decreasing resistance at the electrode-electrolyte interface due to the redox properties of murexide. The redox properties of murexide will contribute indirectly to the capacitance of the electrode. This is evident in the samples where murexide is used as a capping agent (figure 6.1 D and E) where we see an increase in the CV area specifically in the more negative potential range. The increase in CV area in only this range can be attributed to the influence of the adsorbed murexide molecule, which exhibits redox peaks in this range.

Figure 6.2 compares the galvanostatic charge-discharge (GCD) curves (panels A-E) for different electrodes, with corresponding capacitance (panel F) calculated from the discharge data at different current densities. GCD was performed in a potential window

of −0.8 V to 0 V vs SCE. Nearly symmetrical and triangular charge-discharge curves are seen, confirming the pseudocapacitive behavior. Similar to the trends we see with the CV data, when electrodes showed only a slight increase in capacitance when murexide is used as a dispersing agent. For murexide as a dispersing agent in ethanol and water we see a peak capacitance of 2.8 F cm^{-2} and 2.7 F cm^{-2}, respectively, at the current density of 3 mA cm^{-2} compared to a value of 2.4 F cm^{-2} for the case where no additive is used. When murexide is used as a capping agent, we again see a much more significant increase in the value of capacitance. For murexide as a capping agent with a concentration of 5% and 10% we see a peak capacitance of 4.6 F cm^{-2} and 4.1 F cm^{-2}, respectively, at the current density of 3 mA cm^{-2}. At current densities above 10 mA cm^{-2}, we see that the capacitance of C10 exceeds that of C5.

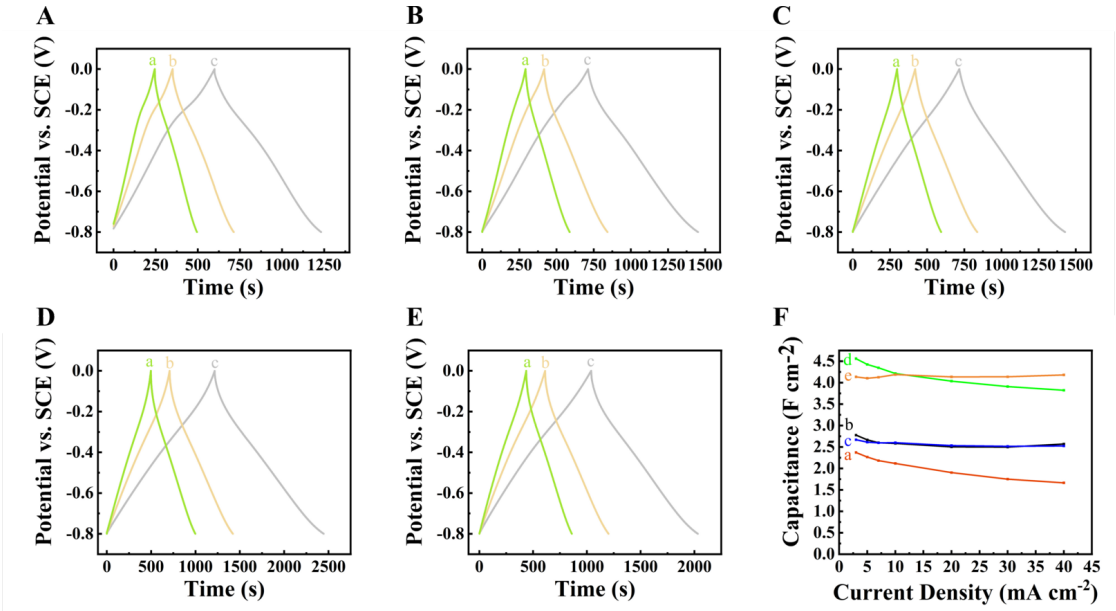

FIGURE 6.2: (A, B, C, D, E) charge-discharge curves at current densities of (a) 7, (b) 5, and (c) 3 mA cm^{-2} for (A) NA, (B) DE, (C) DW, (D) C5, and (E) C10. (F) Capacitance vs. current density profiles for (a) NA, (b) DE, (c) DW, (d) C5, and (e) C10.

The analysis of impedance data further provides evidence of the improved performance of the electrodes fabricated using murexide for surface modification of Fe_3O_4. In figure 6.3, we present the impedance at more negative potentials via Nyquist plots. We see a substantial decrease in the value of the real part of impedance for samples that were prepared with murexide, indicating that the presence of murexide results in easier charge transfer at more negative potentials. Although DE and DW samples exhibit the lowest real part of impedance at an electrode potential of 0 V vs. SCE, we see that the C5 and C10 samples exhibit much lower impedance at more negative electrode potentials (below −0.2 V vs. SCE). This decrease in impedance at lower electrode potentials is explained by the redox and electron mediation properties of murexide in this potential range.

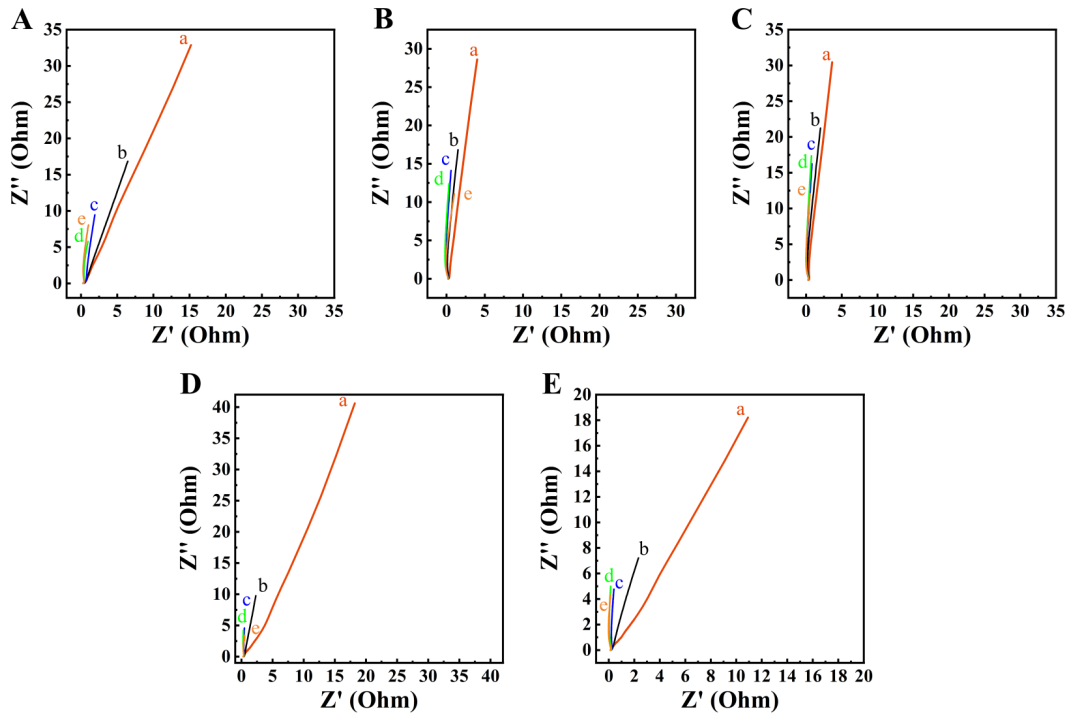

FIGURE 6.3: Nyquist plots for (A) NA, (B) DE, (C) DW, (D) C5, and (E) C10 at electrode potentials of (a) 0, (b) −0.2, (c) −0.4, (d) −0.6, and (e) −0.8 V.

Figure 6.4 shows the real part of capacitance for each of the five electrodes at 0, −0.2, −0.4, −0.6, and −0.8 V vs. SCE. We see a significant improvement in the real part of capacitance (C') for the C5 and C10 samples at electrode potentials below −0.2 V vs. SCE compared to other samples. This is consistent with what we see in the CV data, where the area of the CV curves drastically increases at lower electrode potentials when murexide is used as a capping agent. We see similar results with the dispersing agent samples (DE and DW) where the real part of capacitance is comparable to the case where no additive is used.

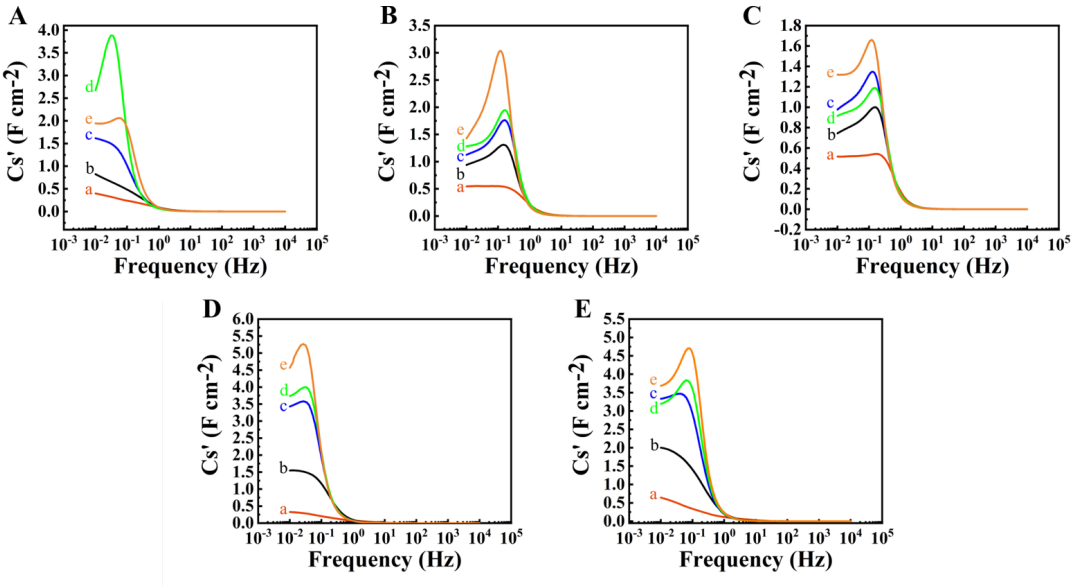

FIGURE 6.4: Real part of capacitance (C') plots for (A) NA, (B) DE, (C) DW, (D) C5, and (E) C10 at electrode potentials of (a) 0, (b) −0.2, (c) −0.4, (d) −0.6, and (e) −0.8 V vs. SCE.

From figure 6.5 an increase of relaxation frequency from the imaginary part of impedance (C'') for the electrodes prepared with murexide as a dispersing agent (DE and DW) is observed. With the analysis of impedance at more negative electrode potentials, we see an increase in both the real part of capacitance (figure 6.4) and the relaxation frequency (figure 6.5) for samples prepared with murexide, indicating the indirect contribution to the overall capacitance of the electrode via the charge mediation properties of

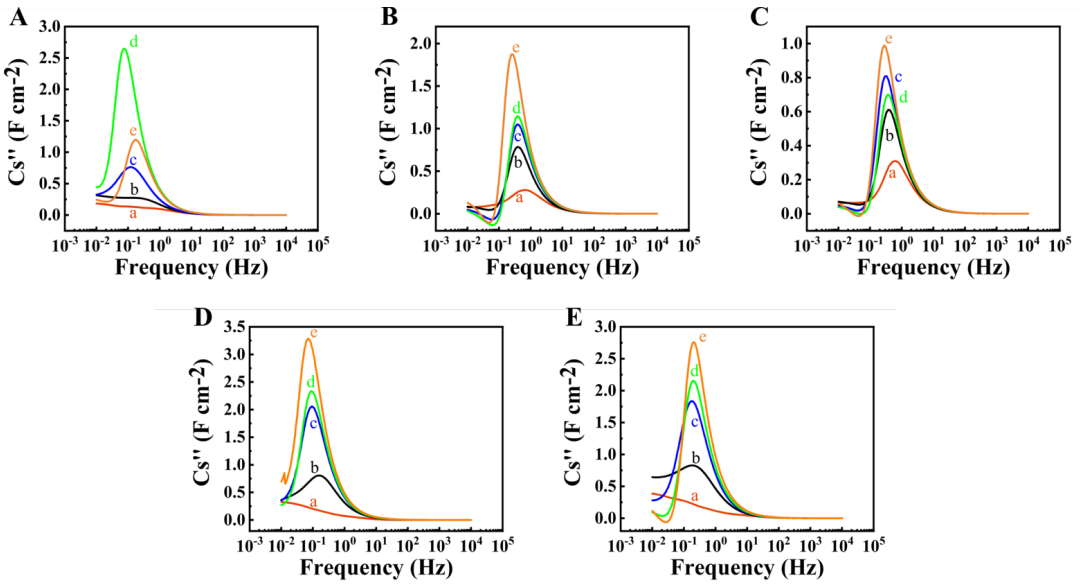

FIGURE 6.5: Imaginary part of capacitance (C'') plots for (A) NA, (B) DE, (C) DW, (D) C5, and (E) C10 at electrode potentials of (a) 0, (b) −0.2, (c) −0.4, (d) −0.6, and (e) −0.8 V vs. SCE.

murexide. Additionally, the decrease observed in the real part of impedance (figure 6.3) indicates relatively low resistance and the the large slope shown in the Z'' vs. Z' curves shows good capacitive behaviour, especially at lower electrode potentials.

6.3.2 DFT modelling of murexide adsorption on Fe_3O_4 (001) surface

DFT modelling of the adsorption process of murexide on the surface of Fe_3O_4 is conducted. The structural model (in the lowest energy configuration) is illustrated in figure 6.6. One hydrogen atom is cleaved from the murexide molecule and accommodated by Fe_3O_4 to form a surface OH group. Relaxation of bulk cubic Fe_3O_4 unit cell and subsequent construction of the (001) surface was performed following the procedure described elsewhere [36]. The selected stochiometric surface terminated with tetrahedrally coordinated Fe atoms, is in line with previous computational studies [37, 38] which have identified this (001) surface and its termination as the most energetically favourable.

Adsorption strength of murexide to the surface of Fe_3O_4 is evaluated by the calculation of an adsorption enthalpy (H_{ads}), which represents the difference between the total energy (E_{tot}) of the adsorbed and desorbed states

$$H_{\text{ads}} = H_{\text{tot}}^{\text{ads}} - H_{\text{tot}}^{\text{des}}. \tag{6.1}$$

The desorbed state is modelled as the surface slab with the murexide molecule positioned 10 Å above the surface in the vacuum layer. Our calculations yield an enthalpy of $H_{\text{ads}} = -4.5$ eV. This value indicates very strong adsorption, consistent with previous studies reporting adsorption enthalpies ranging from -1.8 eV for other organic molecules [36] to -5.5 eV for adsortion of single adatoms [39, 38] on the Fe_3O_4 (001) surface. In comparison to other organic molecules, the adsorption enthalpy of murexide onto the surface of Fe_3O_4 exhibits a remarkable increase, attributed to the formation of four bonds with the surface. This significant enhancement in adsorption energy can be attributed to the unique bonding mechanism of murexide, which involves the simultaneous formation of both bridging and chelating bonds. The adsorption of murexide results in bonding to surface Fe atoms in a manner that maintains the octahedral or tetrahedral coordination, and distorts the surface to result in coordination of surface Fe atoms closer to that of the bulk Fe atoms in the Fe_3O_4.

In addition to the calculation of adsorption energies, the adsorption mechanism is also investigated using charge density difference plots and Bader charge analysis. Figure 6.7(B) presents the three-dimensional charge density difference where the charge density of the separate surface (ρ_{surf}) and molecule, which includes the accomodated H, (ρ_{mol}) is subtracted from the charge density of the adsorbed molecule on the Fe_3O_4 surface (ρ_{ads})

$$\Delta\rho = \rho_{\text{ads}} - \rho_{\text{surf}} - \rho_{\text{mol}}. \tag{6.2}$$

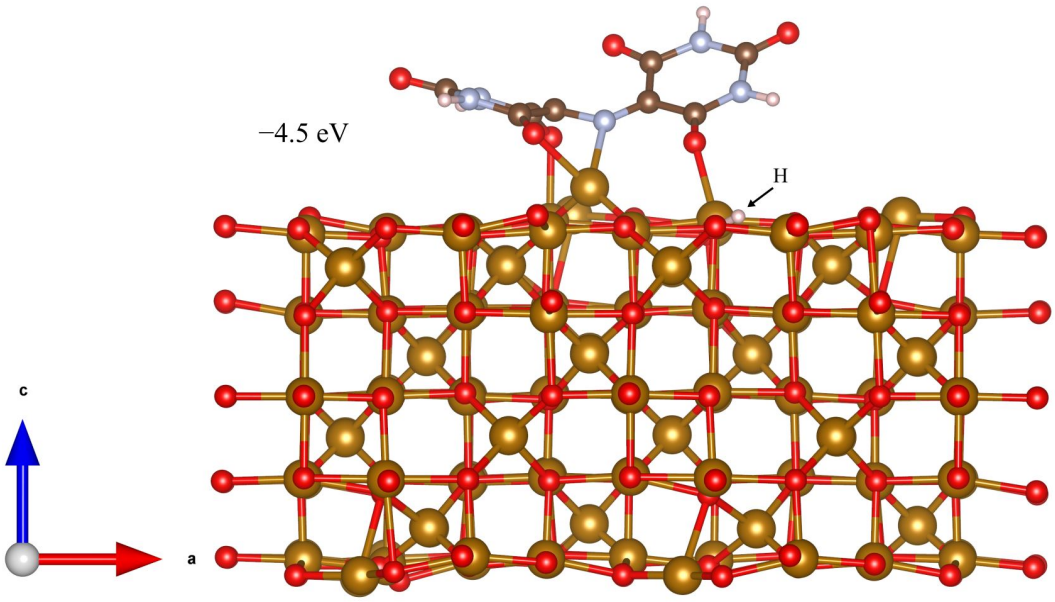

FIGURE 6.6: Adsorption of murexide on the (001) furface of Fe_3O_4. The adsorption is accompanied by the surface adsorption of an H^+ ion displaced from the OH group on the murexide molecule. The value of adsoprtion enthalpy is indicated.

Figure 6.7(A) plots the charge density planar average along the z-direction where the panel (C) plots the amount of charge transferred up to z, and is given by

$$\Delta Q(z) = \int_0^z \Delta\rho(z)\ dz. \tag{6.3}$$

From figure 6.7(A), we can see that the charge density around the Fe_3O_4 surface changes from positive to negative, indicating a transfer of negative charge from the Fe_3O_4 surface to the murexide molecule. From panel (C) we see that the largest magnitude of charge transfer occurs at $z = 13$ Å, which is in the region where the bonds are formed between murexide and the Fe_3O_4 surface during adsorption. The total net number of electrons transferred between the Fe_3O_4 surface and adsorbed murexide is 0.79 e, which implies an electron *deficiency* of in the Fe_3O_4 slab due to the adsorbed murexide molecule.

Since the charge density planar average is an average of the charge density at each point along the z-axis, we use Bader charge analysis [40, 41] to further investigate the charge transfer between Fe_3O_4 and murexide during adsorption on an atom-by-atom basis. The Bader charges can be seen in table 6.1, where we list the difference in Bader net atomic charges between the adsorbed molecule on Fe_3O_4 and the separate Fe_3O_4 surface and molecule. The bonds between murexide and Fe_3O_4 can be seen in figure 6.8 from the three-dimensional isosurface of charge density difference before and after adsorption. It is clear that electron accumulation occurs on the atoms involved in bonding that are part of the murexide molecule, where they are depleted from the surface Fe atoms, shown by the yellow and blue surfaces, respectively. This formation of a dipole results in the ionic nature of bonding of murexide onto the Fe_3O_4 surface.

By investigating the Bader charge difference between atoms in the adsorbed and desorbed states, we can gain insight into the charge transfer that occurs during the

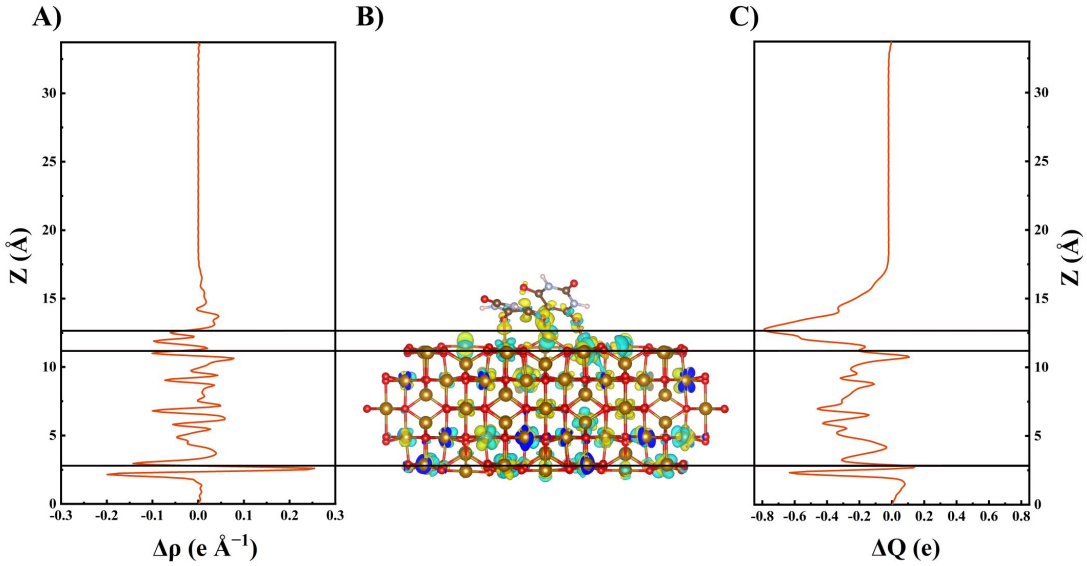

FIGURE 6.7: (A) Charge density difference planar average of murexide adsorbed on Fe_3O_4 surface, plotted along the z-axis, (B) schematic of adsorbed murexide on Fe_3O_4 with three-dimensional isosurface of the charge density difference (rendered value of ± 0.0065 e Å^{-3}), where yellow region represents area of electron accumulation and blue region represents area of electron depletion during the adsorption process, and (C) integral charge transfer $\Delta Q(z)$ with respect to position along the z-axis.

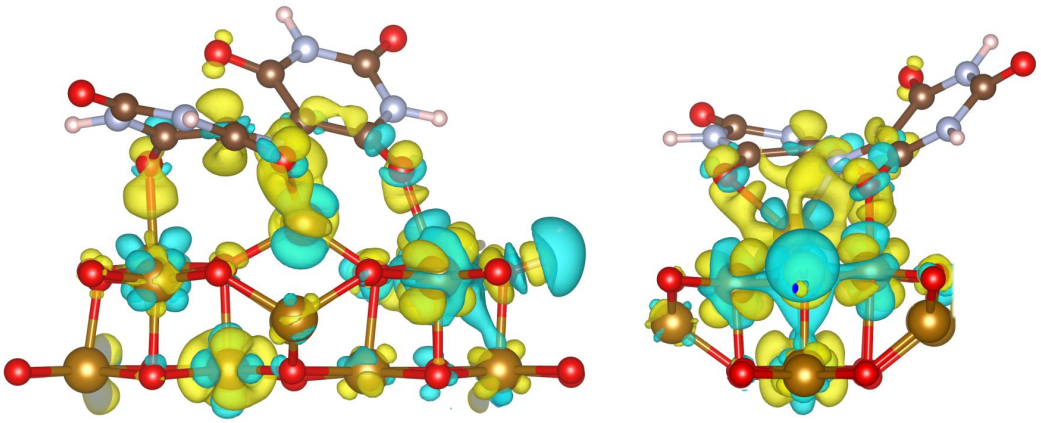

FIGURE 6.8: close-up view of three-dimensional isosurface of the charge density difference (rendered value of ± 0.0065 e Å^{-3}) for atoms involved in murexide bonding to Fe_3O_4 surface, where yellow region represents area of electron accumulation and blue region represents area of electron depletion during the adsorption process.

adsorption process, and which specific atoms play a role. From Bader charge analysis (table 6.1), during the adsortpion of murexide onto the Fe_3O_4 surface, we see a decrease in the Bader charge of 0.60 for the murexide molecule with a subsequent increase of 0.62 for the Fe_3O_4 surface. This indicates a depletion of electrons from the Fe_3O_4 surface with accumulation occuring in the murexide molecule. We can see this charge transfer takes place directly at the adsorption sites, where the bonds between the atoms in the murexide molecule form with the Fe atoms in the Fe_3O_4 surface.

From the charge density difference and Bader charge analysis, we can clearly see that the transfer of electrons from the Fe_3O_4 surface to murexide plays a critical role in the adsorption of murexide on Fe_3O_4. Additionally, this pathway for electron transfer may provide insight into the charge transfer mediation that murexide provides in Fe_3O_4 supercapacitor anodes at negative electrode potentials.

From figure 6.10, we can see that, for both spins, the lowest unoccupied molecular

TABLE 6.1: Bader charge (in units of $|e|$) of selected atoms associated with murexide adsorption (see Fig. 6.9 for labels).

Location	Separate	Bonded	Difference
Surface			
Fe_1	1.58	1.73	0.15
Fe_2	1.33	1.66	0.33
Fe_3	1.58	1.70	0.12
Sum	—	—	0.60
Murexide			
O_1	−1.00	−1.17	−0.17
O_2	−0.98	−1.10	−0.12
O_3	−1.04	−1.15	−0.11
N	−0.95	−1.17	−0.22
Sum	—	—	−0.62

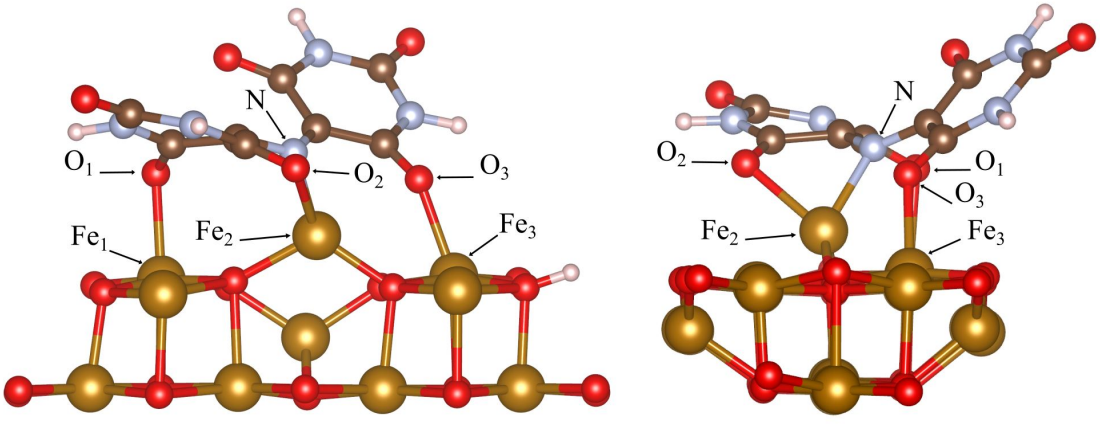

FIGURE 6.9: Close-up view of murexide adsorbed onto Fe_3O_4 surface with atoms labelled for Bader charge analysis.

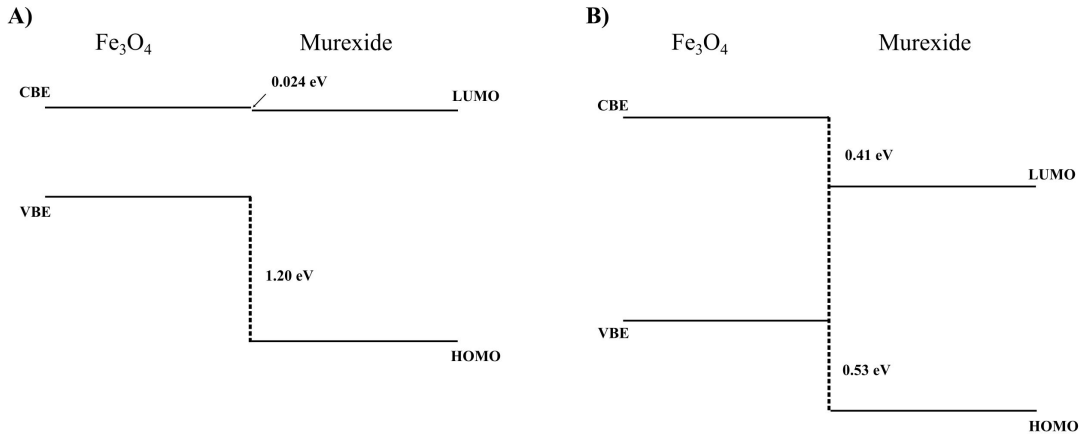

FIGURE 6.10: Schematic energy band alignment for (A) spin up and (B) spin down electronic states at the interface Fe_3O_4/murexide.

orbital (LUMO), and the highest occupied molecular orbital (HOMO) of the murexide molecule are positioned lower in energy compared to the conduction band edge (CBE) and valence abnd edge (VBE) of the Fe_3O_4, respectively. This energetic arrangement plays a pivotal role in electron transfer dynamics during the adsorption process. Specifically, the lower energy positioning of the murexide's LUMO facilitates the acceptance of electrons from the Fe_3O_4 conduction band, enabling efficient charge transfer from the metal oxide surface to the adsorbed molecule. This energetic alignment may also promotes enhanced electron transfer efficiency, with the possibility to increase the overall conductivity and performance of the system.

Further investigation of the density of states (DOS) reveals the formation of a band gap after the adsorption of murexide, while the surface is metallic (for one of the spin channels) in the non-adsorbed state (figure 6.11. This band gap formation can be seen in figure 6.11, where the density of states for the Fe_3O_4 surface before (A) and after (B) adsorption is shown. The formation of a band gap after murexide adsorption suggests a change in the electronic structure of the system. Adsorption-induced modifications, such as charge redistribution, can open up a band gap in the energy spectrum [42]. From

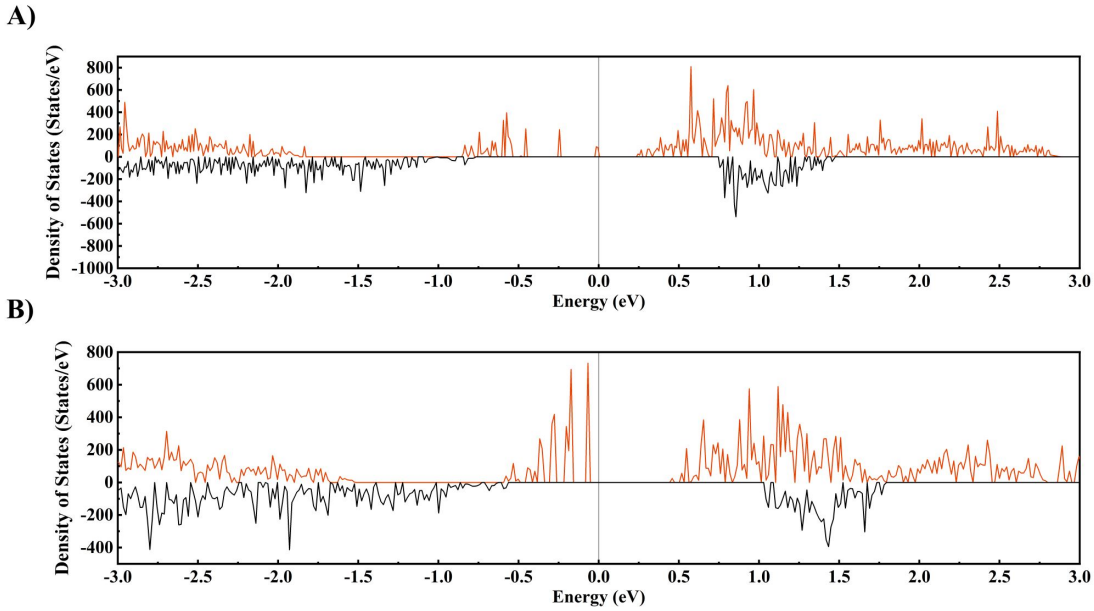

FIGURE 6.11: Density of states of the Fe_3O_4 surface before (A) and after (B) adsorption of murexide, where the red and black curves represent spin up and spin down, respectively. The Fermi energy is normalized to 0 eV.

charge-density and Bader charge analysis, the adsorption of murexide molecule on the Fe_3O_4 surface leads to a redistribution of charge. We see that the interaction between the murexide molecule and the surface atoms results in charge transfer, which can alter the occupancy of electronic states near the Fermi level.

6.4 Materials and Methods

6.4.1 Materials and Experimental Methods

Iron (II) chloride tetrahydrate, iron (III) chloride hexahydrate, ammonium hydroxide, murexide (Ammonium 2,6-dioxo-5-[(2,4,6-trioxo-5-hexahydropyrimidinylidene)amino]-3H-pyrimidin-4-olate), poly(vinyl butyral-co-vinyl alcohol-co-vinyl acetate) (PVB, MilliporeSigma, Canada), multiwalled carbon nanotubes (MWCNT, ID 4 nm, OD 13 nm, length 1−2 μm, Bayer, Germany), and nickel foam (porosity 95%, thickness 1.6 mm,

Vale, Canada), were used as starting materials.

Synthesis of Fe_3O_4 was performed by a chemical precipitation method [18, 43] using aqueous solutions of iron (II) chloride and iron (III) chloride. The molar ratio of $FeCl_2$ to $FeCl_3$ in the solutions was 1:2. For the synthesis of Fe_3O_4 in the presence of MWCNT, a 3 g L^{-1} MWCNT suspension was initially prepared. Preparation included ultrasonication of the MWCNT suspensions using a high energy Cole-Parmer (Canada) ultrasonic processor. Iron (II) chloride tetrahydrate and iron (III) chloride hexahydrate were added to the suspension, allowing for an Fe_3O_4:MWCNT mass ratio of 4:1. The pH of the solutions was adjusted to pH=9 by ammonium hydroxide. Chemical precipitation was performed at 50 °C at continuous stirring. Obtained suspensions were separated via centrifuge, washed, filtrated, and dried overnight in an oven at 60 °C. For DE and DW samples, Fe_3O_4-MWCNT suspension was redispersed in ethanol and water, respectively, via ultrasonication before being separated, washed, filtrated, and dried. For C5 and C10 samples, murexide was added to the Fe salt solution during synthesis in a weight percentage of 5% and 10%, respectively, then separated, washed, filtrated, and dried.

Electrodes were prepared by impregnation of Ni foam current collectors with slurries, containing Fe_3O_4, MWCNT and PVB binder. The mass ratio of Fe_3O_4:MWCNT:PVB was 80:20:3. The mass of the impregnated material after drying was 40 mg cm^{-2}. The impregnated Ni foams were pressed to 30% of their original thickness in order to improve electrical contact of the impregnated material and current collector.

Electrochemical studies were performed in aqueous 0.5 M Na_2SO_4 electrolyte using Biologic VMP 300 potentiostat (BioLogic, France) for CV, electrochemical impedance spectroscopy (EIS), and GCD investigations. Testing was performed using a 3-electrode electrochemical cell containing a working electrode (impregnated Ni foam), counter-electrode (Pt mesh), and a reference electrode (SCE, saturated calomel electrode). Mass and area normalized capacitances were calculated from the corresponding CV and GCD

data, as described by previous studies [44, 45]. The capacitances calculated from the CV and GCD data represented integral capacitances measured in a potential window of $-0.8 \ldots 0$ V versus SCE. The capacitances calculated from the EIS data represented differential capacitances measured at a potential 0 V, -0.2 V, -0.4 V, -0.6 V, and -0.8 V versus SCE, at voltage amplitude of 5 mV. CV results were obtained at 2, 5, 10, 20, 50, and 100 mV s^{-1} scan rates with EIS measurements performed afterwards. GCD results were obtained at 3, 5, 7, 10, 20, 30, and 40 mA cm^{-2} current densities.

6.4.2 Computational

The first-principles electronic structure calculations were performed in the framework of DFT [46] using Perdew–Burke–Ernzerhof (PBE) generalized gradient approximation [47] for the exchange correlation functional, augmented by the DFT-D3 correction with Becke–Johnson damping [48, 49] to capture van der Waals interactions. The Vienna ab initio simulation program (VASP) (version 5.4.4, University of Vienna, Vienna, Austria) [50, 51, 52] and projector augmented-wave potentials [53] were used, where the p semi-core states were treated as valence states for Fe potentials in all calculations. Standard potentials were used for all other elements. The cut-off energy for a plane wave expansion of 400 eV was used for adsorption calculations. We included on-site Coulomb interaction to treat the highly correlated Fe 3d-electrons in the framework of Dudarev et al. [54] using an effective Hubbard energy of $U = 3.7$ eV [39]. Collinear spin-polarized calculations were performed for all structures. Magnetic moments were initialized with opposing spin orientations of magnitude 4.0 μ_B for tetrahedrally and octahedrally coordinated Fe atoms [55]. Only forces were relaxed for surface models of Fe_3O_4 with an additional constraint of atomic position for the middle three layers of the Fe_3O_4 surface structure, to maintain bulk atomic positions. The structure was considered as optimized when the magnitude of Hellmann–Feynman forces acting on atoms dropped below 50 meV $Å^{-1}$ and components of the stress tensor did not exceed 1 kbar. The groundstate energy

was calculated using first order Methfessel–Paxton smearing with a width of 0.02 eV. A blocked-Davidson algorithm with high precision is used during the relaxation of the bulk and surface Fe_3O_4 structures. The Brillouin zone was sampled with a Γ-centered k-mesh generated automatically with a linear density of 30 divisions per 1 $Å^{-1}$ of the reciprocal space.

The electronic and charge properties of the murexide adsorbate and Fe_3O_4 system was investigated by analyzing the Bader charge [41] and DOS analysis. In Bader analysis, the electron charge distribution from the DFT calculation was partitioned and assigned to individual atoms. The differences in the partitioned charge before and after adsorption indicate charge transfer between the surface and adsorbate. DOS analysis examines chemical bonding interactions by showing the changes in the occupation of the electron energy levels associated with adsorption. Charge density planar average and DOS plots were obtained from data using VASPKIT [56].

All structure files and VASP input files used in this work can be found in the Supporting Information section. Structure files can be visualized in VESTA [57].

6.5 Conclusions

In conclusion, the experimental results presented in this study provide evidence for the effectiveness of murexide as a capping agent to enhance the performance of MWCNT-Fe_3O_4 supercapacitor anodes. The addition of murexide, whether as a dispersing agent or a capping agent, resulted in significant improvements in electrode performance compared to the case without any additive. When used as a dispersing agent, 5% murexide in ethanol and water led to slight increases in peak capacitance and remarkable improvements in capacitance retention at higher scan rates. On the other hand, murexide as a capping agent during synthesis resulted in a more substantial, 1.9-fold increase in peak capacitance, reaching values as high as 4.6 F cm^{-2} in the case of the C5 sample,

and maintaining the improved capacitance retention when murexide concentration is increased.

The analysis of impedance data further supported the enhanced performance of murexide-modified electrodes, showing easier charge transfer and improved capacitance at negative electrode potentials. GCD data confirmed the pseudocapacitive behavior of the electrodes and demonstrated the superior charge storage capacity of murexide-modified electrodes.

The atomistic modelling of the adsorption process of murexide on the Fe_3O_4 surface provided valuable insights into the adsorption strength, bonding characteristics, charge transfer, and electronic properties. The strong adsorption of murexide on the Fe_3O_4 surface is indicated by an adsorption enthalpy of -4.5 eV. Additionally, it is evident that the coordination of Fe atoms in bonding significantly influences the interaction between atoms. Specifically, O and N from murexide forms bonds with surface Fe atoms in a manner which restores their respective bulk tetrahedral or octahedral coordination. Further analysis using charge density difference plots, Bader charge analysis, and DOS demonstrated the transfer of electrons from the Fe_3O_4 surface to murexide and was found to play a critical role in the adsorption process. This electron transfer pathway may have implications for the charge transfer mediation provided by murexide in Fe_3O_4 supercapacitor anodes at negative electrode potentials. Additionally, the band alignment analysis reveals that the lower energy levels of the LUMO and HOMO of the murexide molecule compared to the CBE and VBE of Fe_3O_4, respectively, allows for the transfer of electrons from the Fe_3O_4 surface to murexide during adsorption, and may illustrate a conductive pathway for electrons to decrease electrode resistance.

Overall, these findings contribute to a deeper understanding of the interaction between murexide and Fe_3O_4 and have implications for the development of advanced energy storage systems. The demonstrated improvements in electrode performance and

the insights into the adsorption process and charge transfer mechanisms provide a foundation for further exploration of murexide and its potential applications in various fields, including energy storage devices.

6.6 Acknowledgement

This research was funded by the Natural Sciences and Engineering Research Council of Canada, grant number RGPIN-2018-04014, and Faculty of Engineering of McMaster University. Calculations were performed using the Compute Canada infrastructure supported by the Canada Foundation for Innovation under John R. Evans Leaders Fund.

Data availability

The raw data (VASP input and structure files) required to reproduce computational findings are available in the form Zenodo file repository [58].

Bibliography

[1] A. G. Olabi, Q. Abbas, A. Al Makky, and M. A. Abdelkareem, "Supercapacitors as next generation energy storage devices: Properties and applications," *Energy*, vol. 248, p. 123617, June 2022.

[2] P. Forouzandeh, V. Kumaravel, and S. C. Pillai, "Electrode materials for supercapacitors: A review of recent advances," *Catalysts*, vol. 10, p. 969, Aug. 2020.

[3] R. M. E. Silva, R. Poon, J. Milne, A. Syed, and I. Zhitomirsky, "New developments in liquid-liquid extraction, surface modification and agglomerate-free processing of inorganic particles," *Adv. Colloid Interface Sci.*, vol. 261, pp. 15–27, Nov. 2018.

[4] Q. Zhao, X. Wang, J. Liu, H. Wang, Y. Zhang, J. Gao, J. Liu, and Q. Lu, "Surface modification and performance enhancement of carbon derived from chromium carbide for supercapacitor applications," *J. Electrochem. Soc.*, vol. 162, no. 6, pp. A845–A851, 2015.

[5] A. Pimsawat, A. Tangtrakarn, N. Pimsawat, and S. Daengsakul, "Effect of substrate surface roughening on the capacitance and cycling stability of Ni(OH)2 nanoarray films," *Sci. Rep.*, vol. 9, p. 16877, Nov. 2019.

[6] L. W. Yang and I. Zhitomirsky, "Influence of capping agents on the synthesis of Mn_3O_4 nanostructures for supercapacitors," *ACS Appl. Nano Mater.*, vol. 6, pp. 4428–4436, Mar. 2023.

[7] W. Chen, R. B. Rakhi, L. Hu, X. Xie, Y. Cui, and H. N. Alshareef, "High-performance nanostructured supercapacitors on a sponge," *Nano Lett.*, vol. 11, pp. 5165–5172, Dec. 2011.

[8] Y. Shao, M. F. El-Kady, J. Sun, Y. Li, Q. Zhang, M. Zhu, H. Wang, B. Dunn, and R. B. Kaner, "Design and mechanisms of asymmetric supercapacitors," *Chem. Rev.*, vol. 118, pp. 9233–9280, Sept. 2018.

[9] T. Brousse and D. Bélanger, "A hybrid Fe_3O_4-MnO_2 capacitor in mild aqueous electrolyte," *Electrochem. Solid State Letters*, vol. 6, no. 11, p. A244, 2003.

[10] Y. Gogotsi and P. Simon, "Materials science. true performance metrics in electrochemical energy storage," *Science*, vol. 334, pp. 917–918, Nov. 2011.

[11] M. S. Ata, Y. Liu, and I. Zhitomirsky, "A review of new methods of surface chemical modification, dispersion and electrophoretic deposition of metal oxide particles," *RSC Adv.*, vol. 4, no. 43, p. 22716, 2014.

[12] W. Yang, M. Nawwar, and I. Zhitomirsky, "Facile route for fabrication of ferrimagnetic Mn3O4 spinel material for supercapacitors with enhanced capacitance," *Energies*, vol. 15, p. 1812, Mar. 2022.

[13] D. E. Tallman, C. Vang, G. G. Wallace, and G. P. Bierwagen, "Direct electrodeposition of polypyrrole on aluminum and aluminum alloy by electron transfer mediation," *J. Electrochem. Soc.*, vol. 149, no. 3, p. C173, 2002.

[14] C. Shi and I. Zhitomirsky, "Electrodeposition of composite polypyrrole–carbon nanotube films," *Surf. Eng.*, vol. 27, pp. 655–661, Oct. 2011.

[15] S. Chen and I. Zhitomirsky, "Influence of dopants and carbon nanotubes on polypyrrole electropolymerization and capacitive behavior," *Mater. Lett.*, vol. 98, pp. 67–70, May 2013.

[16] D. K. Ariyanayagamkumarappa and I. Zhitomirsky, "Electropolymerization of polypyrrole films on stainless steel substrates for electrodes of electrochemical supercapacitors," *Synth. Met.*, vol. 162, pp. 868–872, June 2012.

[17] S. Sakib, F. Bakhshandeh, S. Saha, L. Soleymani, and I. Zhitomirsky, "Surface functionalization of metal oxide semiconductors with catechol ligands for enhancing their photoactivity," *Sol. RRL*, vol. 5, p. 2100512, Oct. 2021.

[18] M. Nawwar, R. Poon, R. P. Sahu, I. K. Puri, and I. Zhitomirsky, "Fe3O4 spinel-Mn3O4 spinel supercapacitor prepared using celestine blue as a dispersant, capping agent and charge transfer mediator," *Ceram. Int.*, vol. 46, pp. 18851–18858, Aug. 2020.

[19] H. Yu, J. Wu, L. Fan, S. Hao, J. Lin, and M. Huang, "An efficient redox-mediated organic electrolyte for high-energy supercapacitor," *J. Power Sources*, vol. 248, pp. 1123–1126, Feb. 2014.

[20] Y. Yin, J. Zhou, A. N. Mansour, and X. Zhou, "Effect of NaI/I2 mediators on properties of PEO/LiAlO2 based all-solid-state supercapacitors," *J. Power Sources*, vol. 196, pp. 5997–6002, July 2011.

[21] B. Akinwolemiwa, C. Peng, and G. Z. Chen, "Redox electrolytes in supercapacitors," *J. Electrochem. Soc.*, vol. 162, no. 5, pp. A5054–A5059, 2015.

[22] A. G. Tamirat, X. Guan, J. Liu, J. Luo, and Y. Xia, "Redox mediators as charge agents for changing electrochemical reactions," *Chem. Soc. Rev.*, vol. 49, pp. 7454–7478, Sept. 2020.

[23] S. Roldán, C. Blanco, M. Granda, R. Menéndez, and R. Santamaría, "Towards a further generation of high-energy carbon-based capacitors by using redox-active electrolytes," *Angew. Chem. Int. Ed Engl.*, vol. 50, pp. 1699–1701, Feb. 2011.

[24] S. Kashanian, M. B. Gholivand, S. Madaeni, A. Nikrahi, and M. Shamsipur, "Spectrophotometric study of the complexation reactions between alkaline earth cations and murexide in some non-aqueous solutions," *Polyhedron*, vol. 7, pp. 1227–1230, Jan. 1988.

[25] M. Shamsipur, A. Esmaeili, and M. K. Amini, "Formation of cobalt, nickel and copper complexes with murexide in ethanol-water mixtures," *Talanta*, vol. 36, pp. 1300–1302, Dec. 1989.

[26] M. Shamsipur, S. Madaeni, and S. Kashanian, "Spectrophotometric study of the alkali metal-murexide complexes in some non-aqueous solutions," *Talanta*, vol. 36, pp. 773–776, July 1989.

[27] H. Parham and M. Shamsipur, "Spectrophotometric study of some alkali and alkaline earth cryptates in dimethylformamide solution using murexide as a metallochromic indicator," *Polyhedron*, vol. 11, pp. 987–991, Jan. 1992.

[28] M. S. Masoud, T. S. Kassem, M. A. Shaker, and A. E. Ali, "Studies on transition metal murexide complexes," *J. Therm. Anal. Calorim.*, vol. 84, pp. 549–555, May 2006.

[29] Mohran, "An electrochemical investigation of the redox properties of murexide in aqueous and non-aqueous media," *Am. J. Appl. Sci.*, vol. 6, pp. 964–969, May 2009.

[30] M. Serwar, U. A. Rana, H. M. Siddiqi, S. Ud-Din Khan, F. A. Ahmed Ali, A. Al-Fatesh, A. Adomkevicius, J. A. Coca-Clemente, L. Cabo-Fernandez, F. Braga, and L. J. Hardwick, "Template-free synthesis of nitrogen doped carbon materials from an organic ionic dye (murexide) for supercapacitor application," *RSC Adv.*, vol. 7, pp. 54626–54637, 2017.

[31] N. Z. Atay and T. Varnali, "A semi-empirical study on metal ion/murexide complexation," *Turkish Journal of Chemistry*, vol. 26, pp. 303–310, 2002.

[32] W. G. Pell and B. E. Conway, "Analysis of power limitations at porous supercapacitor electrodes under cyclic voltammetry modulation and dc charge," *J. Power Sources*, vol. 96, pp. 57–67, June 2001.

[33] A. Chowdhury, S. Biswas, T. Singh, and A. Chandra, "Redox mediator induced electrochemical reactions at the electrode-electrolyte interface: Making sodium-ion supercapacitors a competitive technology," *Electrochem. Sci. Adv.*, vol. 2, pp. 1–14, Feb. 2022.

[34] O. Gharbi, M. T. T. Tran, B. Tribollet, M. Turmine, and V. Vivier, "Revisiting cyclic voltammetry and electrochemical impedance spectroscopy analysis for capacitance measurements," *Electrochim. Acta*, vol. 343, p. 136109, May 2020.

[35] V. Augustyn, P. Simon, and B. Dunn, "Pseudocapacitive oxide materials for high-rate electrochemical energy storage," *Energy Environ. Sci.*, vol. 7, no. 5, p. 1597, 2014.

[36] C. Boucher, O. Rubel, and I. Zhitomirsky, "Supercapacitor performance of magnetite nanoparticles enhanced by a catecholate dispersant: Experiment and theory," *Molecules*, vol. 28, p. 1562, Feb. 2023.

[37] R. Bliem, E. McDermott, P. Ferstl, M. Setvin, O. Gamba, J. Pavelec, M. A. Schneider, M. Schmid, U. Diebold, P. Blaha, L. Hammer, and G. S. Parkinson, "Subsurface cation vacancy stabilization of the magnetite (001) surface," *Science*, vol. 346, pp. 1215–1218, Dec. 2014.

[38] R. Gargallo-Caballero, L. Martín-García, A. Quesada, C. Granados-Miralles, M. Foerster, L. Aballe, R. Bliem, G. S. Parkinson, P. Blaha, J. F. Marco, and J. de la Figuera, "Co on fe_3o_4(001): Towards precise control of surface properties," *J. Chem. Phys.*, vol. 144, p. 094704, Mar. 2016.

[39] R. Bliem, J. Pavelec, O. Gamba, E. McDermott, Z. Wang, S. Gerhold, M. Wagner, J. Osiecki, K. Schulte, M. Schmid, P. Blaha, U. Diebold, and G. S. Parkinson, "Adsorption and incorporation of transition metals at the magnetite fe_3o_4 (001) surface," *Phys. Rev. B Condens. Matter Mater. Phys.*, vol. 92, Aug. 2015.

[40] R. F. W. Bader, "Principle of stationary action and the definition of a proper open system," *Phys. Rev. B*, vol. 49, pp. 13348–13356, May 1994.

[41] G. Henkelman, A. Arnaldsson, and H. Jónsson, "A fast and robust algorithm for bader decomposition of charge density," *Computational Materials Science*, vol. 36, no. 3, pp. 354–360, 2006.

[42] A. M. Rojas-Cuervo and R. R. Rey-González, "Electronic band gap on graphene induced by interaction with hydrogen cyanide. an DFT analysis," *Chem. Phys.*, vol. 565, p. 111744, Jan. 2023.

[43] M. Nawwar, R. Poon, R. Chen, R. P. Sahu, I. K. Puri, and I. Zhitomirsky, "High areal capacitance of fe_3o_4-decorated carbon nanotubes for supercapacitor electrodes," *Carbon Energy*, vol. 1, pp. 124–133, Sept. 2019.

[44] K. Shi and I. Zhitomirsky, "Electrophoretic nanotechnology of graphene-carbon nanotube and graphene-polypyrrole nanofiber composites for electrochemical supercapacitors," *J. Colloid Interface Sci.*, vol. 407, pp. 474–481, Oct. 2013.

[45] Y. Zhu, K. Shi, and I. Zhitomirsky, "Polypyrrole coated carbon nanotubes for supercapacitor devices with enhanced electrochemical performance," *J. Power Sources*, vol. 268, pp. 233–239, Dec. 2014.

[46] W. Kohn and L. J. Sham, "Self-consistent equations including exchange and correlation effects," *Phys. Rev.*, vol. 140, pp. A1133–A1138, Nov. 1965.

[47] J. P. Perdew, K. Burke, and M. Ernzerhof, "Generalized gradient approximation made simple," *Phys. Rev. Lett.*, vol. 77, pp. 3865–3868, Oct. 1996.

[48] S. Grimme, S. Ehrlich, and L. Goerigk, "Effect of the damping function in dispersion corrected density functional theory," *J. Comput. Chem.*, vol. 32, pp. 1456–1465, May 2011.

[49] S. Grimme, J. Antony, S. Ehrlich, and H. Krieg, "A consistent and accurate ab initio parametrization of density functional dispersion correction (DFT-D) for the 94 elements H-Pu," *J. Chem. Phys.*, vol. 132, p. 154104, Apr. 2010.

[50] G. Kresse and J. Hafner, "Ab initio molecular dynamics for liquid metals," *Phys. Rev. B Condens. Matter*, vol. 47, pp. 558–561, Jan. 1993.

[51] G. Kresse and J. Furthmüller, "Efficiency of ab-initio total energy calculations for metals and semiconductors using a plane-wave basis set," *Comput. Mater. Sci.*, vol. 6, pp. 15–50, July 1996.

[52] G. Kresse and J. Furthmüller, "Efficient iterative schemes for ab initio total-energy calculations using a plane-wave basis set," *Phys. Rev. B Condens. Matter*, vol. 54, pp. 11169–11186, Oct. 1996.

[53] G. Kresse and D. Joubert, "From ultrasoft pseudopotentials to the projector augmented-wave method," *Phys. Rev. B Condens. Matter*, vol. 59, pp. 1758–1775, Jan. 1999.

[54] S. L. Dudarev, G. A. Botton, S. Y. Savrasov, C. J. Humphreys, and A. P. Sutton, "Electron-energy-loss spectra and the structural stability of nickel oxide: An LSDA+U study," *Phys. Rev. B Condens. Matter*, vol. 57, pp. 1505–1509, Jan. 1998.

[55] F. Chiter, V. B. Nguyen, N. Tarrat, M. Benoit, H. Tang, and C. Lacaze-Dufaure, "Effect of van der waals corrections on DFT-computed metallic surface properties," *Mater. Res. Express*, vol. 3, p. 046501, Apr. 2016.

[56] V. Wang, N. Xu, J.-C. Liu, G. Tang, and W.-T. Geng, "Vaspkit: A user-friendly interface facilitating high-throughput computing and analysis using vasp code," *Computer Physics Communications*, vol. 267, p. 108033, 2021.

[57] K. Momma and F. Izumi, "Vesta 3 for three-dimensional visualization of crystal, volumetric and morphology data," *J. Appl. Crystallogr.*, vol. 44, pp. 1272–1276, Dec. 2011.

[58] C. Boucher, I. Zhitomirsky, and O. Rubel, "Application of murexide as a capping agent for fabrication of magnetite anodes for supercapacitors: experimental and first-principle studies (computational workflows)," 2023. doi:10.5281/zenodo.8183854.

Chapter 7

Conclusions and Future Work

Investigations have successfully explored the use of 3,4-dihydroxybenzoic acid and murexide as effective dispersing and capping agents in the synthesis of CNT-Fe_3O_4 composite electrodes for supercapacitor applications. The incorporation of these agents has proven to be instrumental in controlling nanoparticle size, reducing agglomeration of particles, and improving the overall performance of the composite electrodes. Notably, these studies incorporated the use of DFT calculations, which provided an in-depth and novel understanding of the adsorption phenomena occurring during the electrode fabrication process. These calculations have played a pivotal role in unraveling the molecular-level interactions and shedding light on the mechanisms through which these molecules enhance the anode performance.

Both experimental investigations and computational simulations have played a crucial role in gaining a comprehensive understanding of the structural, electronic, and surface properties of Fe_3O_4, as well as the interactions with additives and dispersing agents.

The successful utilization of 3,4-dihydroxybenzoic acid and murexide as dispersing

and capping agents highlights their potential as effective strategies for enhancing the performance of supercapacitor electrodes based on CNT-Fe_3O_4 composites. The improved control over particle size and reduction in agglomeration have been demonstrated to positively impact the capacitive behavior, leading to enhanced energy storage capabilities.

The use of DFT calculations has offered valuable insights into the adsorption behavior of 3,4-dihydroxybenzoic acid and murexide on the Fe_3O_4 surface, enabling a deeper understanding of their roles as dispersing and capping agents. By studying the structural, electronic, and surface properties of the materials, as well as the energetics of the adsorption process, DFT simulations have provided crucial information on the stability and binding strength of these molecules, elucidating their impact on nanoparticle size control, reduction of agglomeration, and ultimately, the improved performance of the supercapacitor anode.

The understanding gained from this research can serve as a foundation for the development of novel materials and design approaches that address the limitations of Fe_3O_4-based electrodes. Exploring different surface modification techniques, investigating the effect of nanostructuring, utilizing different dispersing molecules, or incorporating other conductive materials may offer opportunities for further enhancement of the conductive and capacitive performance of Fe_3O_4 nanoparticles to be fabricated and tested in fully functional supercapacitor devices.

Looking ahead, the use of DFT calculations can continue to play a pivotal role in future research endeavors. The computational approach offers a platform for exploring a broader range of dispersing and capping agents. The computational model developed during these investigations can continue to be expanded upon, and be used for different dispersing molecules and different material surfaces to continue to gain insights into the phenomena governing adsorption and dispersion of inorganic nanoparticles.